Charge Transport and Recombination in Dye-Sensitized Nanocrystalline Solar Cells

Lobato, K

Award date:
2007

Awarding institution:
University of Bath

Charge Transport and Recombination in Dye-Sensitized Nanocrystalline Solar Cells

Killian Paulo Kiernan Lobato
A thesis submitted for the degree of Doctor of Philosophy
University of Bath
Department of Chemistry
October 2007

Acknowledgements

My greatest thank-you goes to my supervisor, Professor Laurie Peter, for giving me the opportunity, trust and freedom that allowed me to explore.

I also wish to thank Dr. Alison Walker for co-supervising me and without whom I would never have met Professor Laurie Peter.

I must also thank Dr. Frank Marken for suggestions and for his support as my internal examiner.

Mention must also go to Dr. Brian O'Regan for accepting the role as my external examiner and whose suggestions and questioning without a doubt added to this piece of work.

Nonetheless, my work and time in Bath would have been far poorer without the academic and moral support from all the following:

Diego Martinez, with whom I shared seven years of friendship and study in Bath;

Dr. Mike Bailes, with his invaluable up-keep and design of experiments;

Dr. Petra Cameron and Dr. Upul Wijayantha for showing and handing me the ropes within the lab;

Hilary Vidnes who somehow maintains order in all our confusing proceedings. Many thanks for everything.

Oanh Nguyen, James Jennings, Halina Dunn, Alberto Fattori, Claire Walker, Claire Thomson, and Jonathan Scragg, for posing difficult yet enthusiastic questions that continually challenged me and for also taking the time to proof read the final text. I wish you all the best on your PhD's and hope to meet you sometime in the future;

Dr. Philip Dale and Dr. Benjamin Driscol O'Driscol for their continued motivation, friendship and showing me that there is and end;

Hugh Perrot, for his enthusiastic support whilst using the SEM, AFM and thermal evaporators;

Dr. Spartaco Landi, for his generous time and enthusiasm in the clean room using the SEM, Dektak and e-beam evaporator;

Domenico Regonini, for his enthusiasm in sharing his work and trying new areas with dye-sensitized cells, good luck with your PhD;

Professor Anders Hagfeldt, Dr. Gerrit Boschloo and Tomas Edvinsson, at Uppsala University for all their support during my short visit;

A special *obrigado* goes to the "Laboratório de Aplicações Fotovoltaicas e Semicondutores" group at the University of Lisbon, Professor António Vallêra, Professor Jorge Alves, Professor João Serra and Dr. Miguel Brito, who took me in and encouraged me in the final stages of writing.

My kindest regards must also go to my sister Ashling, and my special friends Margarida, Carla, Ana, Amílcar, Ramon, Maria, Marta, Tina, Rocco, Domenico, Mathew, Sara, Filipa, Alia, Filipe and Diogo for always adding to my days.

A *muchas gracias* goes to Lorena, for being there to celebrate and share the high times and pick me up from the low times.

Not forgotten is Dr. Fred Ravenhall. A big thank you for cultivating and challenging my curiosity since my school days. Rest in peace.

A final thank you goes to my parents, Noëlle and Júlio, for their continued and unparalleled support and generosity.

Contributing Work and Publications

The dye-sensitized cell employing the TiO_2 colloid prepared via the "acetic acid route" was graciously donated by Dr. Petra Cameron. This cell was used for the work described in section 8.

The work forming part of this thesis produced four papers for peer reviewed journals:

The paper "Determination of the density and energetic distribution of electron traps in dye-sensitized nanocrystalline solar cells" [1] involved using the charge extraction technique that was continuously applied throughout this work;

The paper "Direct measurement of the internal electron quasi-Fermi level in dye-sensitized solar cells using a titanium secondary electrode" [2] formed the basis of the work in section 7.5;

The paper "Direct measurement of the temperature coefficient of the electron quasi-Fermi level in dye-sensitized nanocrystalline solar cells using a titanium sensor electrode" [3] formed the basis of work in section 7.8;

The paper "Analysis of photovoltage decay transients in dye-sensitized solar cells" [4] resulted in the work in section 8.1. The full numerical computational solutions of *continuum model*, and the derivation of the approximate analytical quasi-static solutions with the resultant theoretical plots were developed by Dr. Alison Walker. The analytical solutions were then applied in the analysis of the data in section 8.2.

Symbols

A	pre-exponential factor
c	concentration
C	capacitance
D	diffusion coefficient
d	thickness
D_0	conduction band electron diffusion coefficient
D_n	apparent diffusion coefficient
ε	electrical permittivity, molar absorptivity
E_A	activation energy
E_C	conduction band
E_E	electrolyte side illumination
E_F	Fermi level
$E_{F,CE}$	Fermi level at counter electrode
$E_{F,WE}$	Fermi level at working electrode
E_{FB}	flat band potential
E_t	trap energy
E_V	valence band
f	frequency
ϕ	electrical potential
FD	Fermi-Dirac function
ff	fill-factor
f_t	trap occupancy fraction
G	generation rate
γ	non-ideality factor
$g(E_F)$	density of states
h	Plank's constant
η	efficiency
i	species i
i_L	generated photocurrent
I_P	incident photon flux
IPCE	incident photon to current conversion efficiency
i_S	reverse saturation current
I_{sun}	solar photon flux
I_T	transmitted photon flux
J	charge flux
j_{SC}	short-circuit current density
k	rate constant
k_B	Boltzmann's constant
k_d	detrapping rate
k_{ext}	extraction rate
k_t	trapping rate
λ	wavelength
L_n	diffusion length
μ	mobility
m_n	electron apparent mass
MP	maximum power point
n	electron density
n_C	conduction band electron density
N_C	conduction band density of states

N_D	donor density
n_e	total electron density
n_{eq}	dark equilibrium conduction band electron density
n_i	conduction band electron density
N_t	total trap density
n_t	trapped electron density
OC	open-circuit
P	power
q	elementary charge
Q	charge
r	radius
R	particle radius, recombination rate
R_{AMP}	input resistance/impedance or amplifier
r_c	capture rate constant
R_P	parallel resistance
r_r	release rate constant
$S/S^0/S^+/S^*$	sensitizer states
SC	short-circuit
SCE	silver chloride electrode
SE	substrate side illumination
S_n	trap capture cross-section
T	absolute temperature
τ_n	apparent electron lifetime
t_0	conduction band electron lifetime
T_C	characteristic temperature
U	potential
u	injection rate
u_i	electrochemical potential for species i
u_i^0	dark equilibrium electrochemical potential
$U_{ph,qs}$	photovoltage calculated via quasi-static approximation
U_{photo}	photovoltage
$U_{photo,num}$	photovoltage calculated numerically
V	voltage
V_{OC}	open-circuit voltage
w	space charge width, depletion region
ω	radial frequency
z_i	species i of charge magnitude z (+/- 1,2...)

Abstract

Models for electron transport and back reaction in dye-sensitized nanocrystalline solar cells were investigated by developing novel measurement techniques and the results were used to test two complementary models; diffusive electron transport within the TiO_2 medium and the quasi-static approximation to deal with non steady-state conditions where trapping plays a role. These will be shown to be partly correct and the shortfalls highlighted and discussed. In the end it was found that more knowledge of the parameters governing the behaviour of electrons is required to further test and develop the models.

The incorporation of a secondary sensing electrode allowed the internal quasi-Fermi level (QFL) within the TiO_2 to be probed. The behaviour of the voltage measured by the secondary sensing electrode was in accordance with diffusive electron transport in the TiO_2. This was confirmed by measuring the QFL along the current-voltage curve of the cell, and by the temperature dependence of the measured QFL. Discrepancies concerning the behaviour of the ideality of the open-circuit voltage (and hence the electron lifetime) between experiment and modelling are highlighted and discussed throughout.

Assuming an Arrhenius relationship simple expressions for the temperature dependence of the open-circuit voltage were derived and experimentally tested.

The trapped electron density was measured along the current-voltage curve. With the inclusion of the secondary sensing electrode and measuring the trap distribution, the way the trapped charge varied could be modelled and compared to experiment. This provided an important link between the free and trapped electron density profiles but again highlighted shortcomings of the applied models.

The quasi-static approximation was tested against a full numerical solution (continuum model) to determine the phase space in which it is applicable. Knowing this, an almost ideally behaving cell was used to test the quasi-static approximation. Having shown that it was valid for the given cell, the quasi-static approximation was used to determine how the conduction band electron lifetime varied with temperature, resulting in an Arrhenius dependence of the back reaction rate of electrons. A strong temperature dependence of the electron lifetime, and hence a strong temperature dependence of the electron diffusion length was demonstrated.

1 Introduction

The need for alternative energy sources is ever more pressing. Fossil fuel reserves are becoming scarce, making their exploration ever more expensive. Charles Fritts, a solar cell pioneer in the late 19th century, was already well aware of the problems future generations would face with energy supply; *"the supply of energy is both without limit and without cost, and will continue to stream down on earth after we have exhausted our supplies of fossil fuels"*. There are also the sensitive geopolitical issues in many parts of the world with the largest fossil fuel reserves. More important though are the reports from entities such as the Intergovernmental Panel on Climate Change (IPCC), correlating with ever greater accuracy the relationship between the marked increase in green-house gases and the accelerated changes observed in climate, e.g. global warming. Another issue is the energetic monopoly exerted by the western world, polarising the energy consumption and wealth between developed and developing nations.

Developing systems that can use free, abundant and renewable sources of energy can solve the problem of the monopolisation of energy and the environmental problems caused by burning of fossil fuels. The alternatives are as diverse as geothermal, tidal, water cycle, atmospheric movements and solar radiation. All these are consequence of the earths inherent heat, gravitational perturbations by the moon and sun, and solar radiation.

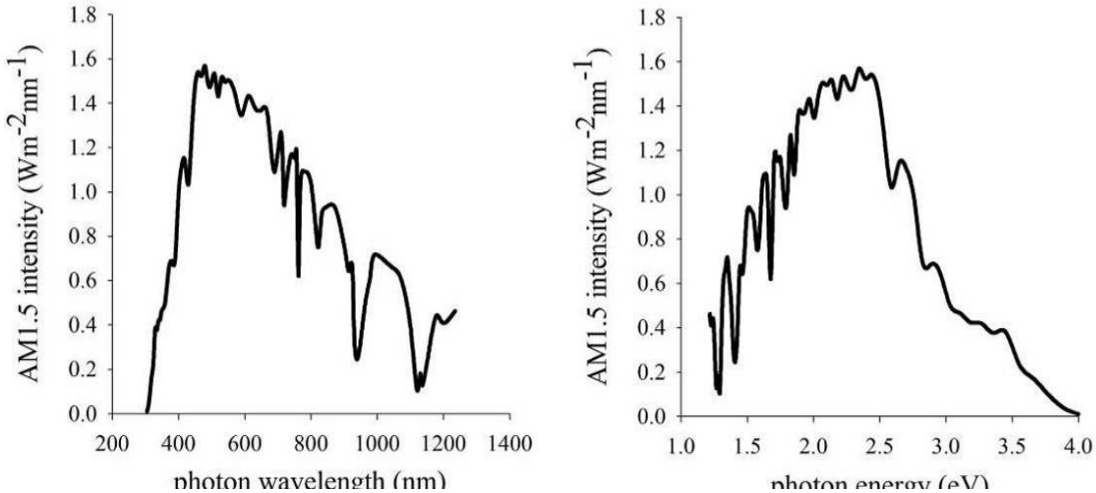

Figure 1 The AM1.5 solar spectral irradiance distribution (diffuse and direct) incident at sea level on a sun-facing 37-degree tilted surface. The atmospheric conditions for AM1.5 are: perceptible water vapour, 14.2 mm and total ozone, 3.4 mm. The aim is to harness the greatest portion of the intensity (area under the curves).

The most abundant and equally distributed of these sources is probably solar radiation. In one hour the Sun delivers the same amount of energy consumed by the whole of humanity in one year. The photovoltaic (PV) effect whereby electricity can be generated via absorption of light is an attractive means of directly generating electrical power.

The spectrum shown in Figure 1 is a typical reference spectrum describing solar radiation, and it is the energy in this spectrum which photovoltaic devices absorb and convert to electricity. The aim is to maximise the energy absorbed whilst maintaining costs low.

1.1 First Generation Solar Cells

The most popular approach is based on silicon pn semiconductor junction cells first demonstrated at Bells Labs in 1954 by Chaplin, Fuller and Pearson [5]. In the past 30 years, the cost of these has dropped by a factor of 20 with efficiencies reaching c.a. 18% for commercially available modules. For this type of device the theoretical limit (Shockley-Queisser limit) is 31% [6]. Overall, this means that although the silicon-based cells have not reached their limit, there is only a 50% gain to be obtained. Thus, the main area of interest with silicon based PV modules lies in making them more economically viable by cheaper manufacturing and increasing their working lifetime. Currently the production of electricity via PV is still an order of magnitude more expensive than by e.g. gas, 0.30$ per kWh versus 0.03$ per kWh respectively [7].

Silicon based solar cells are the holders of the market, breaking down into three categories; single crystal, polycrystalline and amorphous. Due to the high-energy requirements involved in purifying silicon, the cost can be prohibitive due to the long payback time (c.a. 10 to 20 years). There are, however, niches for each type of structure. For example, the space industry employs high-grade single crystal cells whilst low-power cheap consumer electronic devices employ amorphous silicon. Polycrystalline silicon although less efficient, is also used due to reduced manufacturing costs. These cells though are fraught with lower efficiencies due to the recombination properties of the grain boundaries. The determining factors for cost are not only crystal growth. These cells need to be packaged and positioned, both of which have costs associated with them.

Group III/IV direct bandgap semiconductor materials are also utilized in cases where efficiency is a prime objective over cost, such as the space industry.

Whereas a 100μm thickness is required for 90% absorption in silicon, only 1μm of GaAs is required for the same absorption. The main reason for this is that GaAs is a direct bandgap semiconductor and thus excitation of an electron does not require the aid of a phonon for momentum transfer.

There are also efforts into making ribbon silicon [8]. Again, the aim is the reduction of manufacturing costs, this time by circumventing the sawing of crystal ingots (c.a. 40% waste). Investigation has gone into over a score of different approaches in manufacturing ribbon silicon with some already in the pilot scheme state [9]. Impressively, these types of cells demonstrate up to 15% efficiencies and with silicon production yields up to 90%.

1.2 Second Generation Solar Cells

Second generation solar cells [10] appeared in the 1970's. There are mainly two variants; copper indium diselenide [11] and cadmium telluride [12] both coupled with n-type cadmium selenide (CdS) to create pn-heterojunction. Due to the large bandgap of CdS (2.4eV), it is utilised as a window to the pn-junctions. As direct bandgap semiconductors only a thin film (c.a. 10μm) is required for complete light absorption, unlike to first generation silicon cells (c.a.100μm).

Even though laboratory results for $CuInSe_2$ cells have been promising, there is still the need for a complete understanding of these ternary compound semiconductors. In addition, because they are ternary the manufacturing techniques required are complex especially on the up scaling. In addition, there is debate as to the validity of using rare elements such as indium.

On the other hand, CdTe has an excellent solar matching absorption spectrum with a bandgap of 1.5eV and is relatively easy to handle as a thin film. This implies that photons of energy above 1.5eV will be absorbed and converted to electrons, and at 1.5eV, this is a large proportion of the solar spectrum (see Figure 1). However, due to large differences in work functions with the metals used for contacting, there are problems in creating low resistance ohmic contacts. In addition, the toxicity of the materials has been an environmental concern.

1.3 Third Generation Solar Cells

The term describing third generation solar cells is mostly used to describe systems which do not fall into the first or second generations and/or that try

to circumvent the 31% Shockley-Queisser limit. This can be achieved by e.g. concentrating the light source [13], use of tandem cells with multiple bandgaps [14] or conversion of photons [15], where more than one electron-hole pair is generated per photon. These systems are costly and complex to prepare. However, there are also the third generation cheaper alternatives. These can be split into two categories, the organic heterojunctions [16] and dye-sensitized solar cells [17].

In organic heterojunction solar cells, the photogenerated electron-hole pairs are tightly bound, forming excitons. The charge separation occurs at the electron donor and acceptor organic polymers or at selective contacts. There are two different structures, the bilayer heterojunction and the bulk heterojunctions. The bilayer is analogous to the pn-heterojunction, while the bulk heterojunction is an attempt to maximise the p-n interface by intertwining the n-type and p-type polymers. Although efficiencies are at best 5%, this type of system is still in its infancy but with vast potential due to the almost limitless organic compounds that can be synthesized.

The dye-sensitized solar cell (DSC) also commonly known as the Grätzel cell [17] is another alternative which has attracted much attention. At the time of writing, citations to this reference [17] were approaching the 3000 mark. This large volume of published work is a consequence not only of the need for alternative forms of energy but the also the large variety of physical and chemical processes that govern a DSC. It is somewhat intriguing that a DSC being relatively simple and cheap to manufacture, (e.g. no need for clean room facilities compared to more classical photovoltaic system) is still today without a coherent model describing its photovoltaic properties. The current record efficiency for the DSC in optimised laboratory conditions stands at 11.1% [18].

2 Free Energy and Driving Forces for Charge Separation and Transport in Photovoltaic Cells

There is a general misunderstanding in elementary texts describing photovoltaic cells, incorrectly attributing the driving force for the separation of electron-hole pairs to the electrostatic potential difference across the pn-junction. The free energy of the electrons and holes is not only dependent on their potential energy (position of the conduction band edge), but also on their concentration, via the entropic term in the Gibbs energy. It is in fact the gradient of the free energy (or electrochemical potential) and not the gradient of the potential energy that is the driving force for movement of charge carriers. Würfel [19] elegantly expands on this point which is summarised below.

An example of a solid-state junction is used to explore the idea of the importance of the free energy, the p-i-n junction shown in Figure 2.

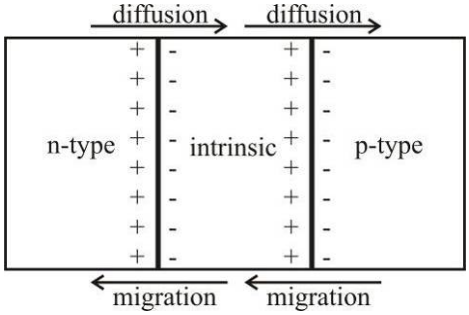

Figure 2 p-i-n junction system, showing where migration occurs due to electric fields and diffusion occurs due to concentration gradients, when three differently doped semiconductors are brought into contact.

By definition, the n-type semiconductor has a higher free electron density to the i-type and consequently the p-type semiconductor. When the three are in contact, the electron densities equilibrate. However, this gives rise to a local charge imbalance. For example, in n-doped silicon the free electron density is increased by doping the semiconductor with a group V element acting as an electron donor. The extra electron of this element is easily thermalised leaving it ionised. Charge neutrality, though, is maintained. However, when this electron is removed an immobile positive charge is left behind. In the case of p-type doping, a group III element is introduced, an acceptor which binds electrons from the conduction band to the valence band, resulting in a negatively charged ion. When the two types are contacted, the excess electron density in the n-type region diffuses to the p-type region until the free electron density throughout is equalised. However, immobile ionised donors (n-type)

and acceptors (p-type) give rise to a localised electric field at the interfaces.

In solid-state physics, the electrochemical potential is identified with the Fermi energy. The electrochemical potential for charge carriers is defined as;

$$\bar{u}_i = u_0^i + k_B T \ln \frac{n_i}{n_0} + z_i q \varphi \qquad 1$$

The electrochemical potential is sum of an equilibrium potential (u_0) related to the equilibrium density (n_0), the ratio of the excess conduction band carrier density (n_i) with the equilibrium density, and the electrostatic potential ($q\varphi$).

The flux of a charged species is related to the gradient of the free energy;

$$J_i = -\frac{z_i n_i \mu_i}{q} \frac{\partial \bar{u}_i}{\partial x} \qquad 2$$

The gradient of the electrochemical potential can be found by the differentiating the expression in equation 1;

$$\frac{\partial \bar{u}_i}{\partial x} = \frac{k_B T}{n_i} \frac{\partial n_i}{\partial x} + z_i q \frac{\partial \varphi_i}{\partial x} \qquad 3$$

Thus the flux of the given species is;

$$J_i = -\mu_i \left(\frac{k_B T}{q} \frac{\partial n_i}{\partial x} + n_i z_i q \frac{\partial \varphi_i}{\partial x} \right) \qquad 4$$

Using the Einstein relation;

$$D = \mu \frac{k_B T}{q} \qquad 5$$

Then;

$$J_i = -D_i \frac{\partial n_i}{\partial x} - u_i n_i z_i q \frac{\partial \varphi_i}{\partial x} \qquad 6$$

Equation 6 describes the two contributions to the flux of charge: diffusion and migration. However, as the gradient of the electrochemical potential corresponds to the gradient of the Fermi level used in semiconductor physics, the expression in equation 2 will be used here to describe flux.

In conventional silicon solar cells, only small gradients in the free energy are required to drive the observed short-circuit current densities. This is because of the relatively high mobilities of electrons and holes (c.a. 100 to 1000 cm^2V^-

$^{1}s^{-1}$). However, for DSCs the mobilities are significantly lower and thus to sustain large current densities the gradient in electrochemical potential has to be significantly larger. This large electrochemical gradient is explored in the work presented here.

The *quasi-Fermi* level is used to describe electrons and holes that are in thermal equilibrium with the lattice but not with each other. This occurs under illumination, to give rise to a photostationary state, one illustrated below.

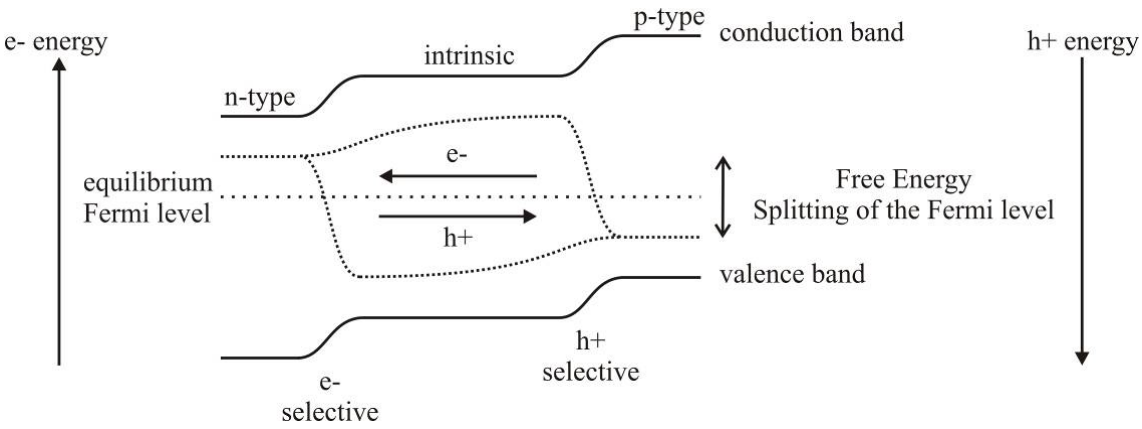

Figure 3 p-i-n homo junction system to exemplify diffusive charge transport and the role of selectivity of the n and p contact. The gradients of the electrochemical energy are exaggerated in the intrinsic region to highlight the driving forces for charge transport. By convention, a higher position in the figure signifies a higher energy for electrons, and vice versa for holes. In this case, electron-hole pairs are created in the intrinsic region. The difference of the free energies in the n and p regions is what is measured externally as a photovoltage. The selective contacts due to the in-built field only allow electrons to flow to the left and holes to the right.

The importance of selective contacts has not been addressed. In fact, the selective contacts give rise to the concentration gradients required to sustain charge flux. The example shown in Figure 3 demonstrates band bending that occurs in a p-i-n junction system. The selectivity occurs at these junctions because of the electric fields, forcing electrons and holes to flow one way or another. For example, at the n-i interface shown in Figure 3, electrons will preferentially flow to the left from the intrinsic region because the conduction band energy is lower (band is bent). The holes, however, do not, because the n-doped region is of higher energy (i.e. the positive donor ions are encountered and repel the holes, see Figure 2). Eventually, there is a build up of holes at the n-i interface and of electrons at the i-p interface, i.e. their densities are higher than at equilibrium increasing the electrochemical potential (see equation 1) and subsequently diffuse to their respective selective contacts. Under stationary conditions, a generated electron-hole pair within the intrinsic

region will separate not because of an electric field but because of the diffusive pressure (entropic). Electrons move towards the n-i interface and holes towards the i-p interface.

The selectivity of the contacts need not be caused by an electric field, but can as in a DSC, be kinetically driven. In addition, in the case of DSCs, there is, in principle, no significant field in the bulk of the nanocrystalline semiconductor.

3 Introducing the Dye-Sensitized Nanocrystalline Solar Cell

The DSC is made up of various components, the absorber being a monolayer of dye molecules sensitizing the supporting semiconductor oxide layer, the redox electrolyte and the transparent contacting electrodes. These are all contacted via an redox electrolyte.

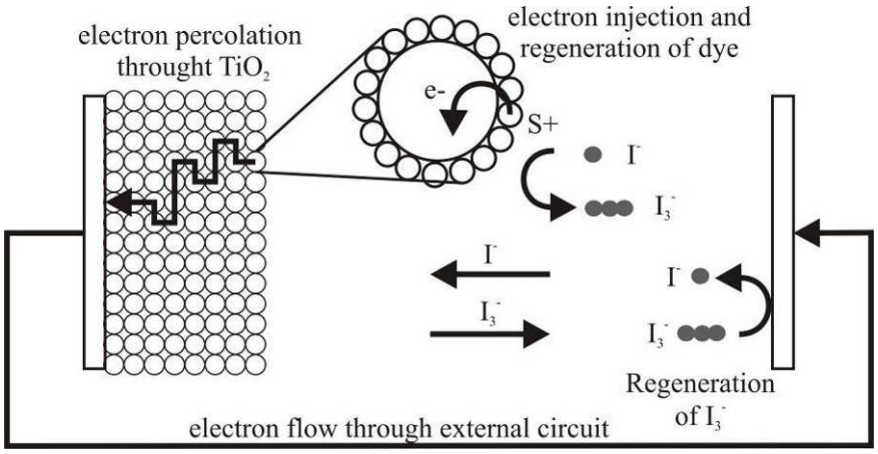

Figure 4 Schematic representation of a DSC

Photons are absorbed by the absorber layer by excitation of electrons from a HOMO to a LUMO level. These excited electrons are then injected into the supporting oxide layer, giving rise to charge separation, resulting in free electrons in the conduction band of the oxide and empty states in the dye molecules. These empty states are regenerated by electron transfer from the redox electrolyte. The free electrons percolate through the porous oxide and move to the external circuit via the transparent electrode. After passing through the external circuit, electrons return to the system to regenerate the electrolyte components that were used to regenerate the dye molecules, hence completing the circuit.

This brief outline of the components and how electrons travel through a DSC, highlights the different disciplines required to understand the properties of a DSC. The dye molecules tend to be organometallic compounds, though purely organic dyes are coming into the frame. The electrolyte components can range from simple ionic species in a solvent to conducting polymers. Various oxides can be used, and their preparation can vary greatly from hydrolysis of metal-containing compounds to anodic oxidation of metal sheets to create porous films. Also important to the overall performance of a DSC, is the quality of supporting substrate, which has to be transparent but with good conductivity.

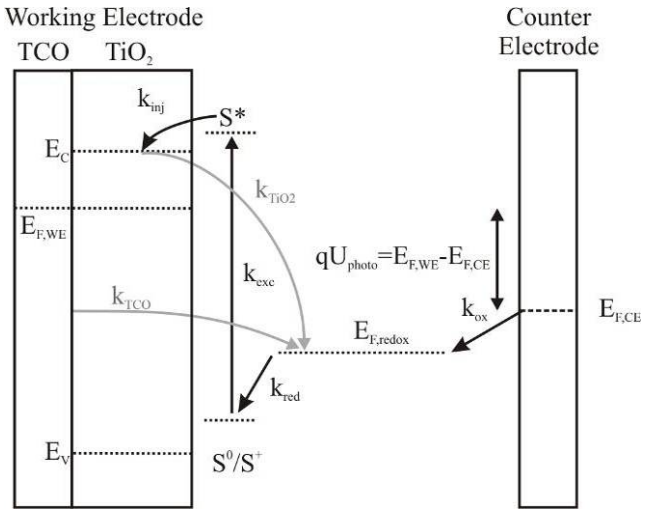

Figure 5 Schematic rendition of the DSC illustrating the competing mechanisms. k_{inj} - injection rate constant from dye to the oxide, k_{exc} - excitation rate constant from the HOMO to the LUMO, k_{TiO2} - recombination rate constant from the oxide to the electrolyte, k_{TCO} - recombination rate constant of electrons from the TCO to the electrolyte, k_{red} - reduction rate constant of dye molecules by the electrolyte and k_{ox} - oxidation rate constant of the counter electrode with the electrolyte. Shown, too, are the relative positions of the energy levels of the conduction band E_C, valence band E_V, LUMO and HOMO levels, the electrolyte redox potential $E_{F,redox}$, along with the splitting of the quasi-Fermi level E_F, at the working and counter electrodes.

It is the asymmetry of the kinetics of the reactions and electron transfer, that generates a build-up of electrons in the oxide, that can drive the electrons around an external circuit and allow for splitting of the Fermi levels. The electron upon excitation has to be rapidly injected into the oxide before it can fall back to its ground state. The regeneration of the dye by the redox electrolyte has to be faster than the possible recombination with electrons in the oxide. The transit time of electrons inside the oxide film has to be lower than the typical time required for them to recombine either with, an oxidised dye molecule, (not shown in Figure 5, but shown in Figure 8) or electron accepting electrolyte species. Also, the exposed areas of the TCO to the electrolyte can be regions of back reaction, so the recombination rate of electrons via the TCO to the electrolyte has to be low as well. The regeneration of the redox electrolyte at the counter electrode has to be facile so that the energy loss in this step is minimised.

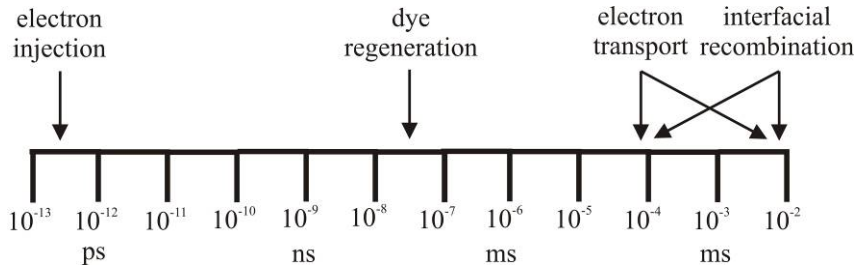

Figure 6 Schematic diagram highlighting the difference in kinetics involved in a DSC [20].

The challenge in understanding a DSC lies in the number of compromises or inefficiencies of components making up a complete cell. For example, ideally only a monolayer of oxide could be used to support a dye with an infinite extinction coefficient. Obviously, such dyes do not exist, so the surface area has to be increased. This is achieved by preparing a porous network augmenting the cross-section area by a factor of c.a. 1000. The cross-section could also be further enhanced by use of a thicker porous structure so that all the incoming photons are absorbed. The problem arising from this is that electrons have a limited diffusion length. The best compromise is reached where the thickness of the porous structure is such that all photogenerated electrons will be collected. In addition, the porosity of the network could influence the pathway of the electrons for collection.

The development of DSCs has been pursued on mainly empirical lines. It is only recently that a clearer understanding has emerged of the factors controlling their efficiency.

3.1 Dyes: Injecting Electrons into the Titanium Dioxide

The optimal sensitizer should absorb light above a certain threshold. Only photons of energy greater than the HUMO-LUMO gap are absorbed, and any energy they may have greater than the bandgap is lost as heat. Thus, there is a trade-off between the number of photons absorbed (small gap) and the energy associated with their absorption (large gap). It is found that an optimal gap for solar illumination is 1.4eV (i.e. absorbing photons of 900nm of greater). This is the optimal value considering the radiation spectrum of the Sun (AM1.5 spectrum), where the loss in number of low energy photons is compensated by the high energy of those absorbed. This sets the theoretical limit of the single junction cells at Shockley-Queisser of 31%. At record efficiencies of c.a. 11% there is still potential in the DSC field.

A sensitizer must have the following properties: (i) it must be firmly attached to the semiconductor oxide surface and inject electrons into the conduction band

with a unit quantum yield; (ii) its energy levels should be such that it can be regenerated rapidly via electron donation from the electrolyte or a hole conductor; and (iii) it should be able to sustain at least 10^8 turnovers under illumination corresponding to c.a. 20 years of natural sunlight.

At the moment there are three types of dyes [21-23] that can produce cells with AM1.5 conversion efficiencies over 10%, albeit with a volatile acetonitrile electrolyte solvent. However, these types of dye suffer from the drawback that they are based on the rare ruthenium transition metal. Other solely organic based dyes [24, 25], have also attained notable performances with efficiencies over 5%. These organic compounds are exciting because they should be easily synthesised and may not contain heavy metals.

The most widely used sensitizer is cis-bis(isothiocyanato)bis(2,2'-bipyridyl-4,4'-dicarboxylato)-ruthenium(II) bis-tetrabutylammonium (see Figure 7). It is popular because high efficiencies are obtained when used and because it is commercially available (e.g. from Solaronix). The efficiency of these dyes is due to the fact that they satisfy the conditions of a high extinction coefficient as well as fast electron injection into the oxide [26-29].

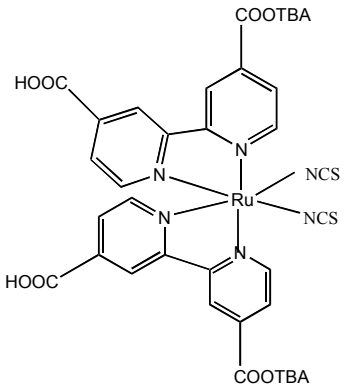

Figure 7 *cis*-bis(isothiocyanato)bis(2,2'-bipyridyl-4,4'-dicarboxylato)-ruthenium(II) bis-tetrabutylammonium, also commonly known as the N719 or Ruthenium 535-bisTBA dye.

Long-term stability of DSCs, though, is still poor [30] (especially under prolonged heating at temperatures over 80°C) due to, according to the authors, desorption of the dye. A similar ruthenium based dye with enhanced stability "cis-bis(isothiocyanato)(2,2'-bipyridyl-4,4'-dicarboxylic acid) (2,2'-bipyridyl-4,4'-dinonyl)-ruthenium(II)" (Z907) was developed [31] and later on improved with a higher molar extinction coefficient "cis-bis(isothiocyanato)(2,2'-bipyridyl-4,4'-dicarboxylic acid) (2,2'-bipyridyl-4,4'-bis(p-hexyloxystyryl))-ruthenium(II)" (K19) by Wang et. al. [32]. The evolution of efficiencies of three cells based on the N719, Z907 and K19 dyes are

compared over 1000 hours of thermal ageing. In this example, the N719 based cell efficiency dropped from an initial value of 7% to just over 4% whilst the K19 based cell only had c.a. 10% drop in efficiency from its initial 7% value. It should be noted that these systems were tested using a thermally stable and low vapour pressure electrolyte [31].

Haque et. al. [33] discuss the idea of engineering out "kinetic redundancy" in the electron transfer at the TiO_2|dye|electrolyte interface, meaning the kinetics of each step only need to be as fast as required for efficient electron collection. For example, the injection of electrons from the excited dye into the TiO_2 only needs to be slightly faster than the relaxation of the electron from the LUMO to the HOMO. There are several ways to manipulate these kinetics. The simplest of these and always employed in optimised DSCs are the addition of lithium ions and/or tertiary butyl pyridine (TBP). These tune the conduction band edge of the TiO_2 by modifying the surface dipole potential.

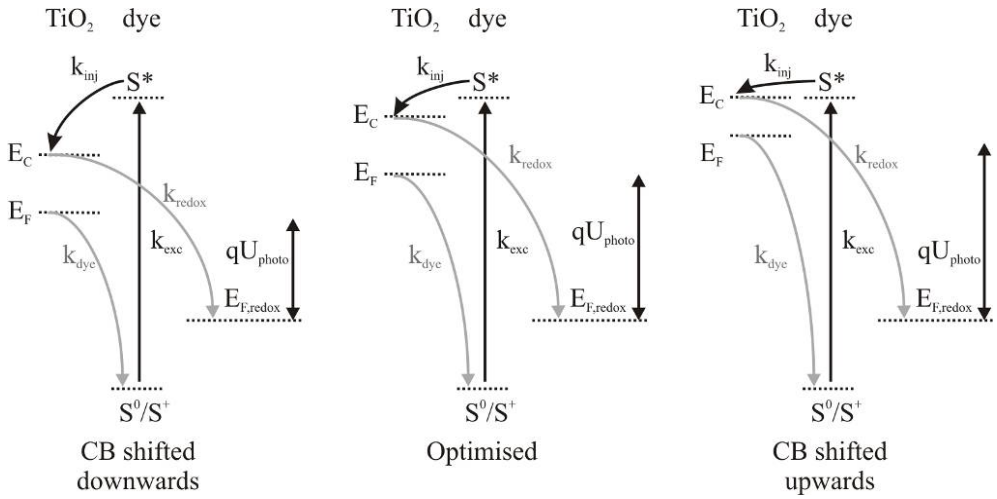

Figure 8 Schematic representation of how the conduction band edge is thought to shift according to the other energies in a DSC and how this influences the measured open-circuit voltage U_{photo}.

In the case of Haque et. al. [33], the effects of Li^+ and TBP are explored. The addition of Li^+ increased the short current density of the cells, however, at the expense of a lower open-circuit voltage and vice versa with TBP, the open-circuit voltage increased at the expense of the decreased short-circuit current density. An optimised balance was achieved when both additives were used in conjunction. The reasons are thought to be that the additives shift the position of the TiO_2 conduction band edge with respect to the LUMO/HUMO levels of the dye. The intercalation of the Li^+ positively shifts (downwards in the figures used here) the conduction band edge of the TiO_2 allowing for faster injection of electrons from the dye. However, this places the conduction band edge closer to the dye HUMO and electrolyte redox potential. It is unclear if

the reduced open-circuit voltage is solely due to the smaller potential difference between the conduction band edge of the TiO_2 and the redox potential, or if there is increased recombination because of the more favourable overlap of the energies. According to Haque et. al. [33] it appears that recombination is enhanced when the conduction band edge is closer to the redox potential. On the other hand, the addition of TBP negatively shifts (upwards in the figures used here) the conduction band edge and in the case exemplified by Haque et. al. [33], can to such an extent, hinder electron injection from the dye, resulting in a decreased short current density. However, this negative shift of the conduction band edge, even with the reduced injection efficiency of electrons, does result in an increased open-circuit voltage.

The kinetics involving the dye do not appear to present a problem for the DSCs, or these can be adjusted so that the injection efficiency is close to unity. However, the present dyes are not appropriately tuned to the solar spectrum, e.g. for the N719 dye, the peak absorption occurres at c.a. 2.3eV (530nm) instead of the optimum 1.4eV (900nm). Essentially, they suffer from not absorbing sufficiently in the red and near infrared.

3.2 The Redox Couple: Regenerating the Dye

The most important requirement for an efficient redox electrolyte is that it regenerates the oxidised dye molecule quickly (which is the case with the iodide ion at concentrations of 0.5M [34]). This is not only important so that the dye molecule is then ready to absorb another photon but also to prevent it accepting electrons from the supporting oxide.

The oxidised species of the electrolyte also have a role to play. The interaction between electrons in the oxide and the oxidised electrolyte species has to be poor to minimise recombination, yet the reduction of the species at the other side of the cell, at the counter electrode, has to be facile.

The redox couple of choice and the only one attaining significant (>10%) power conversion efficiencies is the iodide/triiodoide redox couple. The reaction sequence is thought to be [35-37];

$S + h\nu \rightarrow S^*$	photon absorption, electron excitation	7
$S^* \rightarrow S^+ + e_{CB}$	electron injection into oxide	8
$S^+ + I^- \rightarrow S + I^\bullet$	dye regeneration	9
$I^\bullet + I^- \rightarrow I_2^{\bullet-}$		10
$2I_2^{\bullet-} \rightarrow I_3^- + I^-$	disproportionation	11

The steps in equations 7 to 11 only describe the desirable interaction between the dye and the species of the electrolyte. The oxidised species of the electrolyte need also to be regenerated;

$I_3^- + 2e_{Pt} \rightarrow 3I^-$	electrolyte regeneration at the counter electrode	12

In principle, the reaction step in equation 12 is slow because two electrons are required. The asymmetry in the kinetics of a cell can be induced at the counter electrode by the use of catalyst. Platinum is the catalyst of choice but others have been explored. The high exchange currents at the platinum electrode using a thin cell with the typical electrolyte have been confirmed [38]. On the other hand, the reduction of the I_3^- species at the wideband TiO_2 oxide is slow [36, 37, 39], allowing for an electron concentration to build up to generate a significant voltage when illuminated.

Under illumination and at open-circuit (where there is no current flow though the external circuit), the injection and recombination rates are in equilibrium in the region of the TiO_2, i.e. there is no electron transfer to the I_3^- at the platinum counter electrode. Instead, electron transfer occurs via the oxide conduction band and surface states, and the TCO.

There are problems with the iodide/triiodide redox couple electrolyte. Firstly, iodine can be toxic in large doses (concentration >1mg/m^3) and highly oxidative, possibly making it unattractive for end user applications but also complicating maters in manufacturing. For large area photovoltaic cells, metal (e.g. gold) grids are often employed to reduce resistance. This however, is impossible with iodine present. Secondly, not only do the kinetics of the redox couple need to be favourable, but also the transport of charge to regenerate the dye needs to be facile. In the case of the iodide/triiodide redox couple,

acetonitrile along with thin spacing between the counter and the working electrodes, results in more than adequate diffusion limited currents. However, low viscosity solvents are usually volatile, complicating sealing. Alternative redox couples will have to be able to match performance of the iodide/triiodide couple in acetonitrile but be non-toxic and non-corrosive and easy to contain and manipulate.

The redox potential of the iodide/triiodide redox couple is adequate but not optimal. Pseudohalogens (e.g. $(SeCN)_2/SeCN^-$ and $(SCN)_2/SCN^-$ [40]) with more positive redox potentials were used as a substitute for the iodide/triiodide but yielded poor results, even though a larger photovoltage was expected.

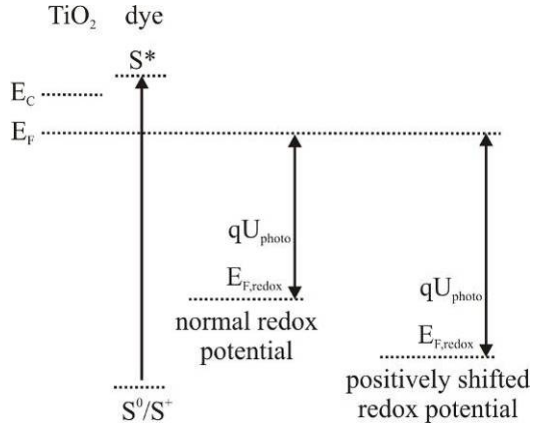

Figure 9 Schematic energy diagram demonstrating the idea of redox couple with a more positive redox potential.

In fact, it was found that the open-circuit voltages remained largely constant but the generation of current was severely affected, suggesting that the redox potential was too positive (below the HOMO of the dye) affecting the dye regeneration rate, i.e. the driving force due to a potential difference between the redox potential and the dye HOMO level was not large enough for electron transfer to occur. The authors suggested that the decreased photocurrent was due to electrons in the TiO_2 recombining with the oxidised dye before being collected, i.e. low diffusion length. This explanation may be incorrect because no efforts were made to suppress recombination via the TCO. However, the same type of redox couples were then found to work as well as the iodide/triiodide couple when SnO_2 was used instead of TiO_2 [41], highlighting the importance of band alignment.

An example of an outer one electron transfer system is the cobalt complex $Co(III)/Co(II)(dbbip)_2$ (dbbip = 2,6-bis(1'-butylbenzimidazol-2'-yl)pyridine) [42], exhibiting slow quasi-reversible electron transfer at gold and platinum electrodes. Interestingly though, cells employing this redox couple only

function if recombination via the TCO substrate is suppressed. The same is true when a solid organic hole conductor spiro(OMeTAD) [43] is used as an alternative. The primary reason for this is that both systems are outer sphere one electron transfer systems, therefore not necessitating catalysis for regeneration, i.e. the electron transfer occurs as easily at the FTO of the working electrode as it does at the counter electrode, thus not having the required kinetic asymmetry.

Gregg et. al. [44] demonstrated the importance of passivating the recombination pathways to obtain kinetic asymmetry and thus the electron density in the oxide required to generate a photovoltage. The redox ferrocene/ferrocenium (Fc/Fc^+) couple has a self-exchange rate several orders of magnitude greater than iodide/triiodide (10^7 $M^{-1}s^{-1}$ [45] compared to $5x10^2M^{-1}s^{-1}$ [46] respectively). When Fc/Fc^+ was employed in normal cells the photovoltaic effect was completely suppressed. This was attributed to recombination via the exposed parts of the TCO. When these exposed underlying conductive sites were passivated by electropolymerization of an insulating polymer, the photovoltaic effect was then present in the cells containing the fast redox couple.

The use of an organic hole conductor has been mentioned, but it is also possible to use a p-type inorganic semiconductor to regenerate the dye, e.g. CuSCN [47] and CuI [48]. This type of cell has the advantage over the organic hole conductors because of the lower cost of inorganic semiconductors. In addition, compared to liquid electrolyte cells, the packaging is greatly simplified. One of the challenges with this type of cell is managing to get a solid to fill the pores adequately, especially for thicker porous oxides layers. The cell structure is identical to that of a liquid electrolyte cell, still containing the dye, except the liquid part is substituted for a solid and this solid is ohmically contacted to the external circuit, e.g. with graphite or gold.

To facilitate the use of the iodide/triiodide redox couple, research has also gone into the use of gel or polymeric materials incorporating the redox couple [49-52]. However, these systems are affected by the low diffusion coefficients of the ionic species, limiting the short-circuit currents of the cells. However, concentration of the triiodide ion has to be kept low to minimise recombination, thus there is a trade off between higher concentrations to combat the low diffusion coefficients and the increased recombination rates. Nonetheless, cells have been reported with efficiencies of 5% to 6% demonstrating a viable alternative to the hole conducting solutions [49-52].

This research extends from studies of lithium ion batteries to improve stability against leakage under thermal stress [53]. The cells containing a polymer gel [31] along with a more hydrophobic dye (e.g. Z907) are the most stable when subjected to thermal stress, simulating real world applications.

3.3 The Counter Electrode: Regenerating the Electrolyte

The counter electrode function is to supply electrons to the redox system that regenerates the dye. It either requires chemical properties, so that catalysis can occur for the redox couples, or it can simply provide an ohmic contact to the p-type conductors. When hole conducting polymers [54] or p-type semiconductors are employed as substitutes for the redox couple, ohmic contacts are sufficient to complete the circuit. These are usually achieved by the deposition of gold or by pressing graphite.

Catalysis is required with the iodide/triiodide redox couple to initially break the I-I bond. If no catalyst is present [55], initial reduction of the I_3^- ion does not involve breaking this bond, but instead the product of the one electron reduction is the $I_2^{-\bullet}$ radical. It is then unclear if the intermediates undergo a second electron transfer to form I- or disproportionate into I_3^- and I.

The platinum counter electrode is not a component of a cell that requires extensive optimisation when used with the iodide/triiodide redox couple. Hauch et. al. [56] investigated the performance of several methods of depositing and post treatment of the platinum electrode. They found that a 2nm thick sputter-coated layer of platinum was sufficient for efficient cell operation when acetonitrile is used as the electrolyte solvent.

An example to help reduce the costs involved in the fabrication of DSCs could be the application of a carbon powder [57] instead of the platinum.

3.4 The Transparent Conducting Oxide (TCO)

The TCO can be obtained from companies such as Pilkington, who refer to their glass as Transparent Electrical Conducting glass (TEC). Research into the manufacture of these TCOs has matured into industry with companies specialising in delivery of the product. The reason for this maturity mainly lays in the flat screen market (ITO) and glazing for IR reflection (FTO). Their compositions tend to be c.a. 100nm thick fluorine doped tin oxide (FTO) or indium doped tin oxide (ITO) layers on a glass.

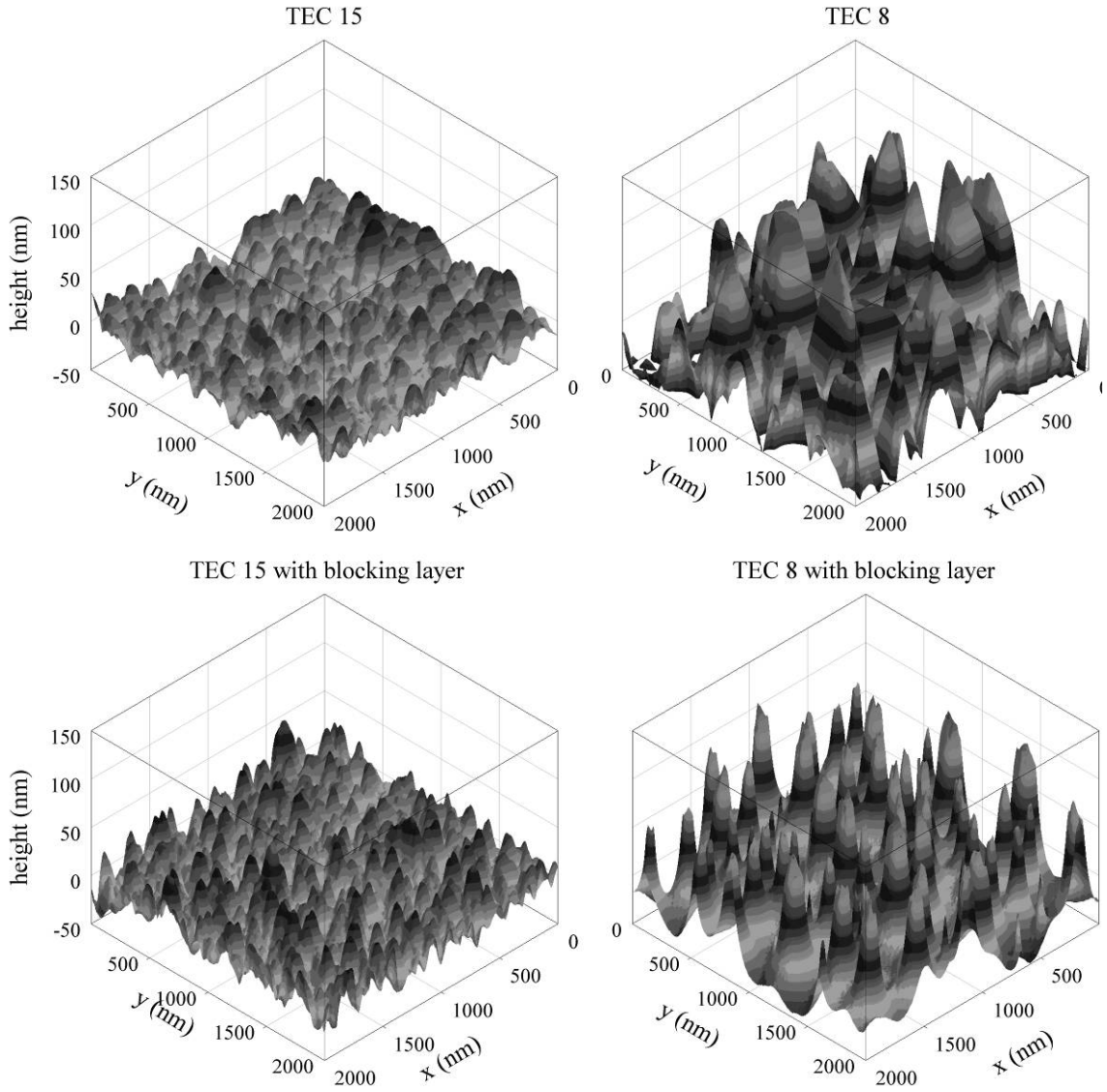

Figure 10 AFM images of TEC 15 (15Ωsquare) and TEC 8 (8Ωsquare) glass with and without the applied TiO_2 compact layer. TEC 8 TCO is visibly rougher than the TEC 15 TCO. In both cases, the addition of the TiO_2 compact layer (estimated to be 100nm thick) does not appear to flatten the surface of the TCO.

To produce efficient cells, the use of highly conductive and transparent TCOs is obviously preferred. However, when fundamental studies are desired, the role of the TCO may significantly influence the results. Cameron et. al. [58,

59] showed how even small exchange currents at the TCO significantly affect plots such as the open-circuit voltage dependence on light intensity. Nonetheless, recombination via the TCO is negligible under normal working conditions as other recombination routes become dominant (this is only true for cells incorporating the iodide/triiodide redox couple). Fortunately, quenching of this back reaction route is possible by the application of thin compact TiO_2 blocking layers [38]. However, we found that this suppression was not possible when highly conductive TCOs were used. This was attributed to the roughness of the TCO (TEC 8) being in the order of the thin compact TiO_2 film (c.a. 100nm).

One promising TCO is the flexible kind (e.g. polyethyleneterephtalate PET) allowing for roll-to-roll production and hence a potential for cost reduction. However, these flexible substrates are intolerant to the high temperature (450°C) required to make efficient cells, i.e. the sintering of the oxide layers. Alternative oxides and methods at lower temperatures (<150°C) for deposition of oxides on a conducting substrate are reviewed in the next section.

3.5 The Nanocrystalline Porous Oxide: Dye Substrate and Electron Acceptor

The role of the nanocrystalline porous oxide is to act as a support for the dye molecules and be a region for electron transport. To enhance the number of adsorbed dye molecules and thus increase the absorption coefficient of the film, porous structures are prepared, increasing the apparent cross-section by up to 1000. The band alignment of the wide bandgap semiconductor needs to be compatible with the absorber layer, i.e. its conduction band has to be at a lower energy than the LUMO of the dye. Since the semiconductor has a wide bandgap, it does not play an important role as an absorber and thus electron-hole pairs are not created. Record cells (>10% efficiencies) employ an anatase nanocrystalline porous TiO_2 film. Other oxides, such as ZnO and SnO_2, have also been explored.

For TiO_2 films, the strategies employed in the production of the films usually consist in preparing a suspension of 10nm to 100nm sized particles. These are then formed into a paste to apply as a film by either screen-printing or doctor blading. The organic binders used in the pastes also act as a spacer to control the film porosity. The heating stage burns out the organic binders but also sinters the nanoparticles together. There is a lack of clarity in the literature concerning techniques for preparing TiO_2 films. For example, the

current record 11.1% efficiency cell [18], refers to another paper [60] to describe the preparation of the cell, which in turn refers to another paper [61] describing the procedure used to prepare the TiO_2. Eventually the precursor is quite simply the commercially available TiO_2 nano powder, P25.

Of particular interest for cost reduction in the manufacture of the cells are low temperature alternatives, e.g. low temperature sintering [62-66], hydrothermal growth [67-69], CVD of Ti alkoxides [70-72], and electron bombardment [73]. One technique which provided considerable interest was the use of compression of a TiO_2 powder [74-78] with potential for roll-to-roll manufacturing on flexible substrates.

Recently, potentiostatic anodization has shown promise with the potential for large scale production of TiO_2 films, and has been used to prepare cells [79-84]. Although the authors claim that these systems exhibit longer (apparent) electron lifetimes, these are most probably due to the inherent inclusion of a blocking layer. The initial work was based on titanium sheets, requiring the illumination to be through the electrolyte, which is not ideal. Nevertheless, the setup using illumination through the electrolyte achieved conversion efficiencies of 6.9% [83] with a 20μm thick film. It would be more desirable to create these tubular arrays on TCO so that illumination does not have to be through the electrolyte. Initial attempts involving sputtering Ti on TCO followed by anodising resulted in film thicknesses of 360nm, exhibiting an efficiency of 2.9%. This is an impressive efficiency when considering the thickness of the film, achieving current densities of $8mAcm^{-2}$. The high current density for such a thin cell suggests a high internal surface area packing more dye molecules per unit volume. More recently, the same group of authors have managed to grow 3.6μm thick films on TCO, achieving efficiencies of 4.7%. With a relatively high current density of $10.3mAcm^{-2}$ and an open-circuit voltage 0.84V, it is the fill-factor of 0.54 that degrades cell performance. The authors attribute the poor fill-factor to additional series resistance due to the need for relatively thick blocking/barrier layer between the porous oxide and the underlying TCO. This method is not yet a low temperature route as it still requires thermal oxidation to remove remaining metallic islands. However, the anodization process could be optimised so as to not leave any metallic islands and thus not require high temperature thermal treatments.

Acceptable performances have been obtained using ZnO [85, 86], Nb_2O_5 [87]

and SnO_2 [88]. ZnO is attractive because it is a wide bandgap semiconductor with better carrier mobility [89] than TiO_2 whilst maintaining a similar conduction band edge. This band edge similarity and better carrier mobility should make ZnO a good candidate as the electron acceptor s. ZnO structures are also easy to obtain via a large variety of methods such as sol-gel [85, 90], chemical bath deposition [91-93] electrodeposition [94, 95] and vapour phase deposition [96]. The variety of morphologies obtained with relative ease from these techniques range from spherical particles, rods, and wires to hollow tubes. The drawback of ZnO generally lies with dye adsorption [97, 98], where, unlike TiO_2, the performance dyes of choice, do not anchor permanently to the surface of the oxide. However, this should not be a reason to stop investigation into ZnO as other dyes may be developed in the future.

3.6 Synopsis

There are various areas of interest in the DSC, but of particular interest for this work are the transport and recombination of electrons within the TiO_2 oxide layer in a complete working cell. The next section provides an overview of how the understanding of these properties has developed. Particular attention is given to the quasistatic approach [99] and the solutions to the continuity equation [100] describing diffusive electron transport within the TiO_2. These formulations are then expanded upon and tested with novel experimental techniques.

4 Theoretical Formulations for Diffusive Charge Transport and Recombination in the Oxide Phase of the Dye-sensitized Nanocrystalline Solar Cell

Progress in understanding the mechanisms governing the generation of energy and ability to extract it has been rather slow. Much initial work was based on investigating the independent components making up the DSC, components which have been highlighted in the previous section. This is most probably due to the almost infinite number of configurations a DSC can take. There is a large body of literature demonstrating large relative increases in efficiency, for poorly performing systems, somewhat obscuring the true mechanisms involved in high performing cells. To investigate the behaviour of electrons in a DSC several techniques have been developed which, when interpreted correctly, have led to a better understanding of the DSC. In some cases, the measurement techniques were developed before adequate theory. Only recently does it appear that one theoretical approach is managing to make coherent a wide range of experimental data.

This section initially introduces the relatively simple concepts of a current voltage curve and the incident photon to current conversion efficiency. Next explored is how the understanding of electron transport in the oxide phase developed, leading to two complimentary models, the quasi-static formulation and diffusive electron transport.

4.1 The iV Curve

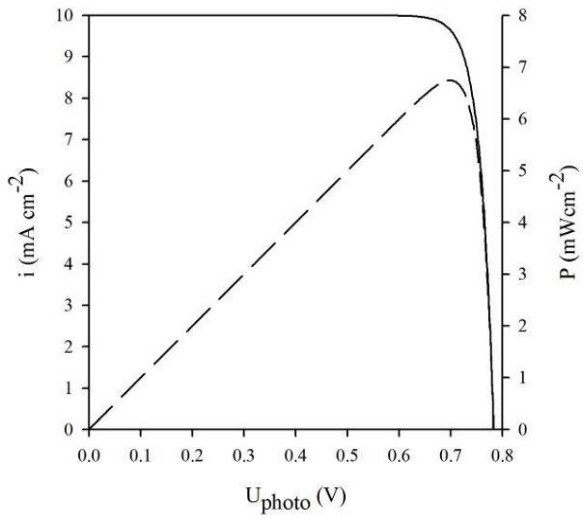

Figure 11 Typical iV curve and power curve of a solar cell. At short-circuit where there is no load across the cell, current is free to flow. As there is no load and thus no voltage there is no work done. At open-circuit, where there is no current flow, there is a maximum voltage but no current, so again no work is done. At the maximum power point (MP) the cell delivers the largest output power P=iV.

The optimisation of the iV curve is the most fundamental aim in the research of the DSC. Key factors are the short-circuit current density i_{SC}, the open-circuit voltage V_{OC}, the maximum power point (current i_{MP} and voltage V_{MP}) and the fill-factor giving the overall efficiency of a cell.

$$\eta = \frac{i_{SC}V_{OC}}{P_{incident}} \quad ff = \frac{i_{MP}V_{MP}}{P_{incident}} \qquad 13$$

$$ff = \frac{i_{MP}V_{MP}}{i_{SC}V_{OC}} \qquad 14$$

The ideal single pn-junction solar cell iV curve can be calculated using the well-known diode equation;

$$i = i_s\left\{e^{qU/\ k_BT} - 1\right\} - i_L \qquad 15$$

Equation 15 is simply the response of a diode with a generation term (i_L) in parallel. As the applied potential is increased, the recombination current increases exponentially (diode response). Initially, this results in a plateau region, where the current of the cell is independent of the applied bias, until the exponential response for the recombination current becomes dominant. In all solar cells, the objectives are to maximise the generation of current (i_L) and to minimise the saturation current (i_S).

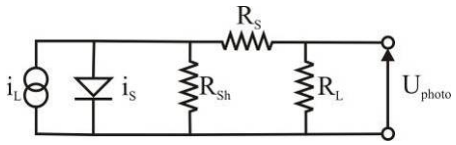

Figure 12 Solar cell equivalent circuit. Also included are some non-ideal characteristics, such as shunt resistance (R_{Sh}) and series resistance (R_S). Ideally, all the current should flow through the load resistor to maximise the voltage drop across it. To achieve this, the series resistance is minimised and the shunt resistance maximised.

The iV characteristics of a pn-junction solar cell are well understood and fuller descriptions can be found in any semiconductor device text book (e.g. Würfel [19] and Sze [101]). Most important in understanding the physics behind such a system is the formulation of the saturation current i_S. Generally, a lot of information can be extracted from fitting the iV curves of pn-junction solar cells.

DSCs also have iV curves as that depicted in Figure 11. However, there is still no consensus as to what physical information can be extracted from it, rather than just performance values. Nonetheless, there now appears to be a plausible theoretical formulation, which is explored in the next sections.

4.2 Incident Photon to Current Conversion Efficiency (IPCE)

The IPCE spectrum is a measure of how efficient the cell is at absorbing photons, of a specific wavelength, to generate current in the external circuit. The overall IPCE can be viewed as the product of four processes: the photon absorption efficiency (η_{abs}); electron injection into the oxide (η_{inj}); the collection efficiency of the electron (η_{col}) and the dye regeneration efficiency (η_{reg}).

$$IPCE(\lambda) = \eta_{abs} \times \eta_{inj} \times \eta_{col} \times \eta_{reg} \qquad 16$$

All four efficiencies depend on different properties. The absorption efficiency is determined by the dye's ability to absorb a photon (see Figure 13). The injection efficiency is a function of how well coupled the LUMO dye level is to the oxide conduction band. Electrons injected further away from the substrate are less likely to be collected as their transit time becomes comparable to their lifetime, thus determining the electron diffusion length. This is reflected by the collection efficiency. The regeneration efficiency of the dye is also important, in that as long it remains oxidised it can be a source of back electron transfer from the supporting oxide.

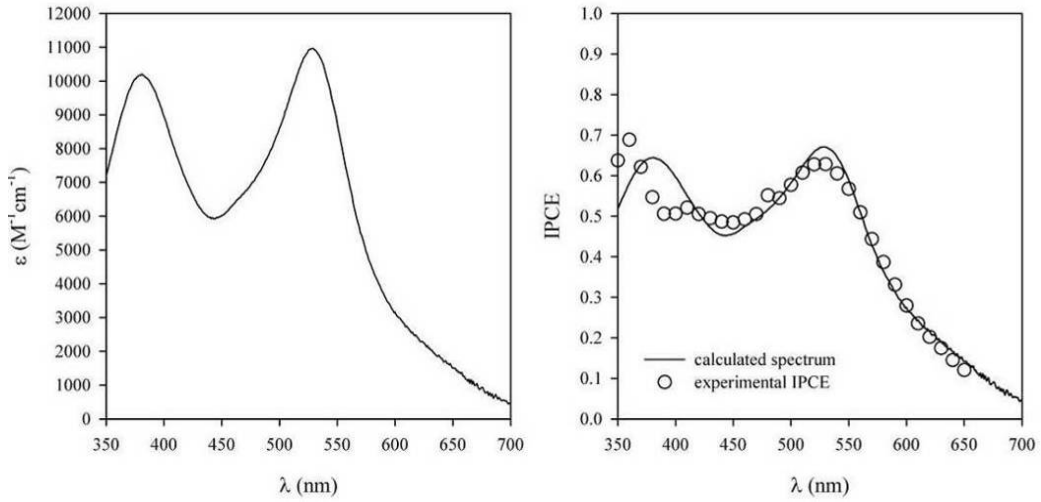

Figure 13 Left: Measured extinction coefficient of N719 dye in tertiary butanol/acetonitrile (1:1). Typical IPCE profile for a DSC employing the N719 dye with a calculated spectrum using the measured extinction coefficient. The IPCE was calculated by assuming a particle radius of 5nm occupying a cubic volume $8r^3$ and using a film thickness of 5μm. This results in a typical internal surface area 1570 times larger than the cross-section area. A dye footprint of 135Å^2 [102] was assumed and from this a volumetric dye concentration calculated. Beer Lambert absorption was assumed; $A=\varepsilon cx=-log(I_t/I_0)$ and $IPCE=1-10^{-A}=I_{abs}/I_0$. To make the spectrums coincide, a dye-loading factor of 0.25 was used. This to a certain extent is not surprising as most values used in the calculation have large uncertainties associated with them.

Generally, for optimised DSCs, the injection and collection efficiencies can be near unity. It is the ability to absorb light of various wavelengths that determines most the IPCE of a DSC.

The simplest way to increase the IPCE spectrum is to make thicker films and hence increase the optical path length for the incoming photons. The resultant calculated spectra for different film thicknesses are shown in Figure 14. Knowing the IPCE of a particular cell, the short-circuit density can be estimated by integrating the response over the incident irradiation spectrum (e.g. AM1.5 spectrum);

$$j_{SC} = q\int_0^\infty IPCE(\lambda)I_{sun}(\lambda)d\lambda \qquad 17$$

Record DSCs report current densities close to 20mAcm^{-2}. Ideally, for a single junction system where the absorption onset occurs for energies above 1.4eV, the absorbed photon density gives rise to a maximal photocurrent density of c.a. 30mAcm^{-2}. There is thus sensibly 10mAcm^{-2} that can still be extracted in DSCs. Looking at Figure 13 it is evident that a current performance dye (N719) is lacking in absorption in the infrared region.

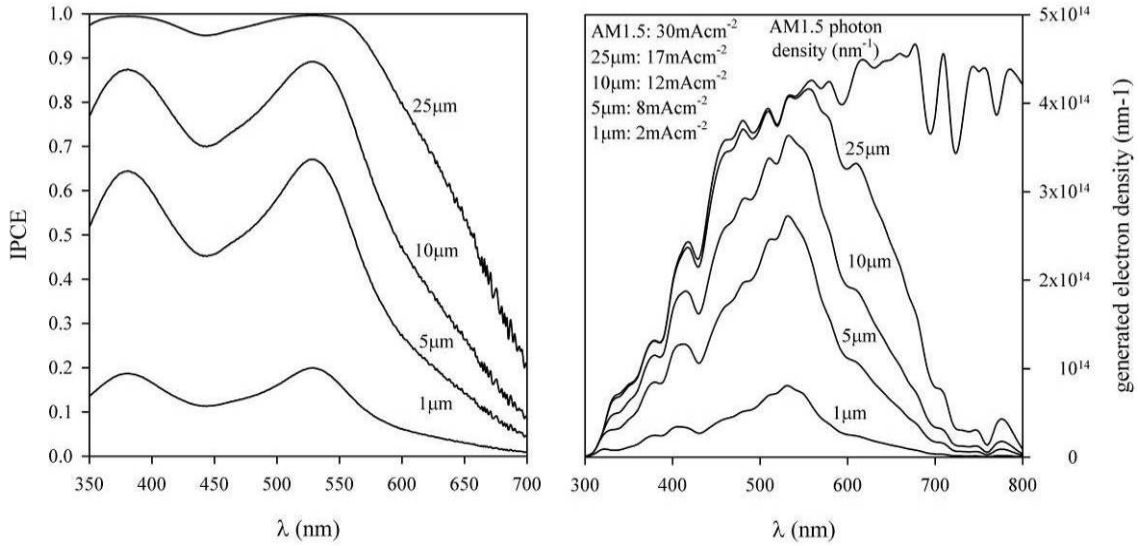

Figure 14 Left: Calculated IPCE spectra using the same parameters as those in Figure 13, except the film thickness was varied as shown. Right: Generated current/electron density for the different IPCE spectra. The ideal current density (30mAcm^{-2}) is that of a single junction system absorbing all photons of energy greater than 1.4eV (i.e. below 900nm).

With the currently available dyes, increasing the film thickness to absorb in the near infrared only has a marginal impact. In fact, reported record performing DSCs have film thicknesses of c.a. 20μm. As the extinction coefficient drops off significantly in the near infrared, the optical pathlength would have to be orders of magnitude larger than the thicknesses shown in Figure 14, for significant absorption to occur. Simple techniques to increase the optical path length by incorporating scattering layers or a reflective counter electrode will at best increase by a few times the optical pathlength. In addition, significantly thicker cells are limited by the diffusion length of electrons.

Designing dyes that absorb more strongly in the near infrared region up to 900nm could, by increasing the current density by 50%, push DSC efficiencies up from 10% to 15%. The result would be DSCs competing directly with commercially available modules.

4.3 Contrasting the Semiconductor Electrolyte Interface for Porous and non-Porous TiO_2 Electrodes

Interest in the behaviour of photoinduced generation and recombination of charge inside colloidal particles can be traced back to 1982 [103], almost a decade before the seminal Nature paper by O'Regan and Gratzel [17]. In this case, electron-hole pairs were generated by UV band-gap excitation in a colloidal suspension of TiO_2 particles, where electrons would then transfer to methylviolegen MV^{2+}, an electron acceptor. The authors described the process having three steps: (i) diffusion of electrons to the surface of the particle (or interphase), (ii) electron encounter with the electron acceptor at surface and (ii) electron transfer to the electron acceptor. Using mobility measurements for bulk TiO_2 crystals [104] and using the Einstein relationship (the equivalence of mobility and diffusivity) they used a value of $D=1.2x10^{-2}cm^2s^{-1}$ to estimate the transit time of an electron to the surface of the colloidal particles (r=10nm) to be only 10ps. From this rate, they deduced that the reduction kinetics of MV^{2+} were not limited by diffusion of electrons to the surface but by the interfacial electron transfer kinetics from the TiO_2 to the MV^{+}.

The relevance of this work is that initial estimates of the diffusion coefficient of electrons in the porous TiO_2 phase in a complete DSC, were orders of magnitude lower than that of bulk TiO_2 crystals. These low diffusion coefficients were speculatively attributed to distortion of the crystal structure at grain boundaries leading to enhanced scattering of electrons, localized states at grain boundaries acting as electron traps or because of the high surface area of the porous network, electron transport being strongly influenced by interfacial properties, such as ambipolar diffusion with species in the redox electrolyte. It now appears that the initial assumptions of diffusion coefficients close to that of bulk anatase TiO_2 are, according to the work presented, here more likely to be correct.

An interesting contrast is apparent when UV photocurrent spectra of compact TiO_2 films are compared to those of porous films. Lindquist et. al. [105] measured the collection of charge carriers in compact films in contact with a hole capturing electrolyte. In this case, a depletion region was created at the semiconductor electrolyte contact providing an electric field that assists in electron-hole pair separation. The width of this depletion region ($w=7.5nm$) was much smaller than the thickness of the compact film ($d=70nm$).

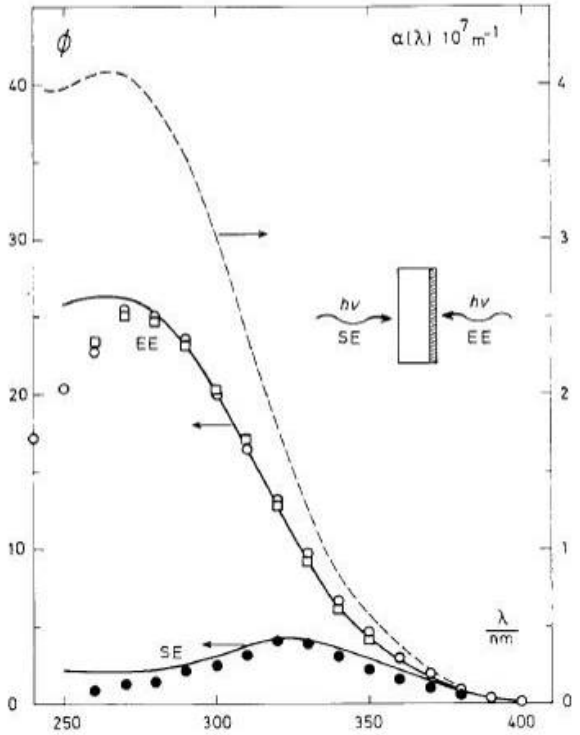

Fig. 9. Preparation 2a and 2b. The measured (□, ○, ●) and calculated (solid lines) quantum efficiency spectra depicted together with the absorption coefficient spectrum (dashed line) of TiO_2. Light incident upon the substrate-TiO_2 interface (SE) ● and upon the electrolyte-TiO_2 interface (EE) with □ and without ○ back contact of Al. Calculated curves are based on Eq. [1] and [7] with $d = 70$ nm, $w = 7.5$ nm, $L_p = 0$ nm, U (vs. SCE) = 1.00V.

Figure 15 IPCE spectra measured by Lindstron et. al. [105] for compact TiO_2 films in contact with a hole capturing electrolyte.

In this type of system, (see Figure 15) the collection efficiency of charge is not only governed by creation of electron-hole pairs but also by the efficiency with which they can be separated by aid of an electric field. The absorption coefficient of UV light in TiO_2 is such that essentially a sheet of electron-hole pairs is generated at the side on which light is incident. Thus, it is straightforward to understand that free electrons will be available when the generation of the electron-hole pairs is within the electric field, increasing the local concentration and thus providing a concentration gradient for diffusion to the substrate. In Figure 15 this is electrolyte side illumination (denoted EE). When the generation of electron-hole pairs occurs in a field free region, few are the pairs that can undergo charge separation before recombining. This is demonstrated by illumination through the substrate side (denoted SE).

Hagfeldt et. al. [106] performed similar photocurrent action spectra but using nanoporous films (see Figure 16). In essence, they found the action spectra to be the inverse of those found by Lindstrom et. al. [105]. Collection of charge separated electron-hole pairs was found to be more efficient the closer charge separation occurred to the substrate collecting electrode. They argued that

because the semiconductor electrolyte interface was interpenetrating, charge separation occurred homogeneously. Because of this, charge collection efficiency was then governed by how far electrons could travel before recombining, i.e. those closer to the collecting substrate were more likely to be collected.

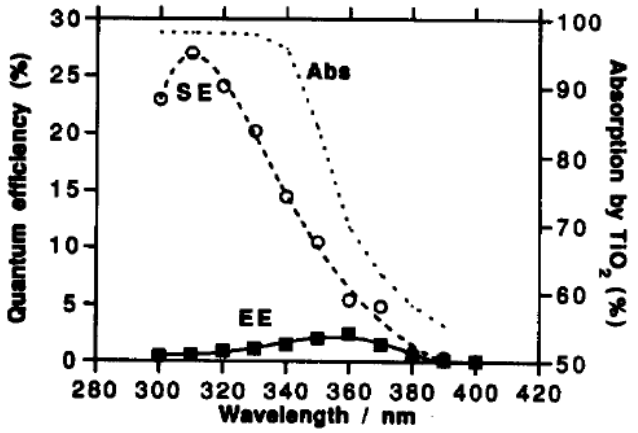

Fig. 3. The action spectra for SE and EE irradiation of a E_7 electrode. For comparison the absorption spectrum of the colloidal TiO_2 film electrode is also presented. The potential is 0.3 V. 0.1 M KSCN in water, pH = 5.

Figure 16 Photocurrent action spectra by Hagfeldt et. al. [106] on a porous TiO_2. The two geometries of illumination substrate side (SE) and electrolyte side illumination (EE) are compared.

Södergren et. al. [100] performed similar experiments but also formulated solutions to the continuity equation to explain the shapes of the curves. It was in this paper that solutions were also presented to describe the iV characteristics of a DSC based on diffusive transport.

4.4 Contacting the Titanium Dioxide and Consequent Negligible Electric Fields

To understand charge transport within the TiO_2, one has to initially appreciate the consequences of bringing a redox electrolyte and conducting electrode into contact with a semiconductor.

Let us consider a 5nm diameter particle, which is n-doped by oxygen vacancies (e.g. TiO_2) with a donor density of $10^{18}cm^{-3}$. Because of the high donor density, the Fermi level of the particle is close to the conduction band. It is generally estimated that the redox potential of the I^-/I_3^- couple is c.a. 1eV below the conduction band edge of the TiO_2 (e.g. see Figure 17). When the particle and electrolyte come into contact, electrons are extracted from the particle until the Fermi levels of the particle and redox couple are equilibrated. This results in a particle that has a net positive charge due to the ionised donors. The particle becomes fully depleted of free charge carriers and hence

insulating. The electric field associated to this depletion region is found by solving Poisson's equation;

$$\frac{\delta^2\phi}{\delta r^2} - \frac{2}{r}\frac{\delta\phi}{\delta r} = -\frac{\rho}{\varepsilon} = \frac{qN_D}{\varepsilon} \qquad 18$$

The solution for a particle of radius R (when the arbitrary zero potential is taken in vacuum at infinity);

$$\phi(r) = \frac{qN_D}{6\varepsilon}\left(R^2 - r^2\right) + \frac{qN_D}{3\varepsilon}R^2 \qquad 19$$

This variation in electrostatic potential is the distortion of the conduction and valence bands (see Figure 17). For the particle chosen and taking the relative electrical permittivity of TiO_2 to be $\varepsilon_r=100$, the potential difference between the centre and the edge of the particle is c.a. 0.75meV. This value is most sensitive to the particle radius, by increasing the radius to 10nm the potential difference is c.a. 3meV. Obviously, a larger doping density or smaller relative permittivity would give rise to larger potential differences. However, these values continue to be small when compared to the relative positions of the energies (E_C-$E_{F,redox}$≈1eV). In essence, this gives rise to a particle with an insignificant potential gradient and hence negligible electric fields.

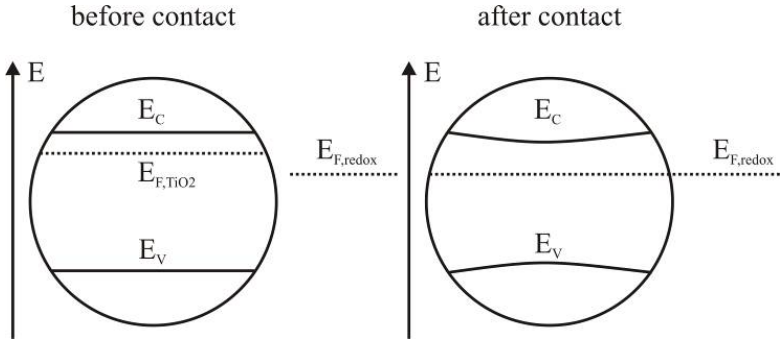

Figure 17 Fermi level equilibration of a TiO_2 particle with the I^-/I_3^- redox couple. The redox couple energy is generally estimated to be 1eV below the conduction band edge of TiO_2. The TiO_2 bandgap is c.a. 3.2eV. The band bending is exaggerated for clarity.

Peter [107] discusses the interesting point of electron channelling using an enhanced electric field, by either increasing the doping density or using larger particles. This confinement would prevent electrons reaching the surface to recombine with I_3^-, increasing the electron lifetime.

As discussed before, an energy gradient is required to sustain high current densities and the lower the electron mobility (or diffusion coefficient) the greater this gradient has to be. It will be shown that for a typical DSC the splitting of the Fermi level observed in the TiO_2 is about 0.5eV, orders of

magnitude larger than the potential difference due to the electric field.

The other contact/interface that exists at the TiO_2 particle, is with the degenerate ($N_D \approx 10^{20} cm^{-3}$) FTO. The dark equilibrium Fermi level is controlled by the redox electrolyte, buffered by the high density of the electrolyte species. Thus in principle, the initial relative positions of the Fermi levels of the TiO_2 and FTO are inconsequential.

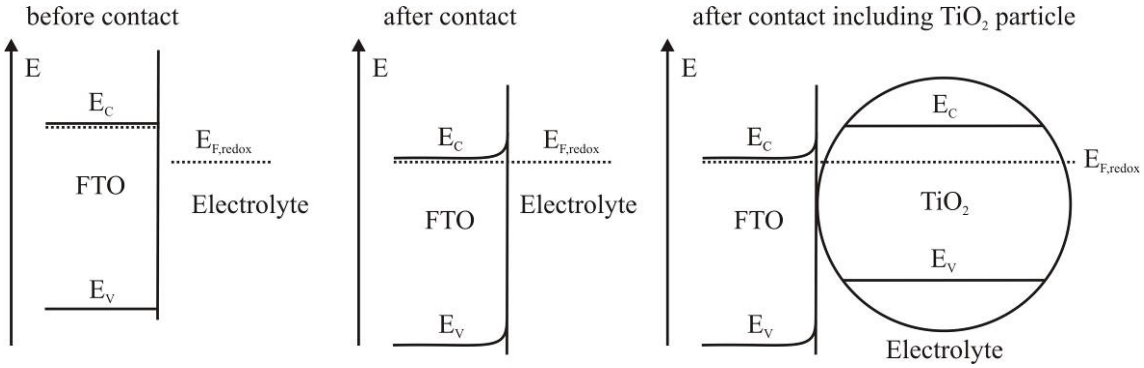

Figure 18 Example of band bending due to depletion that occurs when the n-doped degenerate FTO comes into contact with I^-/I_3^- electrolyte. The bandgap of $SnO_2(F)$ is c.a. 3.6eV and thus wider than TiO_2.

A depletion region is induced in the FTO. The barrier created may be energetically large but because of its reduced width, it allows for facile tunnelling. The depletion width is defined by;

$$w_{SC} = \sqrt{\frac{2\varepsilon}{qN_D}\left(E_C - E_{FB}\right)} \qquad 20$$

If we assume the flat band potential energy to be c.a. 1eV above the conduction band (the difference between the original position and final after contacting with the electrolyte) and maintaining the estimate of the doping density to be $10^{18} cm^{-3}$, the space charge width is c.a. 10nm, sufficiently small for tunnelling. Essentially, this means that the FTO|TiO_2|electrolyte interface behaves like a metal electrode.

However, when current is flowing it is unclear if the Fermi-level across the interface can be taken as continuous or if there is a significant barrier to extraction. If this is the case, then the voltage measure at the FTO may not be representative of the voltage of the TiO_2 at the interface.

Thus far examples of published results and some simple formulations point to the idea of no significant electric fields in porous TiO_2 and thus transport having to be diffusive.

4.5 Electron Recombination and the Open-Circuit Voltage

By definition, the open-circuit condition is where no charge flows through the external circuit. Thus, all electrons injected by the dye must be balanced by all the recombination routes. These routes have already been identified in section 3. For simplicity, the only route considered here is the recombination of electrons with I_3^-.

The electron injection rate can be defined as;

$$\upsilon_{inj}(\lambda, x) = \eta_{inj}\alpha(\lambda)I_0 e^{-\alpha x} \qquad 21$$

The rate of electron transfer to the I_3^- also determines the open-circuit voltage of a DSC. Section 3.2 only described the favourable routes involving the electrolyte species. The back reaction routes can be [107];

$$I_3^- + e_{TiO_2} \rightarrow I^- + I_2^{-\bullet} \qquad \text{electron recombination with } I_3^- \qquad 22$$

Followed by;

$$I_2^{-\bullet} + e_{TiO_2} \rightarrow 2I^- \qquad \text{second electron transfer involving electron recombination} \qquad 23$$

Or by the dispropornation reaction;

$$2I_2^{-\bullet} \rightarrow I_3^- + I^- \qquad \text{disporportionation} \qquad 24$$

If we assume the initial step (equation 22) to be the rate determining step, then the recombination rate can be described by;

$$\upsilon_{I_3^-} = k_{I_3^-} n\left[I_3^-\right] \qquad 25$$

As we have defined the injection rate of electrons to be equal to the recombination rate, we can now write (and also with $k_{I_3^-}\left[I_3^-\right] = \tau_n^{-1}$);

$$n = \frac{\upsilon_{inj}}{k_{I_3^-}\left[I_3^-\right]} = \upsilon_{inj}\tau_n \qquad 26$$

I.e. the electron density is directly proportional to the injection rate and inversely proportional to the I_3^- concentration and recombination rate constant. One way to increase the electron density and hence the electron

lifetime, could be to decrease the I_3^-. However, a lower concentration of redox electrolyte species would influence the maximum diffusion limited current of the cell. The concentrations generally employed provide a balance between electron lifetime (open-circuit voltage) and current densities (short-circuit current).

If the electrons are free to move in the conduction band, the photovoltage can be related to the electron quasi-Fermi level via the Fermi-Dirac function;

$$f_{FD} = \frac{1}{1+\exp\left(\frac{E_C - E_F}{k_B T}\right)} \qquad 27$$

Equation 27 reduces to the Boltzmann equation when E_C-E_F>>$k_B T$;

$$f_{FD}\left(E_C - E_F >> k_B T\right) \approx \exp\left(-\frac{E_C - E_F}{k_B T}\right) \qquad 28$$

The density of conduction band electrons thus is defined by the product of the conduction band states and the occupation probability;

$$n_C = N_C \exp\left(-\frac{E_C - E_F}{k_B T}\right) \qquad 29$$

The dark equilibrium density, where the Fermi level in the TiO_2 is that of the redox potential, is defined as;

$$n_{eq} = N_C \exp\left(\frac{E_C - E_{F,redox}}{k_B T}\right) \qquad 30$$

The photovoltage is given by;

$$qU_{photo} = E_F - E_{F,redox}$$

as

$$E_F - E_{F,redox} = \left(E_C - E_{f,redox}\right) - \left(E_C - E_F\right) \qquad 31$$

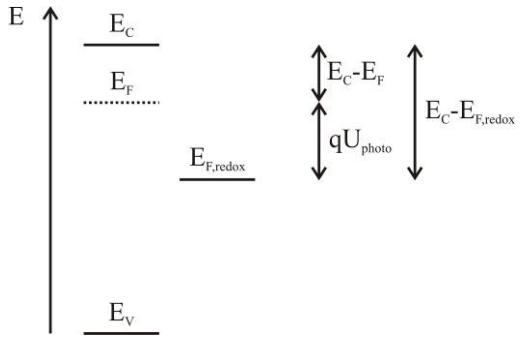

Figure 19 Energy diagram illustrating how the photovoltage is related to the relative position of the energy terms equation 31.

i.e. with this definition and using equation 30, the photovoltage is;

$$qU_{photo} = k_B T \ln \frac{n_C}{n_{eq}} \qquad 32$$

Examining equation 32, one realises that to obtain a typical photovoltage of 0.77V, the ratio of the conduction band densities must be 10^{13}. Typical values of E_C-$E_{F,redox}$≈1eV and N_C=10^{21}cm^{-3} mean that the dark equilibrium density of free electrons is 10^4cm^{-3}, and a density of 10^{17}cm^{-3} is required to obtain the typical photovoltage. Typically at 1 Sun, the absorbed photon flux for a 10μm thick film is c.a. 10^{17}cm^{-2}s^{-1}, translating to an absorption density of 10^{20}cm^{-3}s^{-1}, and thus according to equation 26, an electron lifetime of 1ms.

4.6 Steady-State Solutions to the Continuity Equation

A more formal approach is now taken to describe the steady-state electron transport within the porous TiO_2 phase of the DSC. Assuming electron transport is diffusive towards the underlying TCO, then a general one-dimensional diffusion equation for the electron density can be expressed as;

$$\frac{\partial n_C(x)}{\partial t} = D\frac{\partial^2 n_C(x)}{\partial x^2} + G(x,t) - R(x,t) = 0 \qquad 33$$

What this expression tells us is that the difference of generation (G) and recombination of electrons (R) is balanced by the diffusion of electrons. As we are only interested in the steady-state solution, the expression is set to zero.

For illumination through the TCO substrate (x=0) the generation term is defined as;

$$I = \eta_{inj} I_0 \alpha e^{-\alpha x} \qquad 34$$

This is the case if the Beer-Lambert law is applied, describing how light is absorbed in a non-scattering medium. The absorption coefficient is a function

of the optical cross-section of the dye and the density of active dye molecules attached to the TiO_2 surface. The values for I_0 and α are experimentally accessible. The intensity of illumination is set a priori, and the absorption coefficient can be measured knowing the thickness of the film. It is assumed for the purposes of discussion that the injection efficiency is unity.

$$I = I_0 \alpha e^{-\alpha x} \tag{35}$$

First-order kinetics are assumed for the recombination of conduction band electrons with I_3^- in solution, thus;

$$R = k_0 \left(n_C - n_{eq} \right) \tag{36}$$

The equilibrium electron density is present because it corresponds to the thermally generated electron density in the conduction band. This is expressed as;

$$n_{eq} = N_C \exp\left(- \frac{E_C - E_{F,redox}}{k_B T} \right) \tag{37}$$

Bringing all the expressions together, we have a differential equation to solve;

$$\frac{\partial n_C(x)}{\partial t} = I_0 \alpha e^{-\alpha x} + D_0 \frac{\partial^2 n_C(x)}{\partial x^2} - k_0 \left[n_C(x) - n_{eq} \right] = 0 \tag{38}$$

The terms back reaction rate constant and lifetime are equivalent ($k^{-1}=\tau$) and thus one can also write;

$$0 = I_0 \alpha e^{-\alpha x} + D_0 \frac{\partial^2 n_C(x)}{\partial x^2} - \frac{n_C(x) - n_{eq}}{\tau_0} \tag{39}$$

and;

$$R = \frac{n_C - n_{eq}}{\tau_0} \tag{40}$$

A first boundary condition that needs to be met is;

$$\left. \frac{dn_C}{dx} \right|_{x=d} = 0 \tag{41}$$

i.e. the concentration gradient of the electron density has to be zero at x=d, the point furthest away from the collection electrode. If it were not, electrons would be flowing in or out.

The electron density at x=0 can be defined in terms of the voltage as;

$$n_C(x=0) = n_{eq} \exp\left(\frac{qU_{photo}}{k_B T}\right) \quad 42$$

i.e. it is defined as a function of externally applied bias. It is by varying this imposed electron concentration that different profiles can be calculated for different voltages along the iV curve

Internally, the local quasi-Fermi level is related to the local conduction band electron density by;

$$n_C(x) = N_C \exp\left(-\frac{E_C - E_F(x)}{k_B T}\right) \quad 43$$

The values for the light intensity and the absorption coefficient are measurable. It is therefore the diffusion coefficient and electron lifetime that govern the resultant electron density. Externally, the current flowing out and the bias between the FTO and counter electrode can be monitored.

There are two ways to define the electron flux out of the TiO_2, but both are a function of the electron density at x=0. This sets the second boundary condition;

$$j = n_C(x=0)k_{ext} = -D_0 \left.\frac{dn}{dx}\right|_{x=0} \quad 44$$

In the following discussion, the extraction kinetics are ignored and simply set sufficiently high to ensure diffusion-limited extraction. The kinetic form of the expression is determined by the electron density, while the diffusive form is related to the way the electron density is varying at the contact. By raising the extraction kinetics by an order of magnitude, the electron density at x=0 will decrease by an order of magnitude, but they way it varies in space remains unchanged.

The two set boundary conditions allow the differential equation to be solved. The complete solution are found in Appendix A.

The flux of electrons at x=0 can be obtained as a function of voltage, and it can be shown that the general expression for the iV characteristic takes the form which is analogous to the diode equation [100];

$$j(0) = qI_0\left(1 - e^{-\alpha d}\right) - q\frac{D_0 n_{eq} d}{L_n^2}\left(e^{qU/k_B T} - 1\right) \quad 45$$

$$j(0) = qI_0\left(1 - e^{-\alpha d}\right) - q\frac{n_{eq} d}{\tau_0}\left(e^{qU/k_B T} - 1\right) \quad 46$$

Where;

$$L_n = \sqrt{D_0 \tau_0} \quad 47$$

This expression though is only true for an optimised cell, where the diffusion length is larger than the film thickness (L_n>3d), i.e. injected electrons are all collected at the TCO. Södergren et. al. [100] also demonstrate more general solutions for all diffusion lengths and for illumination through the electrolyte.

Equations 37, 45 and 46 highlight the that in order to plot the ideal iV characteristic, several unknown quantities are required. These are the conduction band density of states (N_C), the relative position of the conduction band edge with respect to the redox potential (E_C-$E_{f,redox}$), the diffusion coefficient (D_0) and the electron lifetime (τ_0). Before the uncertainties in these values are discussed, electron density profiles are illustrated.

Figure 20 illustrates a typical calculation for the electron density profile and the consequent QFL profile using what are thought to be reasonable values. What is evident is that there is a large concentration gradient in electron density, reaching a maximum at x=0. This build-up of electron density gives rise to significant QFL values of c.a. 0.5V for most of the film, except close to the collecting side. It will be shown in section 7 how this internal QFL can be probed directly.

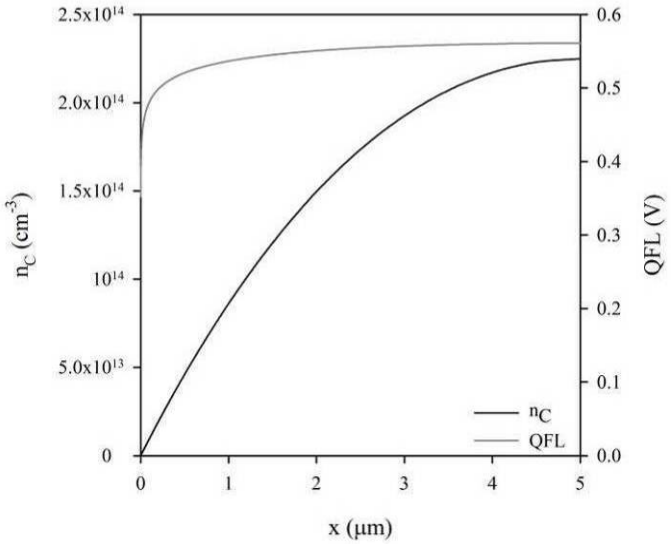

Figure 20: An example of the calculated electron density profile at short-circuit and the corresponding quasi-Fermi level (QFL). Physical parameters used were; $D_0=0.04\ cm^2s^{-1}$, $\tau_0=1\ ms$, $E_C-E_{f,redox}=0.95\ eV$, $N_C=10^{21}\ cm^{-3}$, $I_0=10^{17}cm^{-2}$, $\alpha=1000\ cm^{-1}$ and $d=5\mu m$. $k_{ext}=10^6\ cms^{-1}$, thus extraction of charge at the interface was diffusion limited, with the applied bias U being 0V.

The diffusion coefficient and diffusion lengths are chosen to ensure all electrons are collected (i.e. L_n=63μm in this case). When this is the case, the IPCE is simply then a function of the film thickness and the absorption coefficient. For this example, because of the chosen absorption coefficient and thickness, the IPCE is 39%, resulting in a photocurrent of 6.25mAcm^{-2}.

Increasing the diffusion coefficient (see Figure 21) has the effect of reducing the electron density, as a lower concentration gradient is required to maintain the same electron flux throughout the film. In the short-circuit case and where the diffusion length is sufficiently large, electrons only leave the TiO_2 system at the collecting electrode x=0, i.e. they do not recombine.

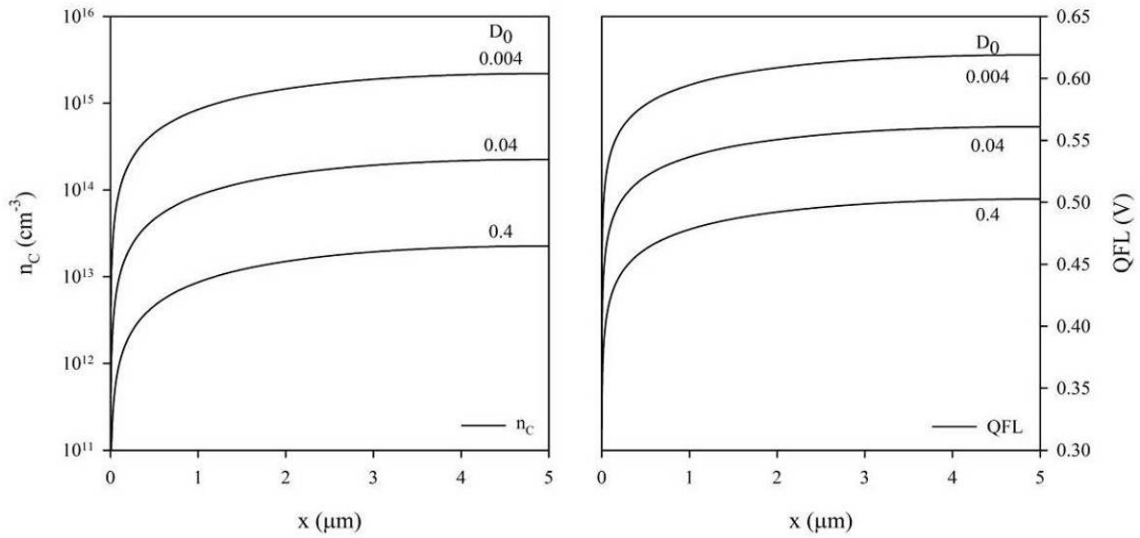

Figure 21: Example of how varying the diffusion coefficient affects the short-circuit electron density profiles and consequently the QFL profiles. All parameters are the same as those used in Figure 20, except D_0 (cm^2s^{-1}) was varied as shown.

When the diffusion length becomes comparable to the thickness, i.e. D_0=0.004cm^2s^{-1} and τ_0=1ms then L_n=6.3μm, the IPCE is affected, in this case decreasing to 34% from 39%, reflected by the decrease in the electron flux at x=0.

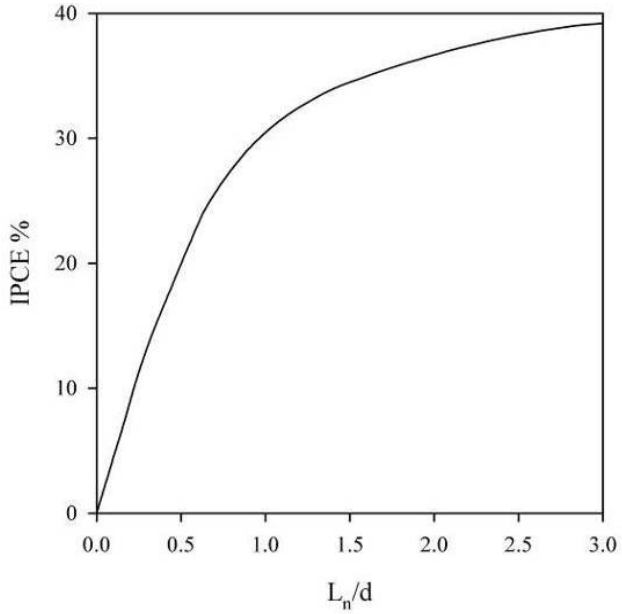

Figure 22 IPCE as a function of the ratio of the diffusion length to film thickness. When the diffusion length is greater than three times the film thickness all charge is collected before recombining. In this example, the IPCE reaches a plateau of 39% because of the combination of the film thickness and absorption coefficient limiting the light absorbed and hence the amount of charge generated.

The diffusion length is also reduced when the electron lifetime is decreased (see Figure 23). At short-circuit, the electron lifetime does not affect the electron density distribution, provided the diffusion length is significantly

larger than the film thickness. However, in the case where the lifetime is 1ns (see Figure 23), the majority of the electrons diffuse away from the TCO to recombine within the film. This occurs when the electron concentration gradient becomes negative, $dn_C/dx < 0$.

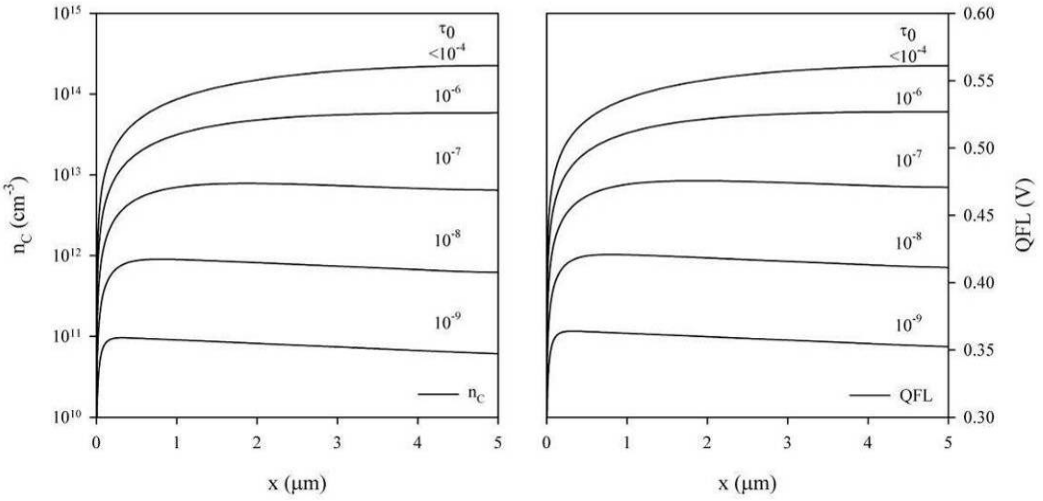

Figure 23: Example of how varying the electron lifetime will affect the short-circuit electron density profiles and consequently the QFL profiles. All parameters are the same as those used in Figure 20, except τ_0 (s^{-1}) was varied as shown.

Varying the incident photon flux (see Figure 24) has the a similar effect as varying the diffusion coefficient. When the generation rate is increased, the electron flux throughout the film has to adjust accordingly, and this is only possible by increasing the electron density.

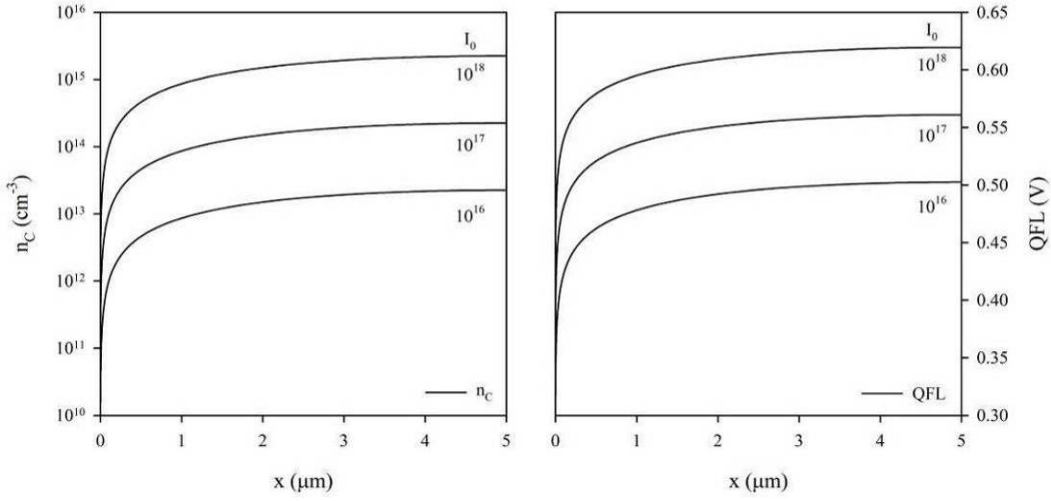

Figure 24: Example of how varying the photon flux affects the short-circuit electron density profiles and consequently the QFL profiles. All parameters are the same as those used in Figure 20, except I_0 ($cm^{-2}s^{-1}$) was varied as shown.

All the previous examples had an identical electron generation profile. One of the methods to improve the IPCE of DSCs is by developing dyes with higher

extinction coefficients.

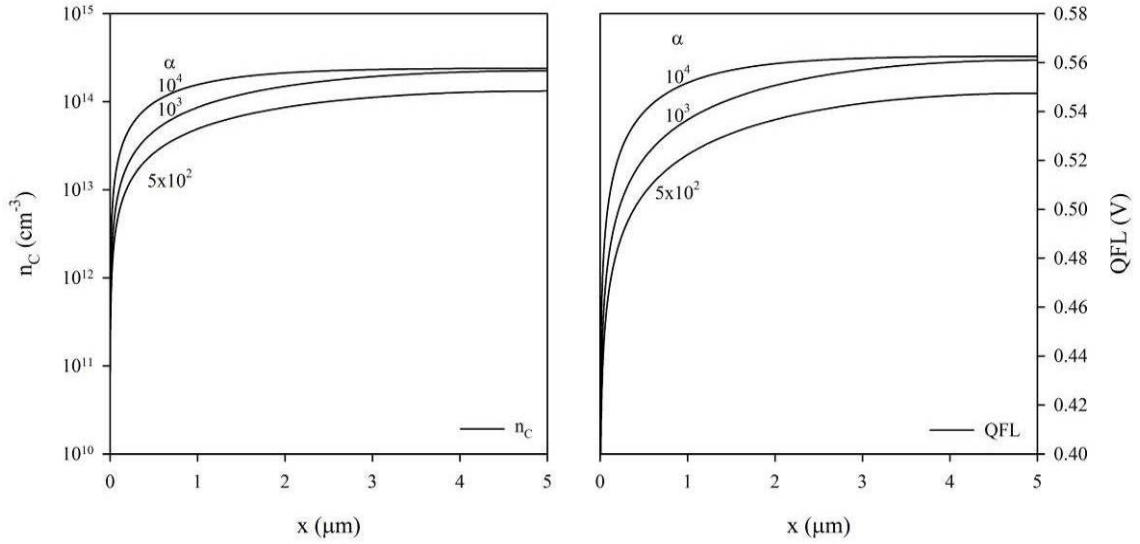

Figure 25 Example of how varying the absorption coefficient will affect the short-circuit electron density profiles and consequently the QFL profiles. All parameters are the same as those used in Figure 20, except α (cm^{-1}) was varied as shown.

Figure 25 shows how varying the absorption coefficient of the film influences the electron density profiles. In the case, of the high absorption coefficient of $10^4 cm^{-1}$, most electrons are generated close to x=0. In this case, the IPCE is essentially 100%, because all photons are absorbed within the space of 5μm, the film thickness. Larger absorption coefficients yield even flatter density profiles away from *x=0*. This is easily understood if one realises that as there is no significant generation of charge away from x=0, then there is no need for a density gradient (and hence diffusional flux) to compensate for the inhomogeneous generation. With lower absorption coefficients, the profile decreases in density accordingly, and the gradient at x=0 decreases. Again, as the generation of electrons is in fact more homogeneous, (i.e. a greater fraction is generated further away from x=0), then a larger gradient is required to compensate. In the case where $\alpha=500 cm^{-2}$, the IPCE drops to *20%* as fewer photons are actually absorbed.

Figure 26 and Figure 27 highlight another interesting question. The QFL is a function of the electron density (see equation 43), but this is physically defined by density of states and the relative position of the conduction band edge to the redox potential, i.e. for the same electron density, different QFLs can be calculated. Since the QFL can be probed experimentally, it is the electron density that will be uncertain because of the uncertainties involved in the position of the conduction band edge and the density of states.

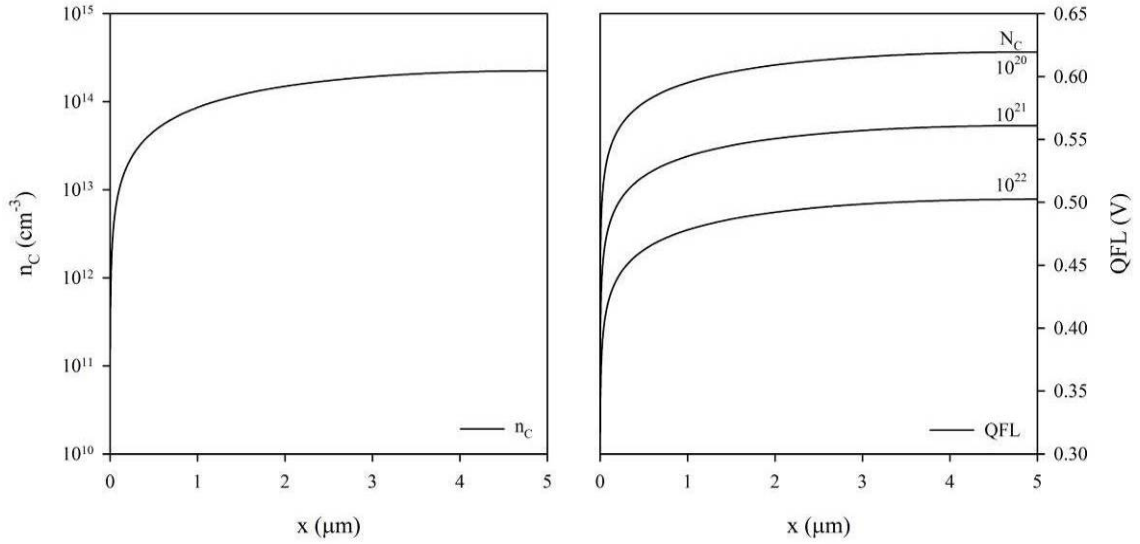

Figure 26: Example of how varying the conduction band density of states affects the short-circuit QFL profiles. All parameters are the same as those used in Figure 20, except (N_C cm^{-3}) was varied as shown.

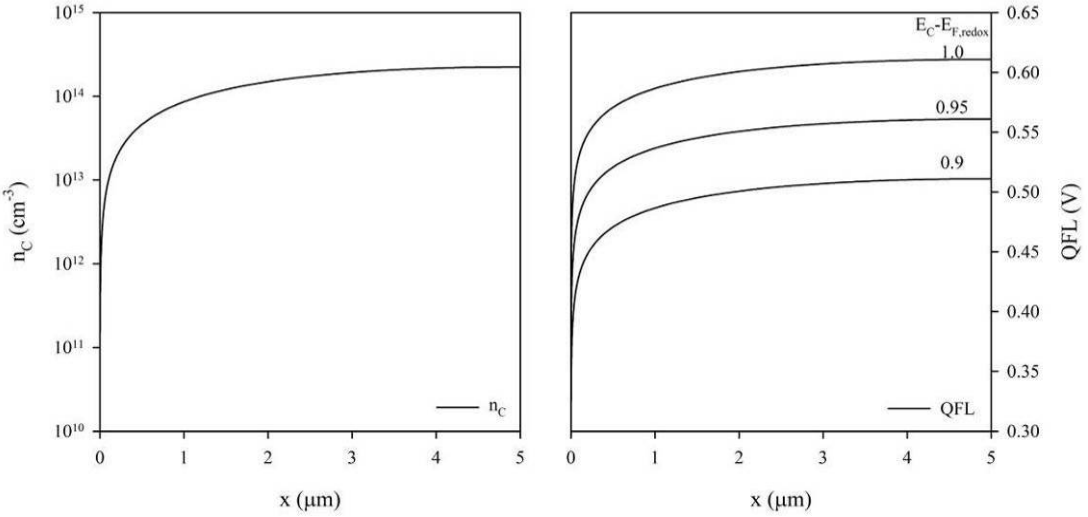

Figure 27: Example of how varying the difference between the conduction band edge and the redox potential affects the short-circuit the QFL profiles. All parameters are the same as those used in Figure 20, except E_F-$E_{F,redox}$ (eV) was varied as shown.

So far, the way in which the electron density profile adjusts has been explored for all the variables except for the changeable boundary condition at x=0, i.e. defining an applied bias (see equation 42).

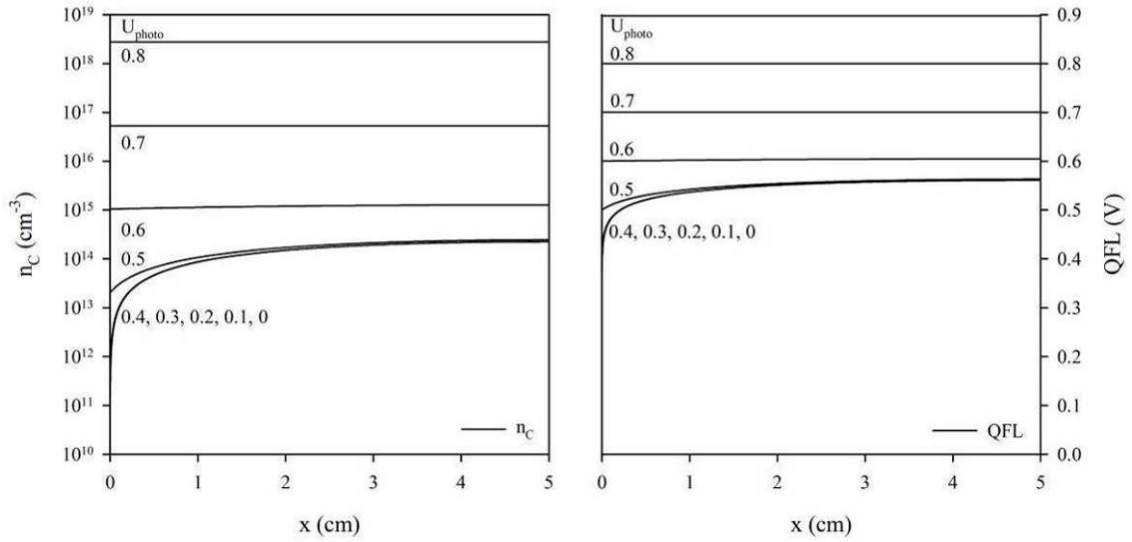

Figure 28: The effect of varying the applied bias. This is the boundary condition at x=0 that is modified to have an electron density corresponding to the applied bias (see equation 42). All parameters are the same as those used in Figure 20, except U_{photo} (V) was varied as shown.

As a bias is applied at x=0, the profile close to x=0, where the gradient is greatest, experiences the most change whilst regions further away remain relatively unchanged. It is only when the applied bias becomes equivalent in magnitude to the QFL for most of *x*, that the electron density then increases. This assumes that the a barrier at the FTO|TiO_2|electrolyte interface is negligible.

Before we can delve any further into the significance of the profiles with the iV curve, the dark recombination current has to be understood. For short-circuit conditions, the parameters were chosen so that the diffusion length of electrons was sufficient to ensure complete collection of all electrons. In this case, the profile is independent of the electron lifetime and hence, recombination. However, as the bias is increased the electron density of the film increases and thus according to equation 41, the recombination current increases. For example, with a photon flux of $10^{17}cm^{-2}s^{-1}$ and a resultant IPCE of 39%, $3.9x10^{16}cm^{-2}s^{-1}$ electrons are generated and are extracted under short-circuit conditions. For a 5μm film, this corresponds to a generation rate of $7.8x10^{19}cm^{-3}s^{-1}$. The electron density has a maximum value of c.a. $2.2x10^{14}cm^{-3}$ (at x=d), translating to a maximum recombination rate of $2.2x10^{17}$ $cm^{-3}s^{-1}$ (the electron lifetime being 1ms), i.e. two orders of magnitude less than the generation rate. However, as the electron density is increased by an applied bias to 0.6V, the electron density is c.a. $10^{15}cm^{-3}$ corresponding to a recombination rate of 10^{18} $cm^{-3}s^{-1}$. At this point, the collection efficiency of

electrons becomes affected, as recombination is occurring at $10^{18}s^{-1}cm^{-3}$ compared to $7.8x10^{19}s^{-1}cm^{-3}$ being generated. Biasing further, the electron density continues to increase (exponentially with U_{photo}) and quickly the recombination rate is equal to the generation rate, thus reaching open-circuit. As in this example, for the recombination rate to equal the generation rate ($7.8x10^{19}s^{-1}cm^{-3}$) the electron density needs to be $7.8x10^{16}cm^{-3}$, which corresponds to an open-circuit voltage of 0.71V. All this translates to the iV curve (see Figure 29), where for bias between 0V and 0.55V, the current density remains unaffected, because the electron density (cm^{-3}) is not sufficient for the recombination rate ($cm^{-3}s^{-1}$) to have any effect. However, the current density quickly decreases once the recombination current density becomes equivalent in magnitude to the injection current density.

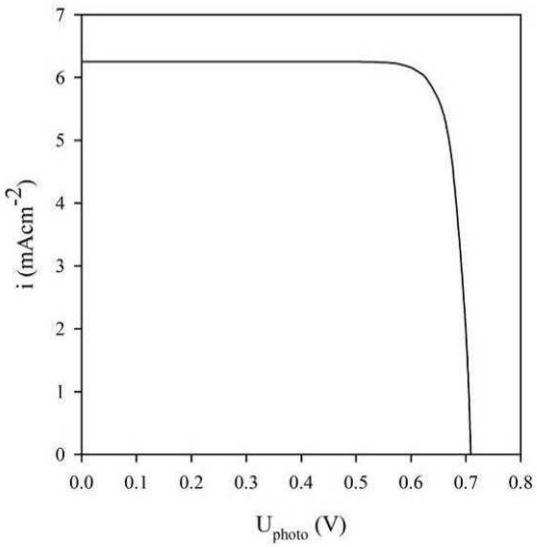

Figure 29: Resultant iV curve, i.e. the current density at x=0 calculated from Figure 28, whereby the current density is calculated according to equation 44.

The work presented here will use the results from this simple formulation to analyse measurements of when the QFL at x=d is probed by the incorporation of an internal sensing electrode.

O'Regan et. al. [108] inferred that the QFL at short-circuit under 1 sun illumination was of the order of 500meV. Other efforts have been made to test the idea of a large electron concentration gradient existing within the TiO_2 film. Boschloo et. al. [109] attempted this by holding a DSC under illumination at short-circuit, then ending the illumination and going from short-circuit to open-circuit conditions immediately. These results however are preceded by Schwarzburg and Willig [110] who in 1991 showed that there was a significant amount of charge stored in a DSC even at short-circuit.

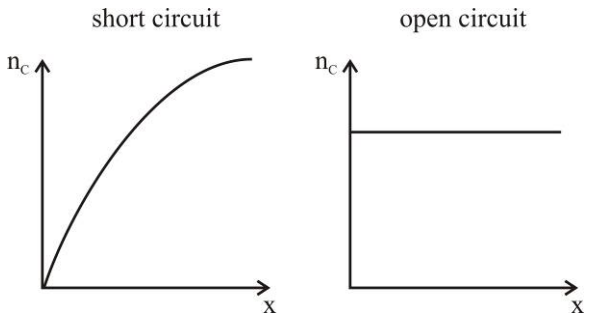

Figure 30 Idea of estimating the electron density at short-circuit under illumination is that the immediate open-circuit voltage (in the dark) gives an average value of the electron density throughout the film. The photovoltage is a measure of the QFL at x=0 and is related to the free electron density at x=0 by equation 42.

In Figure 31a, illustrated are photovoltage transients due to the short-circuit/illuminated to open-circuit/dark transition. There is a delay before the voltage reaches a maximum, due to the time required for the QFL profile to become homogeneous throughout the film. However, the large residual voltages measured (c.a. 200mV below the steady-state open-circuit photovoltage) confirm the large electron density gradient in the order of 0.5V.

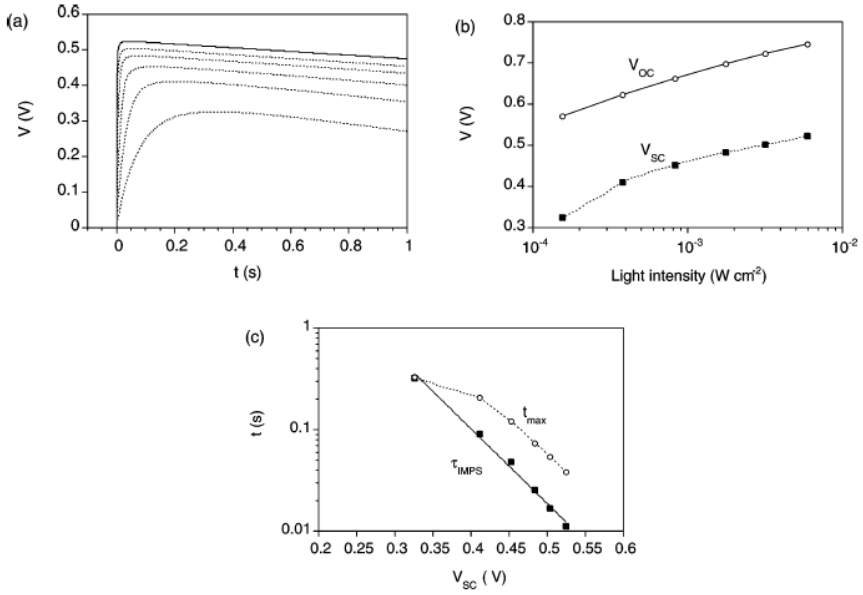

Figure 2. (a) Voltage transients of a nanostructured dye-sensitized solar cell recorded in the dark at open circuit, after illumination under short-circuit conditions. (b) Voltage maximum from (a), V_{SC}, as function of light intensity during the illumination period, and V_{OC} under steady-state illumination. (c) Relation between the time when voltage in panel (a) reaches its maximum (t_{max}, circles) and V_{SC}. Also, the transport time under continuous illumination (τ_{IMPS}, squares) is shown, where the drawn line is an exponential fit: $\tau_{IMPS} = 89 \exp(-16.9 V_{SC})$, $R^2 = 0.997$.

Figure 31: Measurements by Boschloo et. al [109] of the average QFL using the short-circuit/illumination to open-circuit/dark transition to measure the voltage rise.

These measurements also clearly show that there is a reservoir of electrons in the film. The timescale of the photovoltage decays present in Figure 31 (after the voltage has reached a maximum) are into the second regime, initially suggesting electron lifetimes in the order of seconds rather than ms. In fact, this is not the case but is due to a reservoir of electrons trapped in inter-

bandgap states.

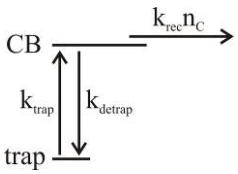

Figure 32 Electrons in the conduction band recombine with a rate $k_{rec}n_C$. However, this is compensated for by the release of further electrons from the traps. The net rate of release of electrons from the traps is, thus, equal to the recombination rate of conduction band electrons $k_{rec}n_C$.

When the light is turned off, the free electron density decreases because electrons recombine with an electrolyte species. If this were the only process involved, the photovoltage decay would be of the order of ms, the free electron lifetime. For the cells discussed in this thesis, we will demonstrate (as it is well known) electron densities of 10^{17} to 10^{18}cm^{-3} are possible under illumination at short-circuit, which is orders of magnitude greater than the calculated free electron densities (10^{14} to 10^{15}cm^{-3}). This large density of electrons is attributed to electrons trapped in inter-bandgap states. This large trap density has the effect of releasing electrons into the conduction band, thus contributing to maintaining a photovoltage. The decay of the photovoltage is not solely a function of the recombination rate of conduction band electrons, but it is also a function of how many trapped electrons there are to buffer the QFL decay.

The next sections deal with the nature of the inter bandgap traps.

4.7 Inter Bandgap States: Electron Trapping and its Implication in Dynamic Measurements

O'Regan et. al. [111] measured absorption spectra of porous TiO_2 films and observed how the spectra changed as a function of applied bias and modified surface conditions. Broad peaks in the infrared (IR) region were observed, which were attributed to inter-bandgap electrons absorbing photons. These results were in tune with earlier studies of IR absorption spectra of colloidal TiO_2 suspensions [112]. Absorption in the IR region was only observed when the films were populated with electrons, i.e. when a negative bias was applied. At zero bias and positive biases, IR absorption was not observed, i.e. when the film was depleted of free carriers. Interestingly, the authors also varied the pH of the electrolyte and shifted the conduction band edge [113] by adding isophthalic acid and catechol. These changes to the surface condition of the TiO_2 particles nonetheless, had only a minor impact on the observed spectra,

suggesting that the IR absorbing electrons were not at the surface but instead trapped within the particles or at grain boundaries.

Schwarzburg et. al. in 1991 [110] measured photocurrent transients of a DSC and attempted some simple modelling. They inferred that the photocurrent transients due to initiation or cessation of illumination were slow because of trapping of electrons in inter-bandgap states. It was also observed that the characteristic timescales for the transients became shorter as higher intensities were employed. If traps are present, electrons injected into the conduction band will fall into a trap when they encounter one and thus not contribute to the current output immediately. However, the quicker these traps can be filled, the quicker a photostationary state can be reached, hence the faster response times with higher injection rates. The authors modelled the system ignoring recombination. The two reasons given were that (i) TiO_2 has a large bandgap (3.2eV) and (ii) the dark Fermi level set by the redox potential of the electrolyte is 1.5eV above the valence band. In fact, it is probably more correct to say that recombination with thermally generated holes can be ignored because, 'recombination' occurs with the oxidised electrolyte species.

It was clear that the response of DSCs to dynamic measurements was non-linear, so attempts were made to measure and model the transport properties by linearising, using small perturbations superimposed over a larger DC value. These measurements revealed the striking fact that the inferred diffusion coefficients and electron lifetimes varied considerably depending on the light intensity.

An example of this approach is provided by Peter & Wijayantha [114] who measured the diffusion length over several orders of magnitude of light intensity. The authors concluded that although the electron lifetime and diffusion coefficient varied considerably over several orders of magnitude of light intensity, their product (the diffusion length) did not. The electron lifetime was observed to decrease, while the diffusion coefficient increased as the light intensity increased, both following a power-law dependence as shown in Figure 33.

The authors attributed the intensity dependence of the electron lifetimes to second order kinetics of electron recombination with I_3^-, and the dependence of the diffusion coefficient was explained by multiple trapping and detrapping.

Several other subsequent studies reached the same conclusion that the

electron lifetime decreased while the diffusion coefficient increased with light intensity e.g. [115-120]. It is now clear that the measured lifetimes and diffusion coefficients are in fact a multiple and fraction (respectively) of their true values, where this fraction is governed by the nature of the trapping and detrapping of electrons.

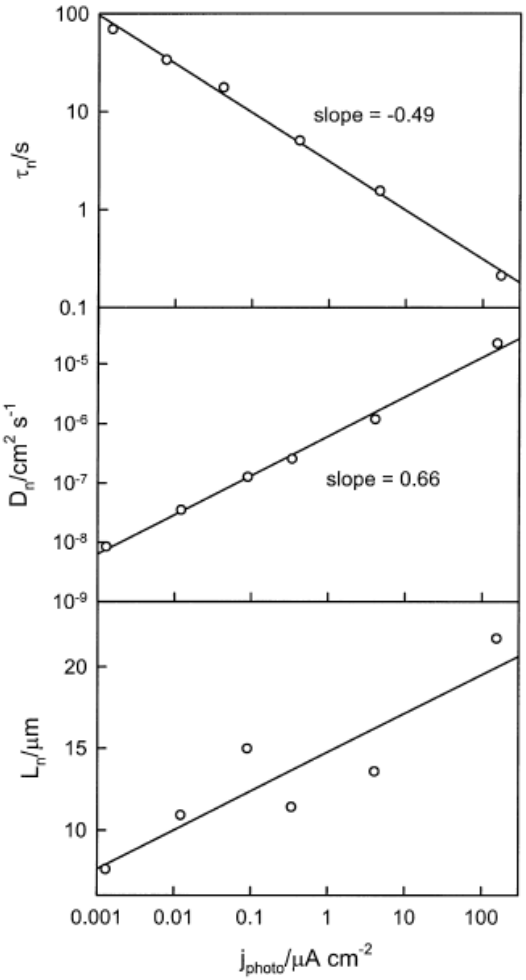

Fig. 3. Dependence of τ_n, D_n and L_n on dc short circuit photocurrent density.

Figure 33: Measured electron lifetimes, diffusion coefficients and thus diffusion lengths as a function of light intensity (or short current density) by Peter & Wijayantha [114].

To summarise, the 'electron lifetime' measured by dynamic methods is influenced by trapped electrons. Once electrons in the conduction band recombine with an oxidised electrolyte species, this electron is then substituted by one from a trapped state. If the number of trapped states is significant, a significant amount of time is required to allow all electrons to recombine. This explains the surprisingly long measured electron lifetimes (>1s). As for the diffusion coefficient, the same idea applies because, as electrons are injected, they become trapped before arriving at the FTO for collection. Again, if the density of traps is significant, then a significant number of electrons are trapped and the measured photocurrent transient is

slow, giving rise to surprisingly small diffusion coefficients ($10^{-5}cm^2s^{-1}$), several orders of magnitude lower than the value of anatase TiO_2.

The origin of the inter bandgap trap distribution observed in nanocrystalline TiO_2 is not well understood. For most data presented in the literature, the traps appears to follow an exponential distribution that can be made to fit the expression in equation 56. A debating point is whether or not the trap sites are recombination sites. If they are recombination sites, they then need to be localised within a tunnelling distance of the electrolyte species. Another problem lies in the transport mechanism, which can involve tunnelling from trap site to trap site.

The trap distribution is most probably a function of the TiO_2 film preparation, and thus may vary significantly, making comparison difficult. Interestingly though, if the trap nature is that described in section 4.8 then it is inconsequential to the performance of the DSC, acting simply as a temporal buffer affecting dynamic measurements.

Not only is the preparation of the TiO_2 important, but additives to the electrolyte (tertiary butyl pyridine) and post treatments to the film (TCl_4) may have positive effects in preventing surface states acting as recombination sites.

in passivating the surface traps which act as recombination sites. However, care must be taken in interpreting results of dynamic measurements since they may be affected by electron transfer (shunting) at the FTO/electrolyte interface. Cameron et. al. [58] showed that the temporal photovoltage decay is significantly different if the FTO substrate is passivated by use of a compact blocking layer. In this case, the recombination via the substrate is demonstrated to be the dominant factor affecting the temporal profile of the photovoltage decay at longer times, rather than homogeneous recombination throughout the film. Analysis of previous work or even current work of others on the nature of the traps and their passivation is difficult to analyse, because a blocking layer at the FTO/electrolyte interface was not employed to prevent shunting.

This influence of traps on transport and recombination was elegantly formulated by Bisquert & Vikhrenko al. [99].

4.8 The Quasi-Static Formulation

Bisquert & Vikhrenko [99] start by differentiating between the information which can be extracted from steady-state and dynamic measurements. It should be noted that the information acquired from steady-state measurements is what is of interest for determining photovoltaic efficiency.

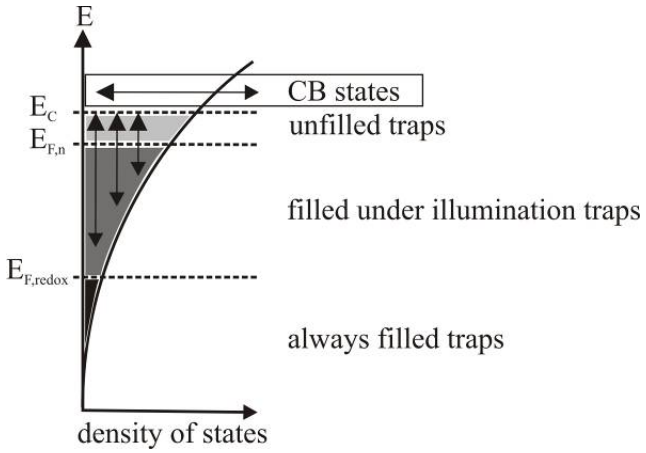

Figure 34 Schematic representation of the multi trapping mechanism with an exponential trap distribution. Traps below the redox potential are always filled. As the quasi-Fermi level is increased, traps below this energy will be filled, while those above it remain empty. However, there is an equilibrium of conduction band electrons constantly trapping, and trapped electrons detrapping. It is generally found for DSCs that the trap distribution follows an exponential profile, their density increasing as a function of energy.

The multi-trapping model was first introduced by de Jongh & Vanmaekelbergh [119]. The crucial assumption of the model is that transport of electrons only occurs by those electrons in the conduction band and recombination also only occurs via the conduction band. Thus, the trap states are solely states with an associated capture and release rate, where electrons remain localised and passive, contributing only to the occupation of the trap (see Figure 32).

For a single type of trap, and applying conservation of free and trapped electrons and diffusive transport, the following expressions can be induced;

$$\frac{\partial n_c}{\partial t} = -\frac{\partial J}{\partial x} - r_c n_C \left(1 - f_t\right) + r_r N_t f_t \qquad 48$$

where;

$$J = -D_0 \frac{\partial n_C}{\partial x} \qquad 49$$

i.e. the rate of change of the conduction band density of electrons is governed by diffusive transport and by the rates of trapping and the rate of detrapping.

$$\frac{\partial f_t}{\partial t} = -r_c \frac{n_c}{N_t}\left(1 - f_t\right) - r_r f_t \qquad 50$$

The rate at which the traps are emptied and filled is governed by the capture rate r_c and the release rate r_r. The rate constant for electron capture is a function of the thermal velocity of electrons, the capture cross-section and the density of traps such that;

$$r_c = N_t v s_n \qquad 51$$

Shockley-Read-Hall statistics determines the thermal release rate of electrons;

$$r_r = \frac{N_C}{N_t} r_c \exp\left(-\frac{E_C - E_t}{k_B T}\right) \qquad 52$$

At thermal equilibrium in the dark when the rates of trap emptying and filling are equal $\partial f_t / \partial t = 0$, the density of free and trapped electrons are governed by the position of the quasi-Fermi level.

We now define the quasi-equilibrium condition as a situation where the change from one equilibrium state to another can be visualised as a series of intermediate steps also at equilibrium. In our case, the property that is changed is the position of the Fermi level by the change in electron density. This quasistatic condition is;

$$\frac{\partial n_t}{\partial t} = \frac{\partial n_t}{\partial n_C}\frac{\partial n_C}{\partial t} \qquad 53$$

i.e. free electrons and trapped electrons maintain a common equilibrium at all times even when the system is displaced away from equilibrium. This signifies that the trap relaxation time has to be significantly faster than the processes which are to be measured, e.g. photovoltage and photocurrent transients. This is also true for measurements in the frequency domain, where the perturbation frequency has to be below the relaxation frequency for the quasistatic condition to hold.

Bisquert & Vikhrenko [99] go on to show that the apparent diffusion coefficient can be expressed as a function of trap occupancy and the position of the Fermi level;

$$D_n = D_0\left(1 + \frac{\partial n_t}{\partial n_C}\right)^{-1} \qquad 54$$

It is generally found that the trap distribution for DSCs can be approximated to an exponential profile with the trap density of states increasing towards the conduction band edge from the redox potential (see Figure 34).

$$g(E_F) = \frac{N_t}{k_B T_C} \exp\left(\frac{E_F - E_C}{k_B T_C} \right) \quad 55$$

The occupancy of the traps as a function of the QFL is then given by the product of the density of states and the Fermi-Dirac function. Using the zero Kelvin approximation (E_F-E_C>>k_BT) so that the probability of a trap being filled is ½ when E_T=E_F, is 1 when E_T<E_F and 0 when E_T>E_F, then the occupied trap density as a function of the QFL is given by;

$$n_t = \int_{-\infty}^{E_F} FD \times g(E_F) dE_F = N_t \exp\left(\frac{E_F - E_C}{k_B T_C} \right) \quad 56$$

we can differentiate to obtain one of the terms in equation 54;

$$\frac{\partial n_t}{\partial E_F} = g(E_F) = \frac{N_t}{k_B T_0} \exp\left(\frac{E_F - E_C}{k_B T_C} \right) \quad 57$$

Since the conduction band density of states is given by;

$$n_c = N_C \exp\left(-\frac{E_C - E_F}{k_B T} \right) \quad 58$$

we can again differentiate to obtain another term in equation 54;

$$\frac{\partial n_c}{\partial E_F} = \frac{N_C}{k_B T} \exp\left(-\frac{E_C - E_F}{k_B T} \right) = \frac{n_C}{k_B T} \quad 59$$

We can now calculate the apparent diffusion coefficient;

$$D_n = D_0 \left(1 + \frac{N_t}{n_c} \frac{T}{T_C} \exp\left(\frac{E_F - E_C}{k_B T_C} \right) \right)^{-1} \quad 60$$

A similar expression has been derived for the electron lifetime by Zaban et. al. [121];

$$\tau_n = \tau_0 \left(1 + \frac{\partial n_t}{\partial n_C} \right) \quad 61$$

and again with an exponential trap distribution, one can define the apparent electron lifetime;

$$\tau_n = \tau_0\left(1+\frac{N_t}{n_c}\frac{T}{T_C}\exp\left(\frac{E_F - E_C}{k_B T_C}\right)\right) \qquad 62$$

Interestingly, even though the apparent electron lifetime and diffusion coefficient vary with the position of the QFL, their product results in the electron diffusion length, since it is easy to show that;

$$L_n = \sqrt{D_0\tau_0} = \sqrt{D_n\tau_n} \qquad 63$$

This definition, though is, only true when the QFL is the same when the apparent electron lifetime and diffusion coefficient are measured. The plots in Figure 35 represent how the apparent diffusion coefficient and electron lifetime vary depending on the position of the QFL. As the free electron density becomes comparable to the trapped electron density, the effect of trapping is diminished. This is observed in the flattening of the profiles, with the apparent values (D_n and τ_n) reaching their bulk values (D_0 and τ_0).

The broken lines in Figure 35 are to highlight a crucial point. These are representative of what would be measured at constant illumination of c.a. 1 sun intensities. We have seen how the QFL varies along the iV curve, with typical variations from 500mV (short-circuit) to 700mV (open-circuit) for the same illumination.

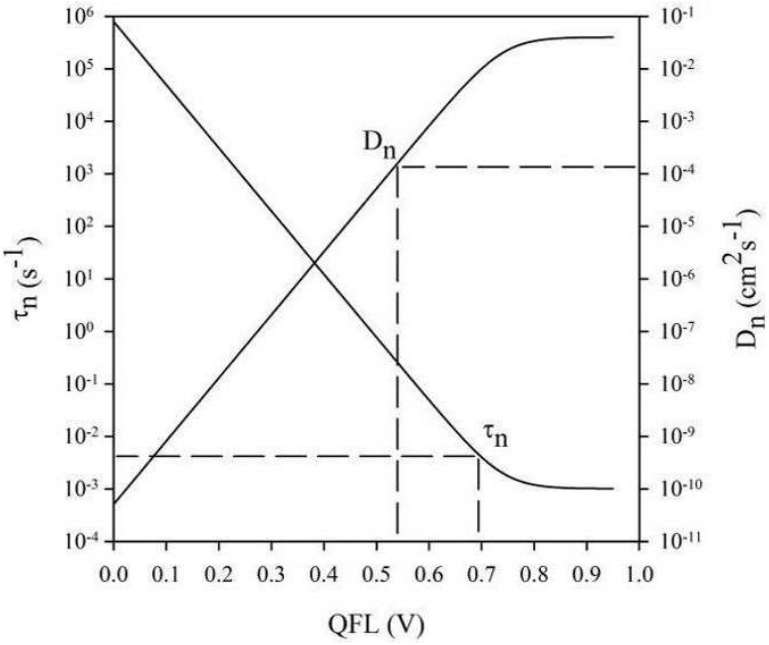

Figure 35: Example of how the apparent diffusion coefficients and electron lifetimes vary according to the expression in equations 60 and 62. The parameters used were; D_0=0.04cm^{2}s^{-1}, τ_0=1ms, T=295K, T_C=1000K, N_t=10^{19}cm^{-3}, E_C=0.95eV and N_C=10^{21}cm^{-3}. The broken lines represent the typical values that would be measured using typical techniques (IMPS and IMVS, see section 5) at QFLs typical of 1 sun intensities at short-circuit and open-circuit.

Up to recently, attempts to measure the diffusion length of electrons were based on intensity dependence of the apparent electron lifetimes and diffusion coefficients [114, 122-124]. Because the QFL is lower at short-circuit than at open-circuit, the then measured electron lifetime is lower and so too is the diffusion length. If the diffusion coefficient of electrons is to be estimated by measuring the apparent electron lifetimes and diffusion coefficients, these need to be done at a constant QFL and not illumination. An example of measurements at constant illumination was done by Peter & Wijayantha [114] (see Figure 33). The problem is that at open-circuit, the QFL is easily measured (voltage across the cell), whereas for short-circuit it has to be either calculated or measured by some other means. Boschloo et. al. [109] and Würfel et. al. [125] introduced an indirect method (see Figure 31), whilst this thesis introduces a direct method.

The diffusion lengths estimated from dynamic measurements were always found to be in the region of 10μm, in the order of the film thickness of optimised cells. We have also seen that in any case, most photons are absorbed in this length (see Figure 14), meaning that thicker films would have little impact in increasing the photocurrent.

5 Measurement and Characterisation Techniques

This section describes techniques previously developed and used in this thesis. The advantages and disadvantages are described along with the precautions that need to be taken to allow for accurate measurements. Any new techniques developed here are described in the relevant sections.

The techniques employed developed beforehand were: photovoltage charge extraction (PV charge extraction); photovoltage decay (PV decay); intensity modulated photovoltage spectroscopy (IMVS); and incident photon to current efficiency (IPCE).

5.1 Charge Extraction

The charge extraction technique was first described by Duffy et. al. [126] and then further explored by Bailes et. al. [1]. The technique is used to probe the electron density as a function of the open-circuit voltage.

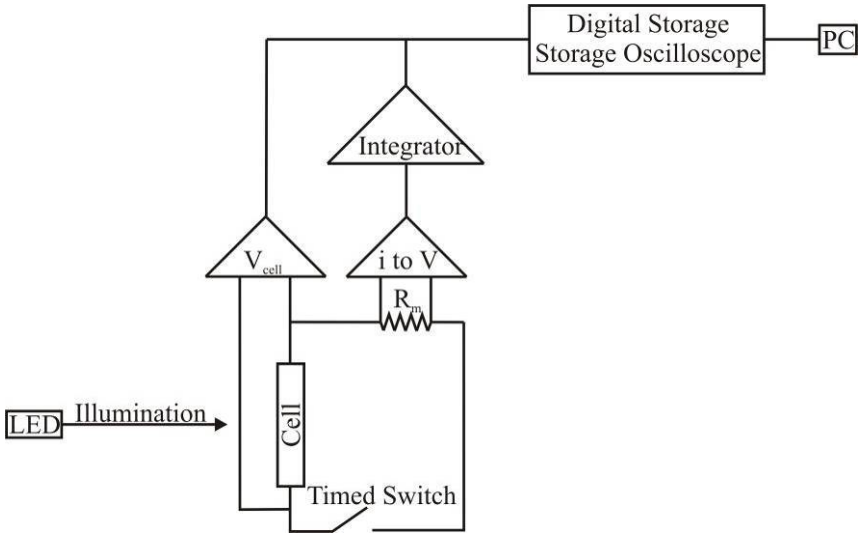

Figure 36: Schematic representation of the charge extraction apparatus.

The cell is held at open-circuit whilst illuminated. The light source is then switched off and the voltage allowed to decay for a defined time. The photovoltage decays because the electrons within the film recombine with the electrolyte species. The cell is then short-circuited and so the remaining charge flows out of the cell through a small resistor. The voltage drop across the resistor is measured and amplified and the signal integrated by an operational amplifier integrator. The voltage transient due to the decay is recorded in a digital storage oscilloscope (DSO) so to determine the voltage at which the cell is short-circuited. The integrated charge is also displayed as a transient on the DSO. The measurement is complete when the integrated

transient reaches a maximal steady value. The data is then fitted to equation 56 to obtain the characteristic temperature (T_C), and an estimate for the total trap density N_t. The total trap density is dependent on what value of E_C-$E_{F,redox}$ is assumed.

Care has to be taken to minimise leakage currents. The switch, for example, has to be of low leakage so that when the switch is at open-circuit no significant current will flow. The same is true of the voltage follower used to measure the cell voltage, which had an input impedance of $10^{12}\Omega$.

The whole active cell area was illuminated homogeneously. This was verified by using a pin diode ($1mm^2$) to map the light distribution. A variation of <5% was easily achievable over the cell area.

5.2 Open-Circuit Photovoltage Decay

The use of this technique to measure the apparent electron lifetime was demonstrated by Zaban et. al. [121]. Its main advantage is that the measurement is technically simpler than Intensity Modulated Photovoltage Spectroscopy and less time consuming.

Zaban et. al. show that the apparent lifetime can be calculated from a photovoltage decay transient using the following expression;

$$\tau_n = -\frac{k_B T}{q}\left(\frac{dV_{OC}}{dt}\right)^{-1} \qquad 64$$

The cell is held at open-circuit whilst illuminated and when the illumination is interrupted and the photovoltage transient recorded. The voltage follower (as in the charge extraction technique) must have a high input impedance. It is important to eliminate stray light, which can lead to significant errors. For this reason the system was placed in a dark box and experiments carried out in a dark room as illustrated in Figure 37.

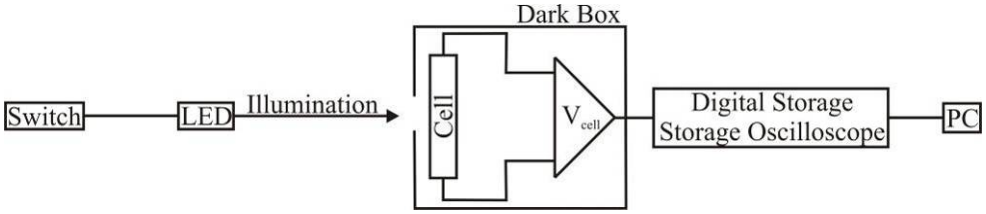

Figure 37: Schematic representation of the open-circuit photovoltage decay transient.

5.3 Intensity Modulated Photovoltage Spectroscopy

The information obtained from this technique is identical to that extracted from the Photovoltage Decay technique [121].

For IMVS measurements, the modulated light intensity can be described by;

$$I(t) = I_0\left(1 + \delta e^{i\omega t}\right) \qquad 65$$

where δ is less than 0.1 to enable linearization, maintaining the system at an essentially constant Fermi level and hence constant measured apparent electron lifetime. The Fermi level is expected to be homogeneous under open-circuit conditions if the diffusion length is sufficiently large (L_n>3d).

The IMVS response for a DSC gives a semicircle in the complex plane [127, 128], where the characteristic frequency corresponds to a 45° phase shift relative to illumination phase, i.e. the imaginary component is at its largest magnitude (but negative as it is a delay). The characteristic frequency is equivalent to the inverse of the apparent electron lifetime;

$$\omega_{\min} = 2\pi f_{\min} = \frac{1}{\tau_n} \qquad 66$$

The complex plane plot response can be understood as follows. At low frequencies, the photovoltage response can follow the temporal change in the illumination, i.e. there is no phase shift (ϕ=0) and thus the response is located on the real axis. As the modulation frequency is increased, the response begins to lag behind the driving frequency, represented as a phase shift or imaginary component. At higher frequencies, attenuation sets in until the response tends to zero with the phase shift increasing to 90°.

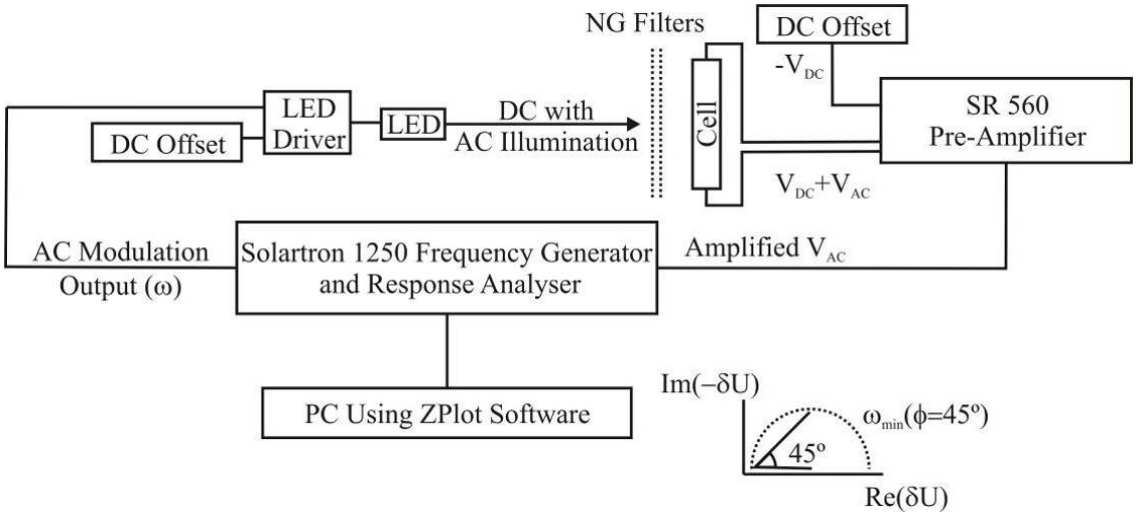

Figure 38: Schematic representation of the IMVS setup.

The IMVS response is measured by illuminating the cell with an LED driven by a frequency generator. The DC level of the cell is set by adjusting the DC level of the LED or by using neutral density light filters. The superimposed modulation is set to c.a. 5% of the LED DC level. The cell voltage is fed into a differential pre-amplifier with an input impedance of $10^8\Omega$. The DC level of the cell is offset so that only the AC component is fed into the frequency analyser to improve the signal to noise ratio. The PC displays the imaginary and real components of the voltage response as a function of the driving frequency. The characteristic frequency is then easily obtained by fitting or manual inspection.

5.4 Incident Photon to Current Conversion Efficiency

Incident photon to current conversion efficiency is a measure of how many incident photons on the cell are converted to electrons.

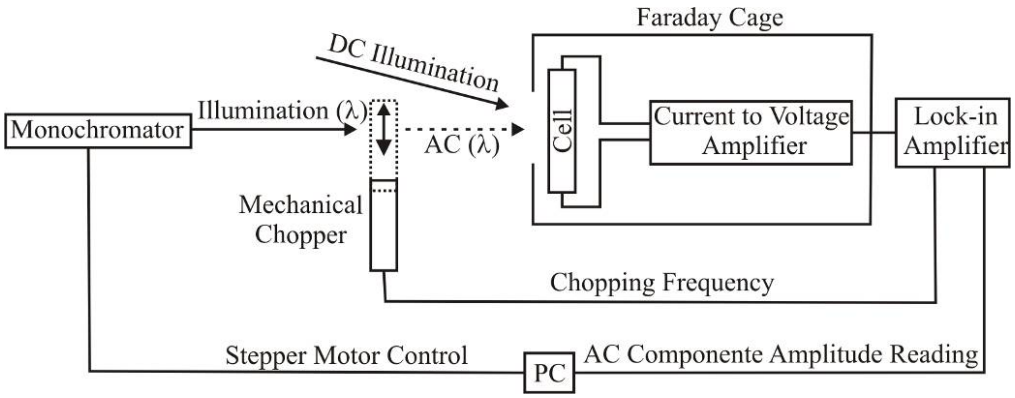

Figure 39: Schematic representation of the IPCE setup

The IPCE response is measured using chopped illumination and a lock-in amplifier. Basically, the lock-in filters out the components of the signal from the cell that do not correspond to the driving frequency. Care has to be taken that the chopping frequency is not set too high to cause attenuation of the cell response. This is achieved by lowering the chopping frequency (typically <0.3Hz), until there is no phase shift and thus negligible attenuation. Bias illumination can be used to set a desired DC current density. This allows the IPCE response to be determined as a function of light intensity/current density.

These measurements were carried out to measure the absorption coefficient of the sensitized TiO_2 film (also assuming ideal injection). The absorption coefficient can be obtained from the IPCE measurement using the following expression (assuming an exponential absorption profile, following the Beer-Lambert law);

$$
\begin{aligned}
I(x) &= I_{x=0}e^{-\alpha x} \\
I_{x=d} &= I_{x=0}(1-IPCE) = I_{x=0}e^{-\alpha d} \\
1-IPCE &= e^{-\alpha d}
\end{aligned}
\qquad 67
$$

where the thickness of the cell and the IPCE are measured.

This assumes that the injection efficiency is unity. For many systems this is not the case. It is best to compare the IPCE to the absorbance of the dye and the dye loading. For example, for the N719 dye, the dye loading can be found by desorbing the dye in 0.1M KOH and measuring the absorbance of the solution. This approach allows the injection efficiency to be estimated.

The IPCE measurement does not take into account reflection losses. However, it is straight-forward to correct for the reflections of the glass and FTO, where in this case the conducting glass had a transmission factor of c.a. 85%.

It was also used to cross compare the theoretical and experimental short-circuit currents under AM1.5 conditions because;

$$
i_{sc} = \int_{-\infty}^{\infty} I(\lambda) IPCE(\lambda) d\lambda \qquad 68
$$

This cross-comparison and the invariance of the IPCE on light intensity confirm the assumed independence of electron injection efficiency.

6 Fabrication of Dye-sensitized Nanocrystalline Solar Cell

Cell preparation involved a long sequence of steps, as shown below.

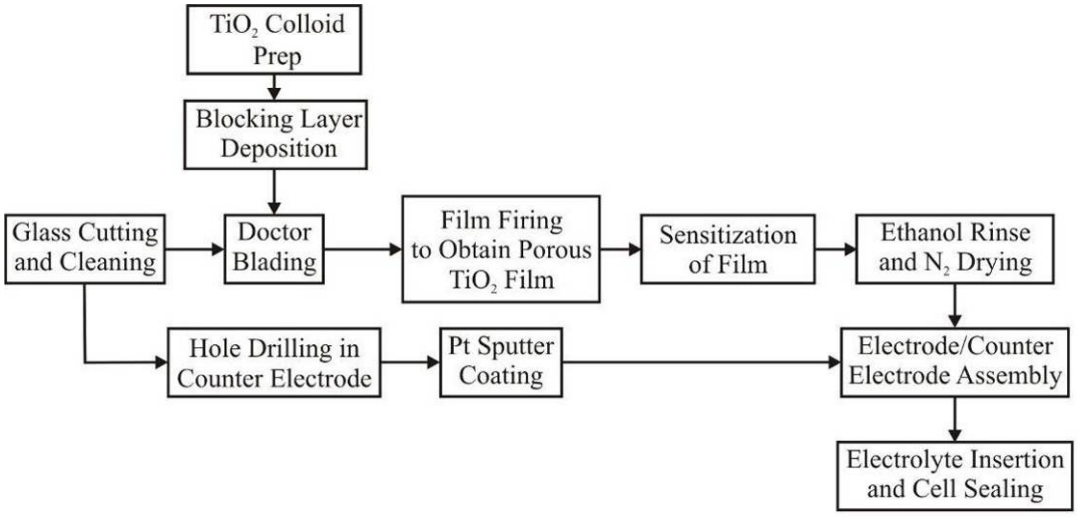

Figure 40: DSC fabrication route.

6.1 Nanocrystalline Titanium Dioxide Colloid Preparation: The Solaronix Colloid and the Acetic Acid Sol-Gel Colloid

Two types of colloid were used in the cells presented, one type using a method developed internally, and a second type purchased from Solaronix (Ti-Nanoxide HT, High Transparency Oxide with a particle diameter of 9-10nm).

The internally developed type of colloid was prepared as follows: A volume of 3.7ml of titanium (IV) isopropoxide (Aldrich 99.9%) was mixed with 1ml of 2-propanol (Aldrich anhydrous 99.9%). This solution was added drop-wise over 30 minutes into mixture of 8ml glacial acetic acid (Aldrich 100%) and 25ml of milli-Q water at 0°C. The resulting solution was then heated to 80°C and stirred for 8 hours. The milky white gel-like solution was transferred to a PTFE lined titanium autoclave and heated to 230°C via a thermostatic heating pad for 12 hours. A colloid containing nano-sized TiO_2 particles was the result of the high temperature and pressures in the autoclave. The solution was sonicated and then rotary-evaporated until a paste of desired consistency obtained, “double cream”. 0.4g of Carbowax (Riedel-de Haen, Carbowax 20000) was then added and the solution left stirring overnight. The result was a white paste of suitable consistency for doctor blading onto glass. To control the final TiO_2 film thicknesses, the viscosity of the paste was adjusted by adding de-ionised water. When in use, the colloid was kept under stirring and for storage was kept refrigerated and sealed. This was true of both types of colloids used.

6.2 Glass Cleaning

The conducting glass plates (LOF TEC15) were cleaned by sonicating for 15 minutes in Deconex (5%), propan-2-ol, ethanol and absolute ethanol, sequentially. In between sonications, the electrodes were rinsed in milli-Q water. This ensured the removal of all organic substances (grease) that tend to be found on the surface of the furnished conducting glasses.

6.3 Preparation of the Blocking Layer

The technique used was first introduced by Kavan & Grätzel [129].

Spray pyrolysis TiO_2 blocking layers were deposited from 0.2M titanium di-isopropoxide bis(acetylacetone) (Aldrich) in propan-2-ol. Clean FTO electrodes were placed on a hotplate at 450°C. The films were deposited by spraying the solution using a hand held atomiser by two short bursts every ten seconds for 3 minutes. The hotplate was surrounded on three sides by a foil-covered box to keep the temperature of the plate constant. After film deposition, the FTO electrodes were left on the hotplate for a further five minutes before being removed and allowed to cool. This technique resulted in blocking layers of the order of 100nm in thickness which suppressed the back electron transfer from the FTO to the I_3^- [38].

6.4 Nanocrystalline Titanium Dioxide Layers

The TiO_2 colloid was transferred onto the FTO by drawing the paste through a template made from c.a. 40μm thick Scotch tape. The Scotch tape templates were made with a hole punch (circular cut 5mm diameter) and carefully placed on the glass. A glass rod was drawn over the template to ensure uniformity and release of air bubbles.

A drop of colloid was then placed near the unmasked area and spread using the glass rod. This was repeated until the colloid layer became uniform but before the paste began to dry. This method resulted in film thicknesses of c.a. 5μm, having an area of 0.196cm^2. Films were left to dry and rest at normal room conditions before firing. Film thicknesses were measured using a Dektak 6M profilometer.

The electrodes (TCO and colloid film) were then fired in stream of air at 450°C for 25 minutes. The colloid film would initially turn black due to thermal decomposition of the organics contained in the paste. This colour would then fade, resulting in a transparent nanocrystalline mesoporous anatase TiO_2 film.

6.5 Counter Electrode

Single holes of c.a. 0.5mm in diameter in the counter electrode were made using a dentist's diamond tipped drill. This drilling was carried out from the conducting side under water immersion. Drilling was done from the conducting side because of the tendency for the glass to slightly shatter as the drill exited the glass. Water was used to help glass dust disperse away and keep the drill bit cool. The glass was then cleaned as described above.

Platinum was deposited on the conducting side of the glass by sputter-coating. Only a thin semi-transparent film is required to ensure facile regeneration of the redox couple. The performance of the counter electrodes were periodically tested. This was achieved by fabricating thin layer cells consisting of two adjoined counter electrodes, filled with electrolyte, and then measuring the current voltage characteristic of the thin cells (example shown in Figure 41).

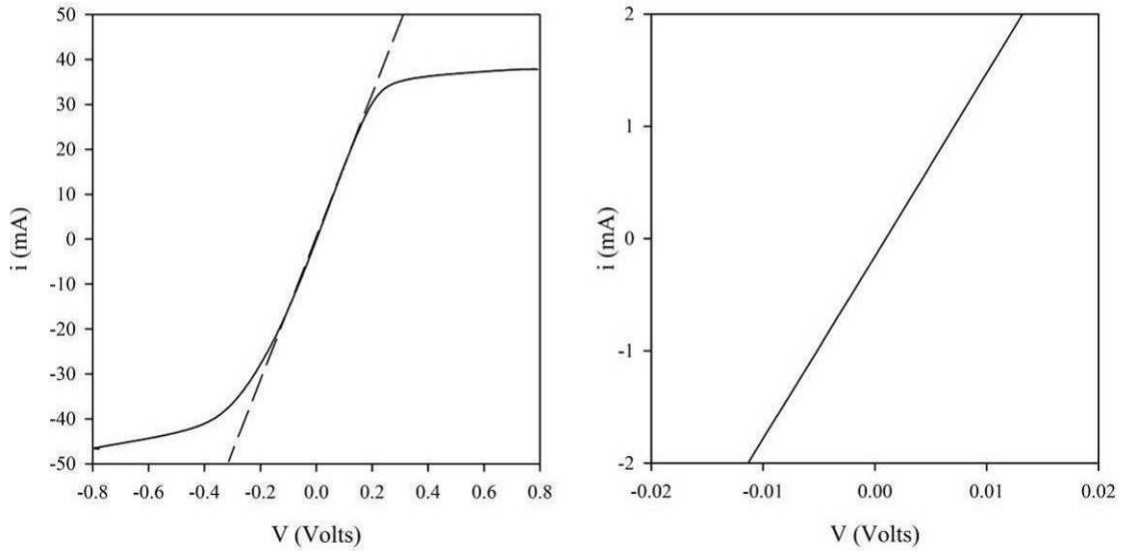

Figure 41: Current Voltage curve of a typical CE/CE setup (left is full scale, right is magnified view) to test the performance of the counter electrode. At 1 sun the cells typically produced 1 to 2mA (5 to 10mAcm^{-2}). At this current density, the overvoltage at the counter electrodes is negligible, c.a. 10mV. This setup also allows one to estimate the intrinsic resistance of the cell using Ohms Law, V=IR. For this cell it is c.a. 5Ω.

The resultant electrodes had a transmission coefficient of c.a. 65% in the visible, and were, accordingly, suitable for counter electrode illumination. The electrodes were fired for 5 minutes at 200°C before and after sputtering to remove organics from the surface. If this were not done, the Pt films tended to detach from the FTO when in contact with the electrolyte solution.

6.6 Electrolyte

The electrolyte used in this work was based on the I^-/I_3^- redox couple. The following were dissolved in acetonitrile to make up the redox electrolyte:

0.05M iodine;

0.1M lithium iodide;

0.5M tertiary butyl pyridine.

The tertiary butyl pyridine is a standard additive that has been found empirically to improve cell performance.

6.7 Dye Solution and Sensitization

The N719 dye utilised is available commercially from Solaronix. Again, it has been found empirically that a 0.3mM solution in 1:1 absolute ethanol/acetonitrile results in good sensitization performance.

After firing, the electrodes were cooled or heated to c.a. 80°C on a hotplate and transferred into the dye solution in a staining jar and left sealed in nitrogen atmosphere in the dark overnight. Upon dyeing, the electrodes were rinsed thoroughly in acetonitrile to remove excess unattached dye. They were then dried in nitrogen and stored in acetonitrile in the dark.

6.8 Final Assembly

The electrodes were joined together using 25μm thick adhesive polymer gasket (available via Solaronix), having the same shape as the templated Scotch tape. A hypodermic needle (~0.5mm diameter needle tip) was then inserted in the hole of the counter electrode and filled with electrolyte. The cells were then placed in a vacuum chamber and pumped down until the electrolyte began to bubble. At this point air was rapidly allowed back into the chamber, pushing the electrolyte into the space between the working and counter electrodes, filling the cell. The filling holes were sealed using the same polymer adhesive and thin glass square plates.

6.9 Cell Enhancements

In order to reduce the RC time constant when performing some photocurrent transients, the contact resistance of the cell was minimised by evaporating gold up to the edges of the working areas of the electrode and counter electrode. This was performed after the working and counter electrodes had

been through the normal preparation phases. Circular 7 mm diameter brass masks were used to mask the working area of the cell. For better adherence of gold to the surface, a buffer layer of chromium was evaporated first to eventually produce a scratch resistant metal surface.

As the capacitance scales linearly with TiO_2/TCO interface area, the active cell area was made as small as possible. After preliminary experiments, an active area of 0.196cm^2 was used.

It was found that the gold contacts reduced the series resistance from 20Ω to 5Ω. This was verified by impedance spectroscopy at short-circuit. The reduced series resistance was also evident from higher fill-factors of the AM1.5 iV curves (see Figure 65).

7 Characterisation of a Dye-sensitized Nanocrystalline Solar Cell Using a Secondary Sensing Electrode

In order to understand the transport and transfer of electrons in a DSC, cells were fabricated where a titanium contact was used to probe the quasi-Fermi level (QFL). Measurements with these cells allowed comparison of experimental and predicted profiles of the QFL under different working conditions. The idea of incorporating a secondary electrode to measure the QFL was first suggested by Würfel et. al. [130, 131] and was then developed at the University of Bath by the author [2].

The internal potential (U_{SE}) was measured as a function of applied bias (i.e. along the positive power quadrant of the iV curve) and fitted using solutions to the continuum equation [2]. The values obtained from the fitting are discussed. The effects of trapping were explored by measuring how the trapped charge within the cell varied with applied bias and internal potential. The temperature coefficients of the open-circuit voltage V_{OC} and the V_{SE} were also characterised [132] and shown to be compatible with conduction band diffusion and recombination of electrons. The use of an internal electrode also proved interesting with regards to characterising the apparent electron lifetime via photovoltage decay. The PV decay was shown to occur more rapidly without a blocking layer and it was demonstrated that under these conditions, the QFL decay is spatially inhomogeneous.

7.1 Incorporation of a Secondary Sensing Electrode

To prevent short-circuiting between the added electrode and the blocking/FTO substrate, a strip of the conducting FTO substrate was etched. Kapton® polyimide tape was used for masking. To etch the unmasked area, zinc granules were placed on it and then a few drops of concentrated HCl were added for only a few seconds to dissolve the FTO. The etching was stopped by rinsing the electrode with distilled water to prevent the etching from continuing beneath the masking tape. The glass was then cleaned and the blocking layer added as described previously.

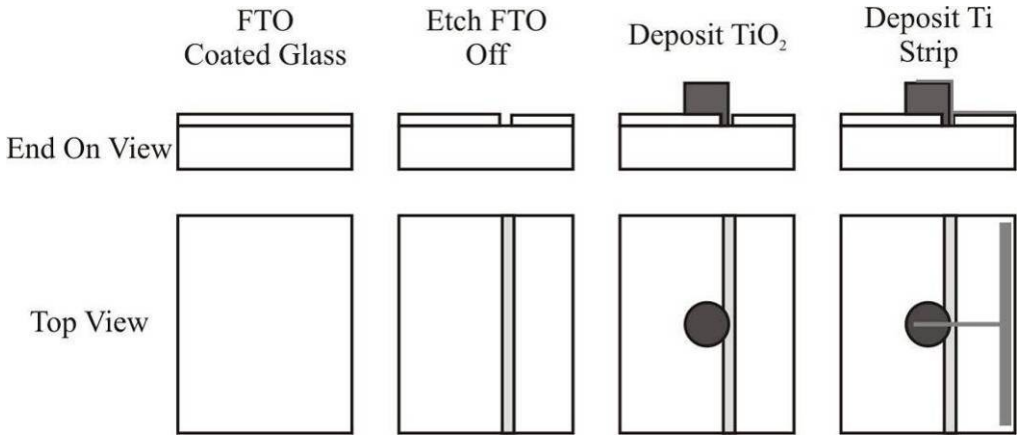

Figure 42: Schematic representation of how the Ti sensing electrode was deposited

The porous TiO_2 film was deposited onto the glass leaving about 1mm overlap onto the non-conducting the etched region of the substrate. This geometry ensured that the internal secondary electrode did not come into contact with the active area of the working electrode. The 1mm wide, c.a. 100nm thick titanium strip was deposited by thermal vacuum evaporation of 99% titanium wire.

To prevent a secondary route for back reaction of the electrons in the TiO_2 with the electrolyte species, the electrode was passivated by growing a TiO_2 layer on the titanium surface. Two methods were used to passivate the secondary sensing electrode (SE). Initially after depositing the Ti film on the TiO_2 electrodes were heated in air at 450^{o}C to grow an oxide layer [133]. However it was later found that by evaporating at moderate vacuum levels (10^{-4} bar) rather than high (10^{-6} bar), the remaining oxygen inside the vacuum chamber was enough to form a sufficiently thick oxide layer on the SE to passivate it. The oxidation of the titanium was manifest in-situ by the decrease of the vacuum pressure during the deposition. Following inclusion of the SE, the cells were assembled in the usual manner.

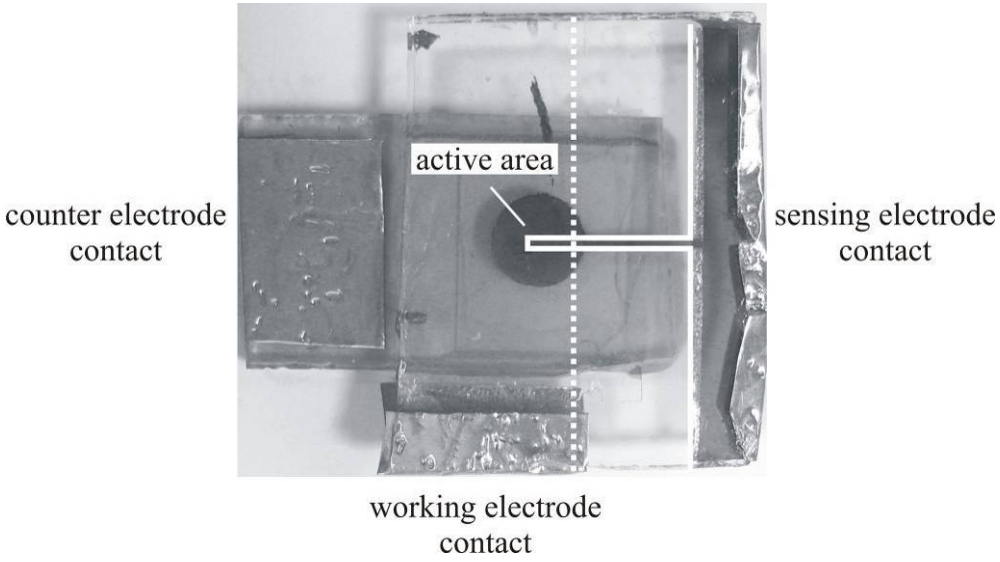

Figure 43 Photograph of a typical cell employing the secondary sensing electrode. The broken line represents the separation between the conducting and non-conducting areas of the glass substrate. The solid line outlines the area onto which the Ti was evaporated onto.

7.2 Secondary Sensing Electrode Optimisation

This section highlights the necessary precautions that are required to obtain reliable results from the SE. The three precautions were: (i) a minimum thickness of the Ti was required; (ii) the Ti surface of the electrode had to be passivated to prevent an additional route for recombination, and (iii) the un-contacted overhanging active area had to be minimised.

The SEM images (see Figure 44) suggested that the Ti penetrated the TiO_2 film to a depth of c.a. 0.5μm. Attempts were made to look at the region where the Ti strip transitions from the TiO_2 onto the glass substrate but, the limited depth of field of the SEM technique coupled with the geometry of the electrode, made it impossible to inspect this transition.

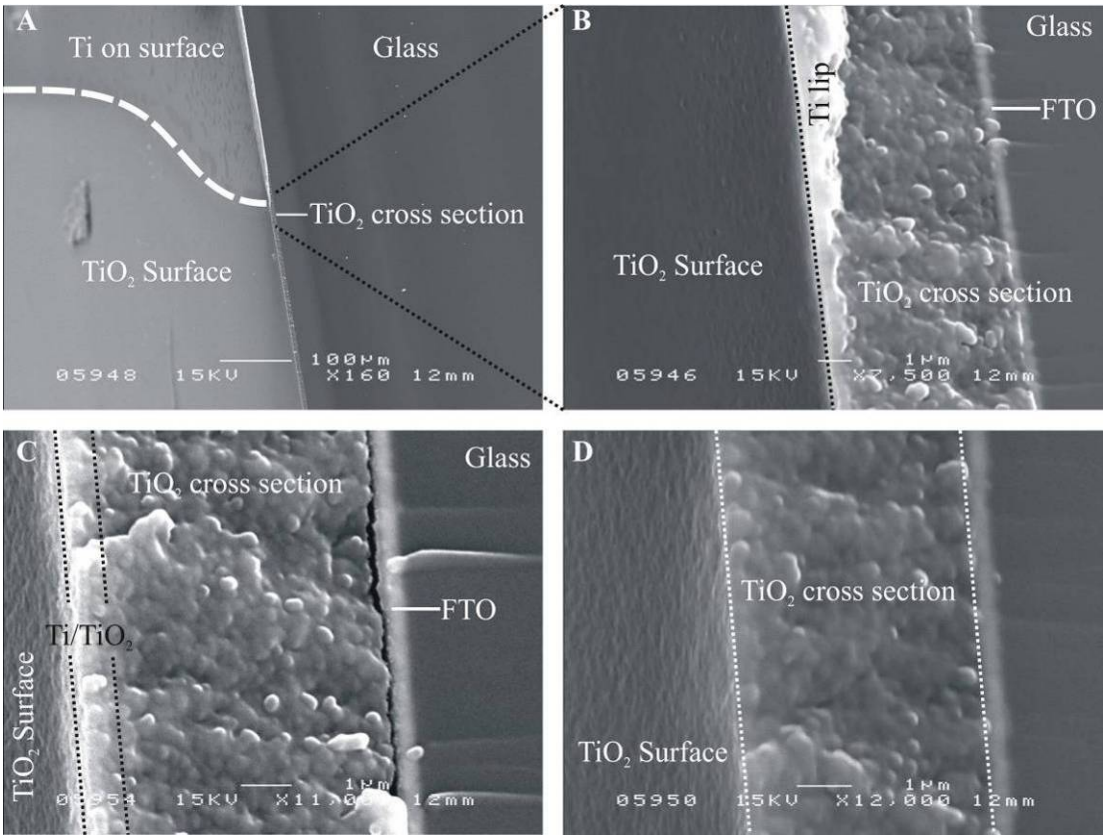

Figure 44 Oblique cross-section SEM images of the deposited Ti on the TiO_2. Sample was broken in half to expose the cross-section of TiO_2 and Ti. For all images from left to right: Surface layer, top edge/Ti, sectioned TiO_2, sectioned FTO/glass. Image A is a low magnification image contrasting the areas where the Ti was deposited and not deposited. At first, the bright strip in the cross-section of the TiO_2 would suggest that the Ti penetrated the TiO_2 structure to a significant degree. However, looking more closely with image B the bright area appears to be an overhanging film of Ti. This could occur as the electrodes are broken in half, stretching and tearing the Ti film. Moving away from the overhanging lip one can observe in image C a c.a. 0.5μm bright layer. With an image taken away from the zone where the Ti was deposited as in image D, the upper layer of the TiO_2 is not as bright. These images suggest that the level of penetration of the TiO_2 to be about 0.5μm.

The minimum thickness of Ti required to obtain reliable results was c.a. 100nm. This thickness was necessary to guarantee an unbroken structure of the Ti electrode from within the cell to the outside circuit, where it has to step down c.a. 5μm onto the substrate. The thickness quoted here were not measured on the TiO_2 layer but on the glass substrate adjacent to the TiO_2. Profiles along the TiO_2 intersecting the region where the Ti was deposited did not show any change in thickness, suggesting the Ti penetrated the TiO_2 film.

If the internal electrode is not passivated not only is the potential measured at the electrode unrepresentative of the nature of the QFL of a normal cell, but it will also have a negative effect on iV characteristic, as illustrated in Figure 45.

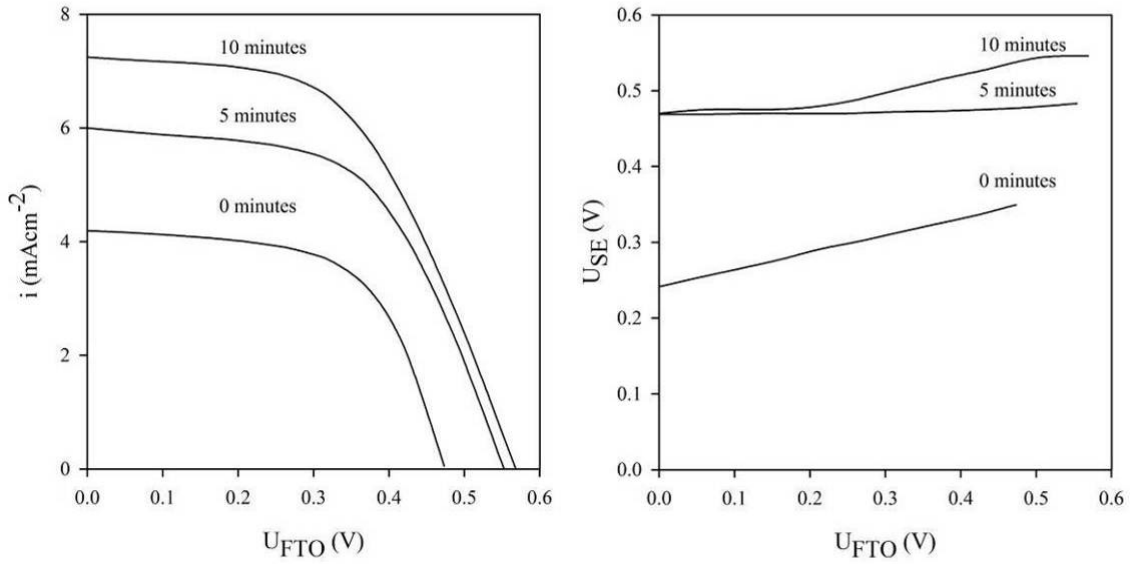

Figure 45 AM1.5 i vs U_{FTO} (Left) and U_{SE} vs U_{FTO} (Right) for cells with different thermal oxidation times to passivate the SE. Voltages were measured with respect to the counter electrode. The electrolyte did not include tertiary butyl pyridine, and hence the low open-circuit voltages. No blocking layer was included in these preliminary measurements.

Figure 45 also illustrates how the internal photovoltage measured by the SE varied according to the applied bias at the working electrode (FTO). The unpassivated electrode cell had a lower voltage because electrons recombine with the electrolyte species at a greater rate at the surface of the titanium electrode. This suggests that inside the TiO_2 layer there is bi-directional electron flow towards the collecting substrate and secondary electrodes, impacting on the short-circuit current.

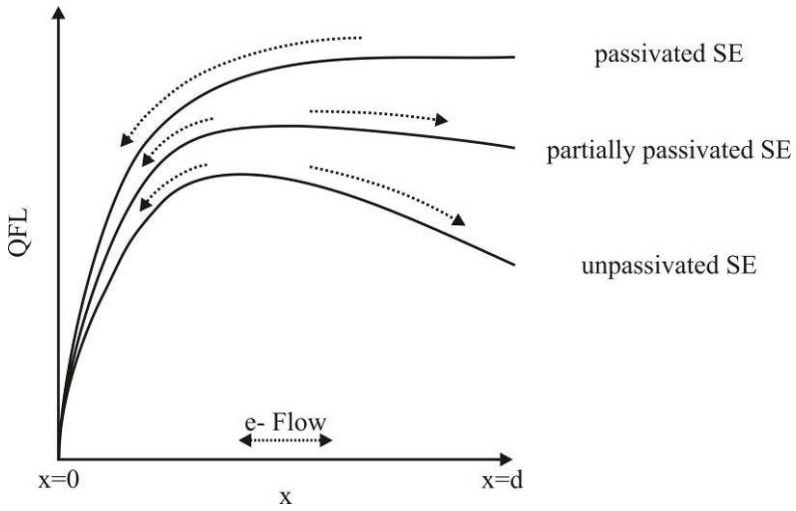

Figure 46: Rendition of the possible QFL distribution at short-circuit within the TiO_2 due to recombination at x=d where sensing SE is present.

The other aspect that interferes with the measuring of the internal voltage is by how much the TiO_2 film overlaps the non-conducting etched area. As the etched region non-conductive, locally the cell appears to be at open-circuit, i.e. the electrons would have to move laterally towards the area where they can be collected. The problem is illustrated in Figure 47.

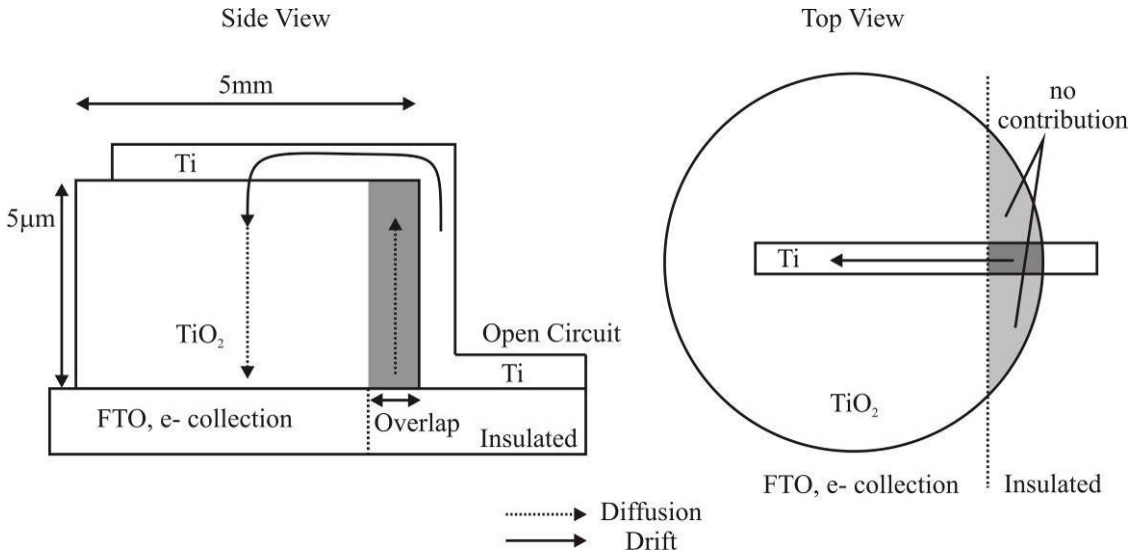

Figure 47: Hypothetical IR drop occurring within the SE. Electrons generated in the volume (dark grey) of TiO_2 covered by the Ti film but where the FTO was etched will be collected and travel around within the metallic electrode (which has a resistance associated to it) and re-injected into the TiO_2 to diffuse to the FTO. The insulated areas (lighter grey) not covered by the Ti film are isolated from the rest of the film. The reason for this is that the lateral distance (~mm) to either the Ti film or the underlying FTO will be greater than the diffusion length (~μm) of the electrons.

An IR drop could arise from the electrons travelling through the Ti film, and its value be a function of the current through the Ti film and the resistance of the same film. The amount of charge would be, in principle, be linearly

proportional to the volume of TiO_2 in contact with the Ti but not with the FTO, this volume scaling linearly with the length of the overlap.

Figure 48 illustrates the three geometries that were used to test how the voltages measured by the secondary electrode varied. The overlapping used was 0mm, 1mm and 2.5mm. The 0mm overlap was an attempt to minimise the overlap to a marginal amount. The 1mm overlap was the minimum that could be repeatedly achieved by the method of fabrication. The 2.5mm overlap gave a 1:1 ratio of the overlapping area with the area in direct contact with the FTO substrate.

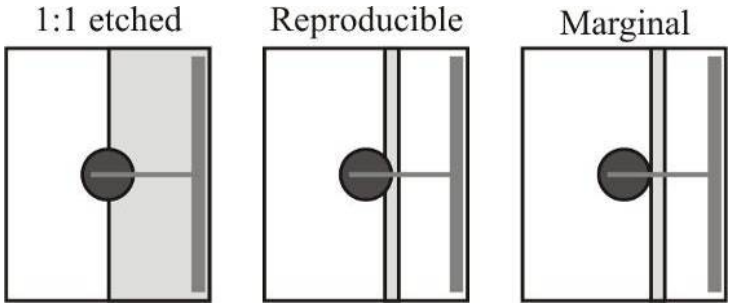

Figure 48: Three geometries used to investigate the effect of overlap of the TiO_2 on a non-conducting substrate (etched).

The attempts at a minimal overlap (0mm) resulted in a low voltage at short-circuit, and thus appeared to be short-circuiting with the FTO substrate. Under open-circuit conditions the voltages measured at the FTO and SE varied by less than 3%. The variation could be attributed to variations in the illumination distribution and the accuracy of the DVM used.

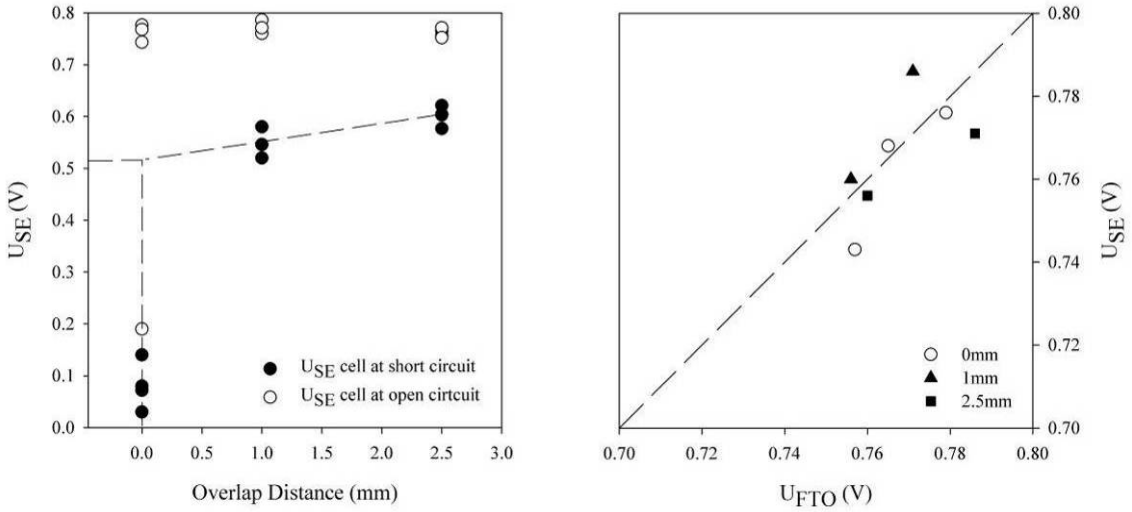

Figure 49: Left: Values of the internal voltage measured by the SE (passivated) at short and open-circuit as a function of TiO_2 overlap with etched region. The voltage measured for the SE at short-circuit increased as the overlap increased at 35mV per mm (ignoring 0mm overlap data). Right: Comparison of the measured voltage at the SE and FTO under open-circuit conditions.

The problem due to the overlap is evident in Figure 49 where the voltages measured for the SE under short-circuit conditions increased with greater overlapping. Because the SE is thin and partially oxidised, the resistance associated to it could be large, thus giving rise to the IR drop across it. If one extrapolates to 0mm overlap then, according to these results, the added potential measured at the SE is c.a. 35mV greater than the true vale c.a. 500mV.

Highlighted were the precautions required when a secondary Ti electrode is incorporated into the TiO_2 film of a DSC. There is the physical contacting between the film to the outside requiring a minimum film thickness. The passivation of the electrode was also shown to be crucial yet simple to achieve. An offset to the voltages measured by the electrode could also be present due to currents flowing internally through the Ti film.

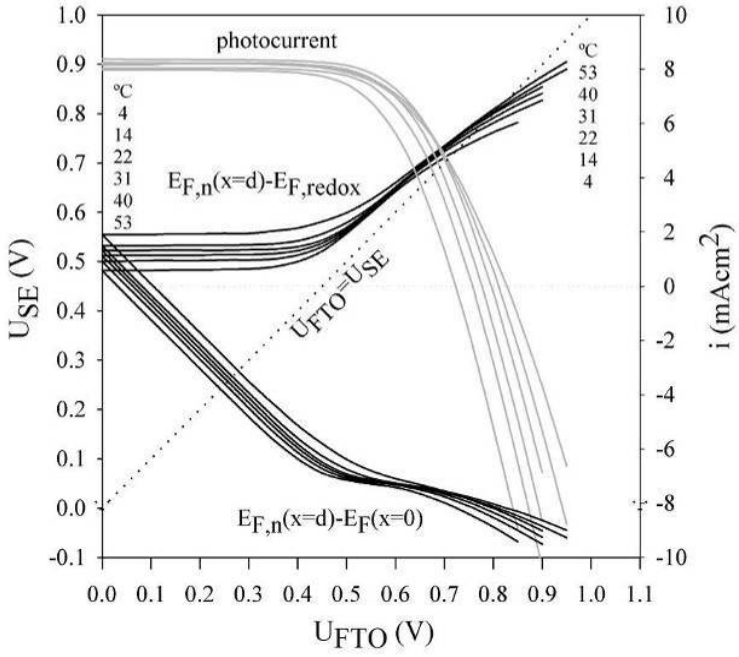

Figure 50 iU_{FTO} and $U_{FTO}U_{SE}$ characteristics of a standard cell with an optimised SE, for various temperatures.

Figure 50 illustrates the corresponding temperature dependence of the complete iU_{FTO} and $U_{FTO}U_{SE}$ curves of these cells. In the following sections, the added information provided by measuring the internal QFL by use of the SE will be put into practice to compare theoretical predictions to experimental data.

7.3 An Example of the Importance of the Blocking Layer

With the optimised incorporation of the secondary sensing electrode, the photovoltage decays present some interesting results. The decay profiles of the FTO and SE for a cell with a blocking layer were, as expected, identical (see Figure 51). This is the case if the QFL decay throughout the TiO_2 layer is homogeneous and the electrodes contacting to the TiO_2 do not interfere with the recombination rates. This has to be true for the FTO and SE electrodes.

For cells with no blocking layer, the QFL decay was found to be spatially inhomogeneous, as recombination via the FTO is predominant. This has serious consequences when inferring electron lifetimes by measuring the voltage at the FTO. The transients demonstrate the importance of a blocking layer in the characterisation of a DSC. Results obtained for cells without a blocking layer are thus likely to be distorted by back reaction of electrons via the FTO substrate (see Figure 5).

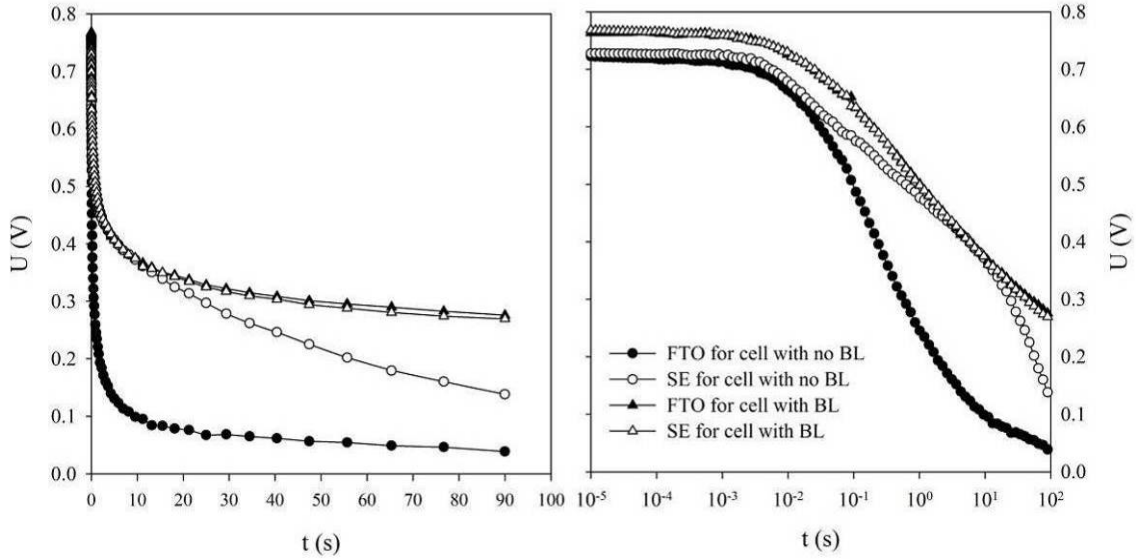

Figure 51 Photovoltage decays of cells with an optimised secondary electrode. The influence of a blocking layer on the FTO is evident. The same profiles are shown on two temporal scales, linear and logarithmic.

7.4 Ideality of the Measured Open-Circuit Voltage

Since the photovoltage decays of optimised cells with blocking layers showed matching transients for the FTO and SE, the same would be expected of lifetimes obtained from IMVS measurements. This was indeed the case. For each voltage, similar lifetimes were obtained for the two contacts. However, these lifetimes were not exactly identical to those obtained via PV decays. The lifetimes measured by IMVS (see Figure 52) separated from those measured via photovoltage decay at intermediate potentials (0.35 to 0.6V). This was also the regime where the photo-stationary open-circuit photovoltages also separated (see Figure 53).

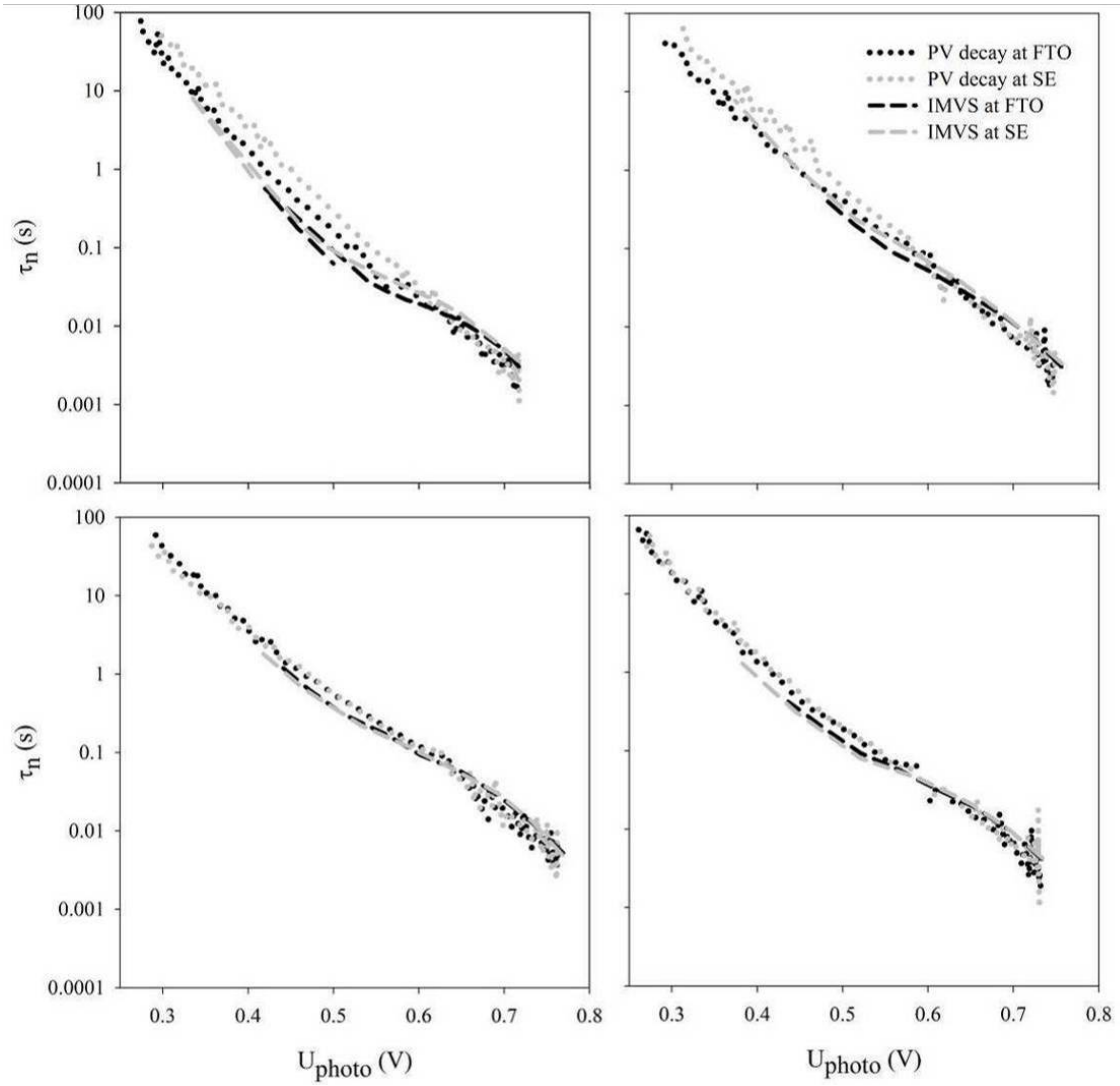

Figure 52 Apparent electron lifetimes of four typical cells employing a secondary electrode. Lifetimes were measured by IMVS and PV decay.

It is unclear if the differences seen in the lifetimes was an artefact created by fitting the IMVS data or whether there is a real difference between the two methods, which in principle should yield the same results.

If the transfer of electrons to the electrolyte occurs via the conduction band, then the value of the slope of the open-circuit voltage intensity dependence should be 59mV/decade at room temperature. However, for the particular cell shown in Figure 53, the gradient was 82mV/decade.

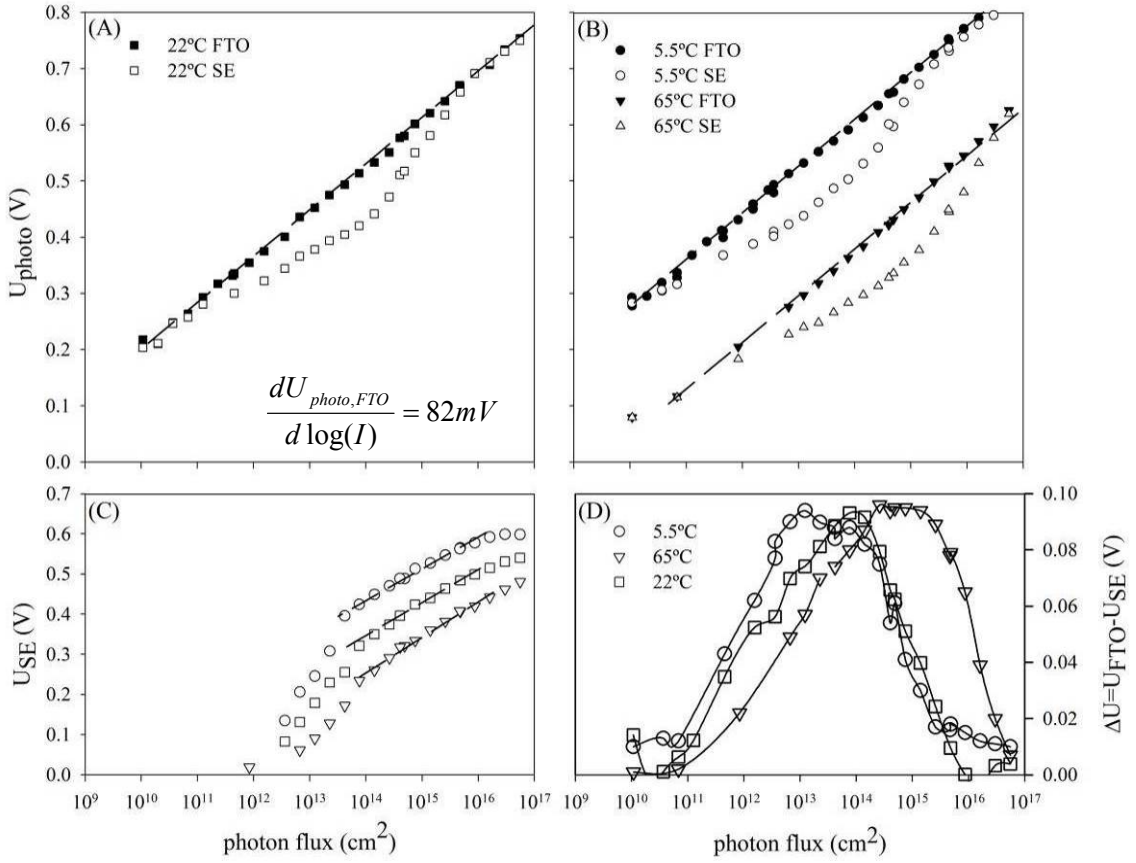

Figure 53 (A) Photovoltage versus illumination (532nm) for the FTO and SE at 22°C. (B) Photovoltage versus illumination for lower and higher temperatures, 5.5C and 65C respectively. (C) Voltage measured at the SE when the FTO is short-circuited (i.e. cell is short-circuited). (D) Difference in measured photovoltage between the FTO and SE versus illumination at the three different temperatures.

The voltage range where the IMVS lifetimes are lower than the PV lifetimes (0.35 to 0.6V) is also the range in which the intensity dependence of the photovoltage measured at the two electrodes splits (10^{11}~10^{16} photons cm^2s^{-1}).

The peak in the difference between the FTO and SE shifted to higher illumination intensities with increased temperature, and at low intensities, the voltages measured at both electrodes were again equivalent. At the highest temperature of 65 ° C, the FTO also deviates from the logarithmic relationship. The c.a. 100mV difference between the electrodes at 10^{15} photons/cm^2 implies a significant electron concentration gradient that would draw electrons from the FTO towards the SE.

Ideally, the gradient of the photovoltage should be dependent on temperature (see equation 32). However, the profiles at three separate temperatures are parallel for reasons that are not clear.

To further elucidate on the performance of the SE, PV decay transients were measured as a function of temperature. As the temperature was increased the difference in the decay transients between the FTO and SE also increased. The transients at the FTO always decayed more rapidly than the transient of the SE, suggesting the kinetics for back reaction at the FTO are more sensitive to temperature. This could be caused by the imperfect passivation of the FTO with a BL. These temperature effects shown here are further explored and the results discussed sections 7.8 and 8.2.

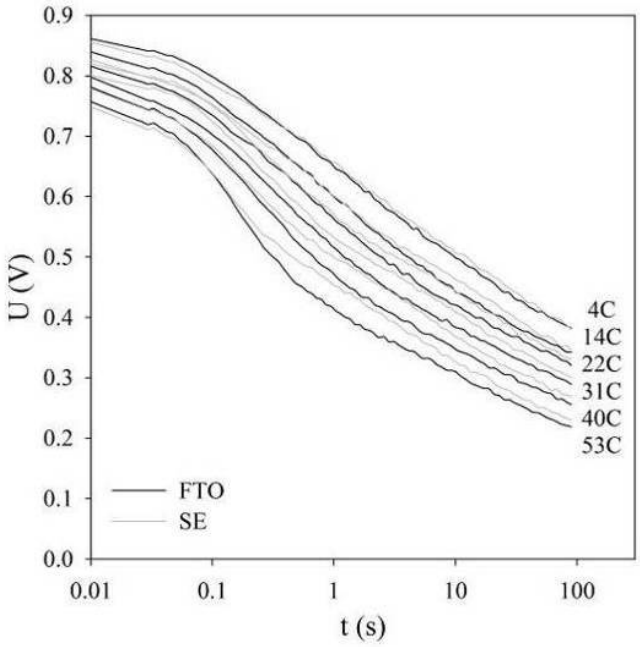

Figure 54 Photovoltage decays for a cell with the SE. Decays were recorded at various temperatures. At increased temperatures, the decay transients are more rapid but there is also a splitting between the voltage measured at the two electrodes, with the more rapid decay transients measured for the FTO.

The PV decay transients suggest the passivation of the SE was always better than that at FTO, i.e. the recombination kinetics at the SE are lower than those at the FTO. However, the photovoltage dependence on illumination (see Figure 53) appears to indicate the contrary. The reasons for this contradiction remain unclear. Nonetheless, at high illumination intensities and low temperatures the splitting of the voltages measured at the two contacts is not observed.

7.5 Direct Measurement and Modelling of the Quasi-Fermi Level Using a Titanium Secondary Electrode

Having shown how the QFL inside the TiO_2 under certain conditions can be probed reliably, the characteristics of the QFL were modelled and compared to experiment. In section 4.6 the iV curve was formulated by solving the continuity equation for diffusive electron flow. The solutions were presented as a function of voltage at x=0. The insertion of the secondary electrode allows the voltage to be probed at x=d (d being the TiO_2 thickness). Therefore, one can test the diffusive model for electron transport by measuring the relationship between applied voltage, internal voltage and photocurrent.

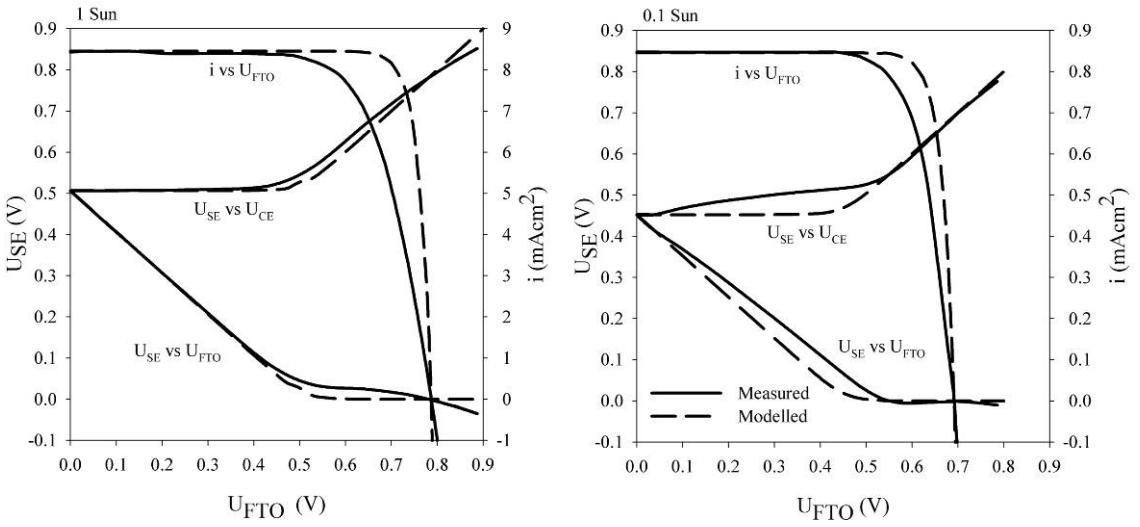

Figure 55 Experimental (full lines) i vs U_{FTO}, U_{SE} vs U_{CE} and U_{FTO} vs U_{SE} under (a) 1 sun and (b) 0.1 sun illumination intensities with the fitted curves superimposed (broken lines).

In Figure 55 are the results of a SE cell where the internal potential was measured as a function of applied bias. The cell was illuminated with 532nm LED at two different intensities to mimic the conditions under 1 and 0.1 sun. The fitting of the curves resulted in reasonable superposition of the measured and modelled data. The discrepancy in the fill-factors is a result of the series resistance of the cells. Cells that were optimised to have a lower geometric series resistance had clearly improved fill-factors. Consequently, at lower current densities, i.e. at 0.1 sun, the fill-factor is noticeably improved. No over-potential at the counter electrode was observed as the measured potential differences between the FTO, SE and CE were all complimentary, i.e.;

$$\left(U_{SE} - U_{CE}\right) = \left(U_{SE} - U_{FTO}\right) + U_{app} \qquad 69$$

The curves were fitted to the experimental data in three stages, with analogies to the terms in the continuity equation (equation 38). Firstly, the calculated

short-circuit currents were checked to match the measured ones by tweaking the absorption coefficient and light intensity, as exact values for these are difficult to measure. Also defining the generation rate of electrons and hence the short-circuit current density is the TiO_2 film thickness, but this was well characterised and thus not changed to suit. This comparison between calculated and measured short-circuit current density only holds true when the TiO_2 is thickness is c.a. three times less than that of the electron diffusion length. These physical parameters correspond to the first term in the continuity equation. Secondly, the diffusion coefficient was determined by matching the modelled and measured voltage at x=d when the cell was at short-circuit. This corresponds to the second term in the continuity equation. Thirdly, the electron lifetime was established by obtaining the correct value that would match the measured open-circuit voltage, i.e. when the dark current (recombination current) matched the photocurrent. This in turn corresponds to the last term in the continuity equation. Thus, to a certain extent, the diffusion coefficient and electron lifetimes were determined independently.

Comparing the internal potential profile as a function of applied bias for the two different intensities raises an interesting contrast. At low biases, the high intensity data better matched the modelled data, while when the maximum power point was approached and surpassed the data at lower intensities was in better agreement.

Table 7.5-1 – Fitting parameters used in Figure 55

Parameter	1 Sun	0.1 Sun	Description
			estimated a priori
E_C-$E_{F,redox}$	0.95 eV	0.95 eV	energy difference between conduction band and redox potential
N_C	10^{21} cm^{-3}	10^{21} cm^{-3}	conduction band density of states
			resultant from fitting
D_0	0.35 cm^{2}s^{-1}	0.29 cm^{2}s^{-1}	CB electron diffusion coefficient
τ_0	16.5 ms	4 ms	CB electron lifetime
L_0	760μm	350μm	CB electron diffusion length
d	5 μm	5 μm	measured values TiO_2 thickness
I_0	8.35x10^{16} cm^{-2}s^{-1}	8.35x10^{15} cm^{-2}s^{-1}	incident photon flux
α	2000 cm^{-1}	2000 cm^{-1}	photon absorption coefficient at 532nm

These measurements suggest an electron diffusion coefficient of hundreds of microns, greater than has been estimated beforehand by time dependent dynamic measurements (see section 4.8). As discussed beforehand the interpretations suffered from being analysed as a function of light intensity and not as a function of the position of the QFL.

The position of the conduction band edge is not a defined value as it is influenced by adsorbing species onto the TiO_2 and changing the surface dipole

moment (e.g. adsorption of lithium, protons or tertiary butyl pyridine). In fact, the band edge could shift as the quasi-Fermi level is raised due to charge accumulation within the TiO_2. The choice of conduction band density of states is to some extent also arbitrary.

Table 7.5-2

diffusion coefficient from fitting

E_C-$E_{F,redox}$ \ N_C (cm^{-3})	10^{20}	10^{21}	10^{22}
0.95-0.059 eV	$3.5x10^{-1}$	$3.5x10^{-2}$	$3.5x10^{-3}$
0.95 eV	3.5	$3.5x10^{-1}$	$3.5x10^{-2}$
0.95+0.059 eV	35	3.5	$3.5x10^{-1}$

D_0 (cm^2s^{-1})

electron lifetimes from fitting

E_C-$E_{F,redox}$ \ N_C (cm^{-3})	10^{20}	10^{21}	10^{22}
0.95-0.059 eV	16.5	165	1650
0.95 eV	1.65	16.5	165
0.95+0.059 eV	0.165	1.65	16.5

τ_0 (ms)

Table 7.5-2 demonstrates how varying E_C-$E_{F,redox}$ or N_C affected the inferred D_0 and τ_0. If E_C-$E_{F,redox}$ is increased by 59meV then to maintain the same D_0 and τ_0, N_C must be increased by an order of magnitude. If N_C is increased by an order of magnitude, D_0 must be lowered and τ_0 increased by an order of magnitude whilst maintaining their product and, hence, L_n constant. Similarly, if E_C-$E_{F,redox}$ is increased by 59meV, D_0 must increase by an order of magnitude and vice versa for τ_0. The values of D_0 and τ_0 are maintained if both Nc and E_C-$E_{F,redox}$ scale together, (left to right diagonal in Table 7.5-2). Deviation from this diagonal in one direction results in un-physically large diffusion coefficients or in the other direction un-physically large lifetimes.

It is important to remind the reader that the electron diffusion coefficients and lifetimes are for electrons in the conduction band, and are not the apparent values obtained from the dynamic methods such as IMPS and IMVS/PV decay. The quasi-static approximation detailed in section 4.8 describes how the diffusion coefficients and electron lifetimes are correlated due to sub-band gap trapping. Therefore, one can use data from IMVS/PV decay and IMPS measurements to set upper and lower limits for electron lifetimes and diffusion coefficients respectively. This is further discussed in section 7.6.

One might expect the maximum value of the diffusion coefficient to be that of bulk anatase TiO_2. From the Hall mobility measurements of Forro et. al [134], the electron diffusion coefficient in single crystal anatase can be calculated to be $D_0 \approx 0.4 cm^2 s^{-1}$. Lower diffusion coefficients might be a consequence of added electron scattering due to the porous TiO_2 structure. Monte Carlo modelling by Cass et. al. [135, 136] of electron transport in an array of interconnected nanocrystals, predicts that geometrical constraints associated to the narrow necks between particles reduces the electron diffusion coefficient.

The electron lifetimes can never be longer than the apparent electron lifetimes observed in IMVS and photovoltage decay techniques. Therefore, an upper limit on the electron lifetimes can be set to 1ms (see Figure 52 and Figure 56). However, lifetimes resultant from the fitting of the QFL are longer. In addition, the discrepancy between the inferred lifetimes at 1 sun and 0.1 sun intensities, is probably a consequence of the non-ideal nature of the cells. Ideal characteristics would lead to an increase in photovoltage by 59meV per decade of illumination. This was not the case for these cells in question (see Figure 53). This is most probably due to additional states, located on the surface of the TiO_2 particles that are involved in the transfer of electrons to I_3^-. This has important consequences on the modelling because ideal behaviour was always assumed. However, if the diffusion length remains large (L_n>3d), the value of the lifetime does not change the QFL profile at short-circuit (see Figure 23) and thus, does not affect the value of the inferred diffusion coefficient.

7.6 Electron Lifetime Estimation by Measuring the Apparent Electron Lifetime

A minimum value for the conduction band electron lifetime (τ_0) can be obtained by measuring the minimum apparent electron lifetimes (τ_n). The quasi-static approximation allows the apparent electron lifetimes to be related to the conduction band electron lifetime (see equation 62). To compare theory with experiment requires the trap distribution to be characterised (the characteristic temperature T_C, and the trap density N_t). There is, as always, flexibility in the use of other parameters and thus far, plausible values for conduction band edge position and density of states have already been explored. The value of T_C can be measured either by the charge extraction technique or in principle by the apparent lifetime techniques (PV decay and IMVS).

Obtaining T_C via PV charge extraction is, in principle, straightforward as it is an independent value, i.e. its value is unaffected by the assumption of other physical values.

T_C can also be determined from how the apparent lifetime varies according to the Fermi level (or measured open circuit voltage) [121].

$$T_C = \frac{d\log(\tau_n)}{dqU_{photo}} \qquad 70$$

However, this is only true if the cell behaves ideally which is not true for most cases. This leaves one parameter, the total trap density N_t (integral of the trap density of states function between $E_{F,redox}$ and E_C). Because of the way N_t is defined here, it is inherently coupled with the position E_C.

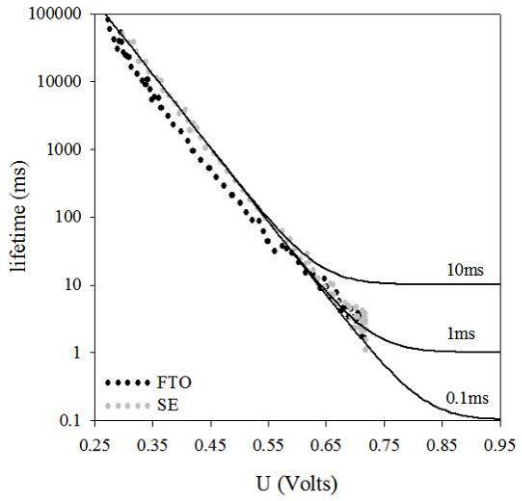

Figure 56 Measured and fitted apparent electron lifetimes calculated from a PV decay transient. τ_0=1ms fitting parameters; E_C-$E_{F,redox}$=0.95eV, N_C=10^{21}cm^{-3}, T_C=800K, N_t=10^{19}. Fitting was guided by the SE data as it was more ideal. Table 7.6-1 shows how varying parameters required others to be modified to maintain a fit.

Table 7.6-1

Fitting for constant E_C-$E_{F,redox}$=0.95eV and T_C=800K adjusting for τ_0 (ms)

N_t (cm^{-3}) \ N_C (cm^{-3})	10^{20}	10^{21}	10^{22}
10^{18}	1	10	100
10^{19}	0.1	1	10
10^{20}	0.01	0.1	1

τ_0 (ms)

Fitting for constant τ_0=1ms and T_C=800K adjusting E_C-$E_{F,redox}$ (eV)

N_t (cm^{-3}) \ N_C (cm^{-3})	10^{20}	10^{21}	10^{22}
10^{18}	0.95	1.05	1.105
10^{19}	0.85	0.95	1.05
10^{20}	0.75	0.85	0.95

E_C-$E_{F,redox}$ (eV)

As depicted in Figure 56, adequate fits were achieved using similar values for N_C and E_C-$E_{F,redox}$ as when fitting the QFL. However, the lifetime used for fitting the 1 sun SE electrode data (17ms in Figure 45) is larger than the minimum measured apparent electron lifetime. If the extrapolation of the apparent electron lifetime is correct, then the conduction band electron lifetime should certainly be 1ms or less.

Another minimum that can be set in terms of the parameter used is the total trap density N_t. In this case, a minimum N_t of 10^{18}cm^{-3} was estimated by measuring at the highest experimentally possible photovoltage of c.a. 750mV. Accordingly, using the information provided in Table 7.6-1, and the fact that the lowest measured apparent electron lifetime was 1ms, N_C then cannot be less than 10^{20}cm^{-3}. This in turn sets a lower limit on E_C-$E_{F,redox}$ to 0.90eV (see

Table 7.5-2).

Clearly, there is certain flexibility in the use of parameters to fit the data. Nevertheless, the lifetimes being estimated from the fitting of the QFL contradict those obtained by apparent lifetime measurements. To a certain extent, this is not surprising because the fitting of the QFL assumes ideal behaviour, whereas this is not always the case.

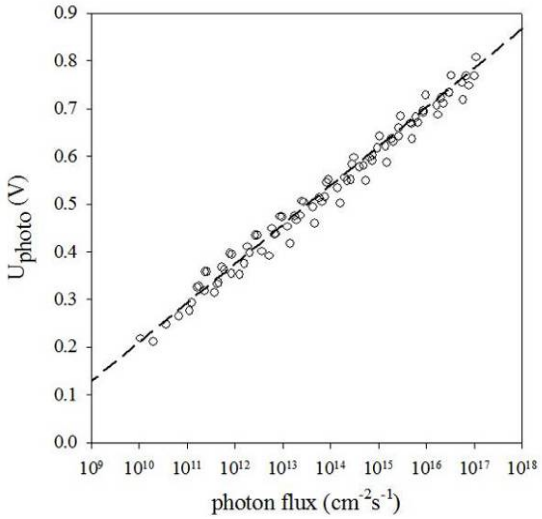

Figure 57 Open-circuit voltage versus intensity for 5 cells with and without the SE. $dU_{photo}/dlog(I)$=82meV, essentially the same as that in Figure 53.

The values obtained for T_C obtained by PV charge extraction were generally higher from the IMVS/PV decay. For example, the data in Figure 58 results in a T_C value of 1100K and apparent electron lifetime data in Figure 56 results in a T_C value of 800K. Again, this discrepancy arises because of the assumed ideality of the cells. The indirect method to determining T_C by measuring the apparent lifetime assumes an ideal dependence of the photovoltage.

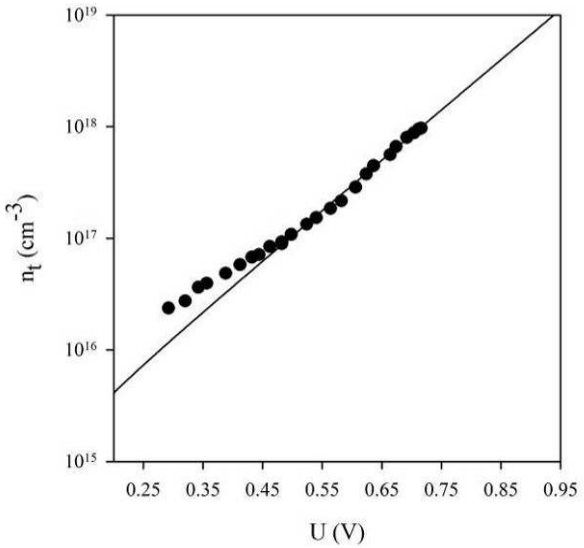

Figure 58 Charge extraction data. Fitting resulted in T_C=1100K and N_t=$10^{19}$$cm^{-3}$ when E_C-$E_{F,redox}$=0.95eV.

The model assumes that the rate of back reaction varies according to the Boltzmann relationship;

$$k_0 n_C = k_0 N_C \exp\left(-\frac{E_C - E_F}{k_B T}\right) \qquad 71$$

If there are surface recombination states, then the overall rate constant for back reaction will be dependent on electron concentration, and thus result in a variable electron lifetime dependent on the position of the QFL.

Empirically to account for the surface states we can write;

$$\upsilon = k_0 n_C^{\gamma} = k_0 N_C^{\gamma} \exp\left(-\gamma \frac{E_C - E_F}{k_B T}\right) \qquad 72$$

This avenue, however, was not explored because of the added complications. Nevertheless, it is possible to fabricate DSCs that demonstrate almost ideal characteristics relating to the electron lifetime/back reaction rate constant and conduction band electron density.

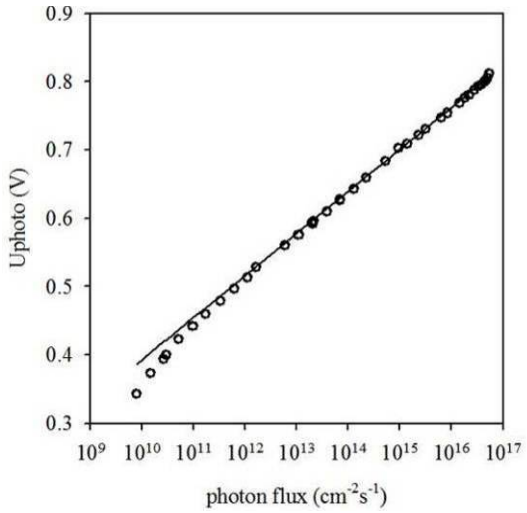

Figure 59 Example of almost ideal cell with a gradient of 62mV per decade of illumination. Fitting was biased towards the high intensity data because of known additional effects of electron recombination via the FTO substrate, due to imperfect passivation by use of a blocking layer. Physical parameters for fitting were E_C-$E_{F,redox}$=1.0eV, N_C=$10^{21}$$cm^{-3}$, τ_0=10ms, d=5μm and α=1000cm^{-1}. The colloid used was that prepared via the acetic acid in-house route.

This highlights the importance of preparation of the TiO_2 film and the impact on what is measured. Unfortunately, cells containing a SE were not manufactured using the in- house colloid. However, this almost ideal cell was used to test the quasi-static formulation and determine electron lifetimes via transient methods over a range of temperatures (see section 8).

7.7 Charge Extraction Along the iV Curve

It has been directly established for the measurements on cells with the secondary electrode that there is indeed a measurable QFL within the TiO_2 film that can be described by a diffusive model for electron transport. The interaction of QFL (and hence the free electron density) with the trap distribution has thus far only been explored for homogeneous distributions, e.g. determination of apparent electron lifetimes via IMVS and the PV decay. As pointed out previously, if the trap states are not recombination sites (surface states), they then play no role in describing the photostationary characteristics of a cell.

Würfel et. al. [125] measured the electron density at short-circuit. They found that the extracted charge under short-circuit conditions was equivalent to that extracted from PV decay when the voltage across the cell was c.a. 550mV, and hence concluded that at short-circuit there was a significant electron density and QFL within the film. The conclusions are similar to those obtained by O'Regan and Lenzmann [108] and Boschloo et. al. [109] (see section 4.6). These methods only estimated the internal QFL at short-circuit, although one method measured the trapped electrons directly [125], and the other measured the "residual" average voltage [109].

With the knowledge of how the QFL profile behaves for different applied biases, it is now possible to test in conjunction, the ideas of an exponential trap distribution and the diffusive model for electron transport.

The local trapped electron density at x is determined by the local QFL level ($E_F(x)$-$E_{F,redox}$). For an exponential trap distribution the trapped electron density is given by;

$$n_t(x) = N_t \exp\frac{E_F(x) - E_C}{k_B T} \qquad 73$$

Figure 60 illustrates a typical set of calculated QFLs that correspond to different points on the iV curve. Typically, the QFL varies strongly for x<0.5μm and then is flat throughout the film. For the rest of the film (x>0.5μm) the QFL does not vary until the applied bias becomes equal to the internal QFL. It is, therefore, easy to foresee that the trapped electron density in the TiO_2 will not vary significantly until the applied bias becomes equivalent to the internal QFL. This corresponds to the measured inflection of the QFL depicted in Figure 55.

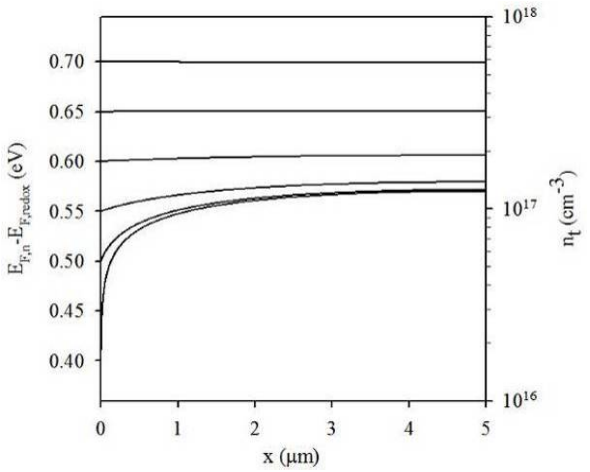

Figure 60 Example of how the QFL and the resultant trap electron density varies for different biases at x=0. Standard parameters were: D_0=0.04cm^{2}s^{-1}, τ_0=1ms, E_C-$E_{F,redox}$=0.95eV, N_C=10^{21}cm^{-3}, N_t=10^{19}cm^{-3}, T_C=1000K. The density of trapped electrons is directly proportional to the QFL so only one set of curves is required to represent both.

Figure 61 demonstrates a few examples of how varying the diffusion coefficient and electron lifetime affects the QFL and the trapped electron density. The dependence on the diffusion coefficient is straightforward, whereby a lower diffusion coefficient gives rise to a higher internal QFL to support the photostationary current. This in turn gives rise to a higher trapped electron density. The electron lifetime only affects the QFL profile when L_n<3d, giving rise to a maximum QFL somewhere within the film and not at x=d.

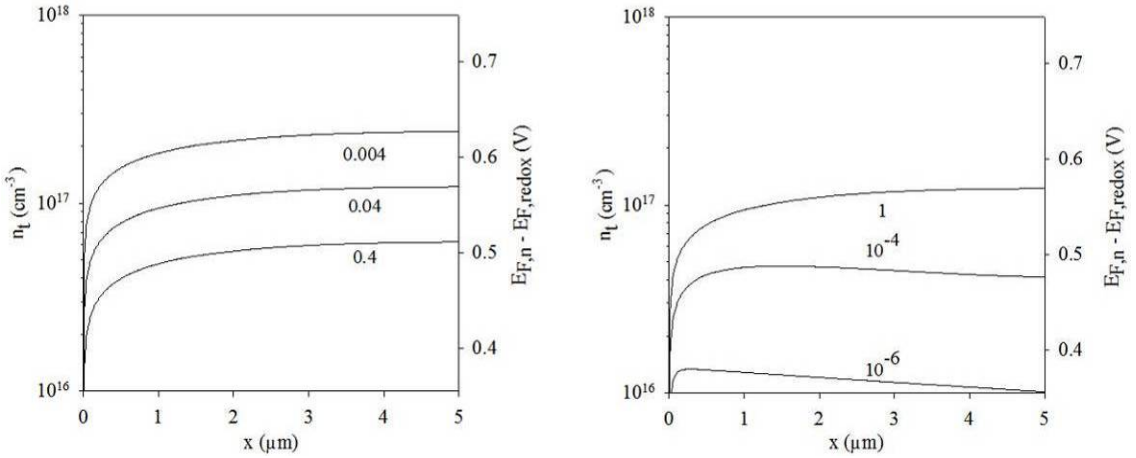

Figure 61 Left - effect of electron diffusion coefficient (cm^{2}s^{-1}). Right - effect of electron lifetime (ms). Standard parameters were: D_0=0.04cm2s-1 (right), τ_0=1ms (left), E_C-$E_{F,redox}$=0.95eV, N_C=10^{21}cm^{-3}, N_t=10^{19}cm^{-3}, T_C=1000K. When L_n>3d the QFL profiles are independent of the electron lifetime but shift according to the diffusion coefficient. The position of the QFL only becomes a function of the lifetime when L_n<3d.

Having shown how the electron diffusion coefficient and lifetime affect the QFL and hence the trapped charge, Figure 62 illustrates how modifying the trap distribution alters the profiles of the trapped charge, whilst maintaining a

unique QFL profile. It is straightforward to appreciate that by increasing the trap density, the trapped charge will increase linearly. Decreasing the characteristic temperature of the distribution effectively biases it to have more states closer to the conduction band. This is why in Figure 62 the profile with a T_C value of 500K has fewer trapped electrons for the same QFL profile.

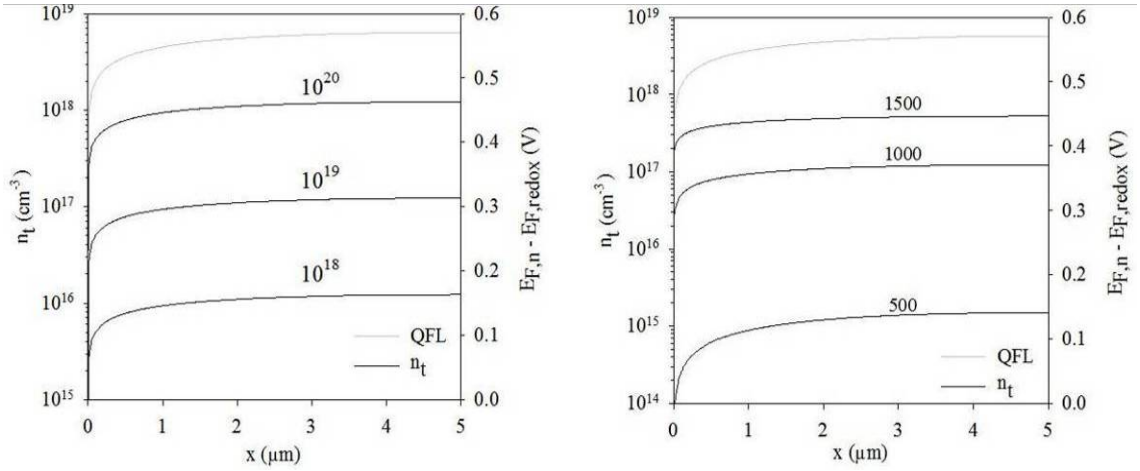

Figure 62 Effect of varying the total trap density N_t (left) and trap characteristic temperature T_C (right) on the trapped electron density, for an identical QFL profile at short-circuit. Standard parameters were: D_0=0.04cm^{2}s^{-1}, τ_0=1ms, E_C-$E_{F,redox}$=0.95eV, N_C=10^{21}cm^{-3}, N_t=10^{19}cm^{-3}, T_C=1000K.

It is evident that there is an important link between the density of trapped electrons and the profile of the QFL. If there is no significant barrier to extraction at the FTO|TiO_2 interface, the measurements of the QFL only provide a measure of the QFL at two points, allowing one to infer the QFL between these two points. However, correlating the inferred QFL profiles with the trapped density for each inferred profile provides an interesting test of the applied models.

The basic concept to measure the stored charge along the iV curve, is to hold the cell at any point along the iV curve and to then simultaneously cease illumination and integrate the current output from the cell. One can imagine the simplest way to achieve this would be to place a variable load resistor and a current follower in series with the cell. In this way, the trapped charge would simply be the integral of the current transient upon cessation of illumination. This basic setup has two problems. Firstly, the cell would have to discharge through a variable load resistor, reducing the current density and thus increasing the integration time. Secondly the integration of current transients from DSCs are complicated at long times by the powerlaw tendency of the decay currents transients. (This characteristic is illustrated in Appendix B).

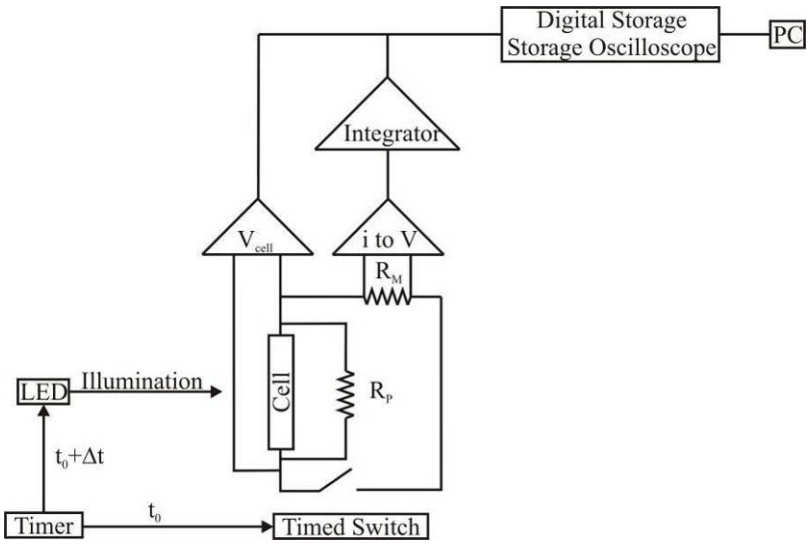

Figure 63: Schematic representation of how the charge extraction along the iV curve was measured.

A different approach was therefore taken by modifying the PV decay charge extraction technique. This apparatus was specifically designed to allow facile integration of small currents over long timescales. The cell was held at various points along the iV curve by adjusting the load by use of a resistor box (R_P). The small measuring resistor of the measuring apparatus was placed in parallel with the load resistance of the cell, but the switch would be closed only when integrating. Since the input resistance for the charge extraction kit is smaller than the load resistor, the discharge of the cell is faster, reducing integration times.

Integration of current was initiated with the still cell in a photostationary state, i.e. still illuminated. The short time interval between short-circuiting the cell and cessation of illumination was well defined, so that the measured integrated charge before switching off the illumination could be subtracted from the total measured charge. This approach was taken because of the impossibility of simultaneously initiating the integrator while switching the illumination. As the cell was at short-circuit in this time interval, the extra photogenerated charge was assumed to be always equal. The extra integrated charge due to the time delay was also checked by careful numerical integration of the photocurrent decay profile at short-circuit (through a 10Ω resistor) and also by sequentially increasing the time delay and extrapolating back to a time delay of 0s. This was also crosschecked by the instantaneous square wave response of a photodiode acting in place of the cell. Once the integrator was initiated, the current from the cell would discharge through the two resistors in parallel. The fraction flowing through the measuring resistor was readily calculated in each case.

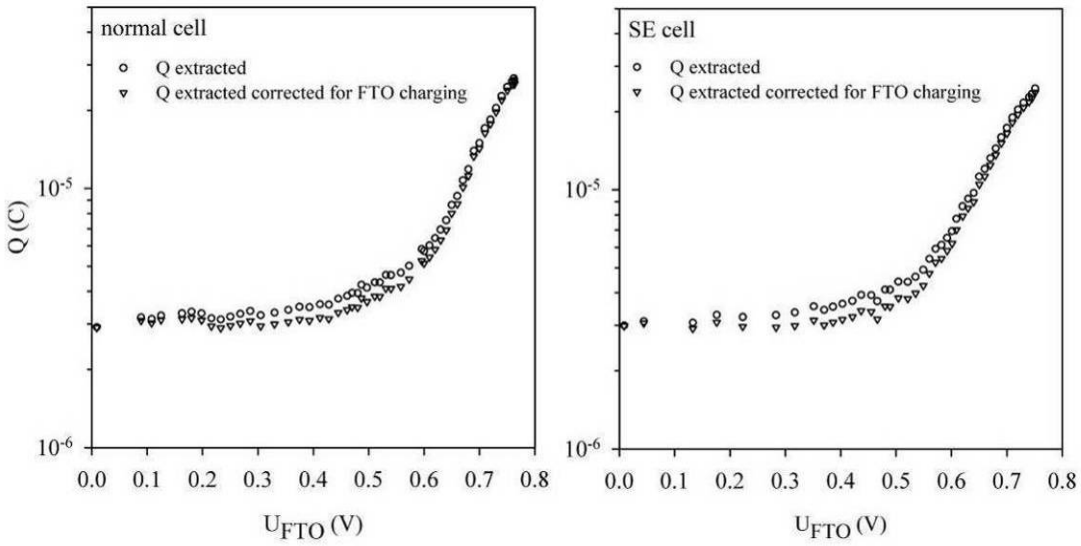

Figure 64 iV charge extraction data for two cells, one a normal cell (left) and another containing the SE (right). The data shown are corrected for loss of current flow through the load resistor (R_P), and the extra integrated current due to the time delay Δt=3.7ms. An added correction for a hypothetical Q=CV charging with C=5μFcm^{-2} (1μF for the 0.196cm^2 cell) is also shown. The data points at $U_{FTO}\approx 0$ were obtained via numerical integration of the current decay transient and used as a crosscheck reference to correct for the extra integrated current. This resulted in an accuracy of 10% in the measured charge.

The general nature of the measured trapped electron density along the iV curves was as expected, whereby there was an inflection when the applied bias approached the short-circuit QFL inside the TiO_2, c.a. 500mV. At this point, given that the QFL becomes homogeneous, further increase in the bias resulted in an exponential increase in measured charge.

The splitting of the current through the two resistors was only noticeable at low biases (200mV) because the measuring resistor (R_M) of the integrator was low (10Ω) when compared to load resistor values (80Ω to 5MΩ). The final correction added to the charge profiles was the hypothetical Q=CV charging. A value of 5μFcm^{-2} was used as it gave rise to a flat charge profile between 0mV and 500mV. The reason for this is evident in Figure 65 where the modelling suggests little change in the charge density up to c.a. 500mV. Significant charging of the substrate though, is unlikely, because such large values were never observed for electrodes containing only a blocking layer [38].

Charge extraction measurements along the iV curve were performed on two cells, one containing the SE electrode (used to also measure the QFL) and a normal optimised cell. Their iV curves were similar with virtually identical short-circuit current densities and open-circuit voltages. The trap distribution parameters were obtained via PV decay charge extraction and the resulting fit

is shown in Figure 65. The behaviour of the QFL was obtained in-situ employing the SE cell.

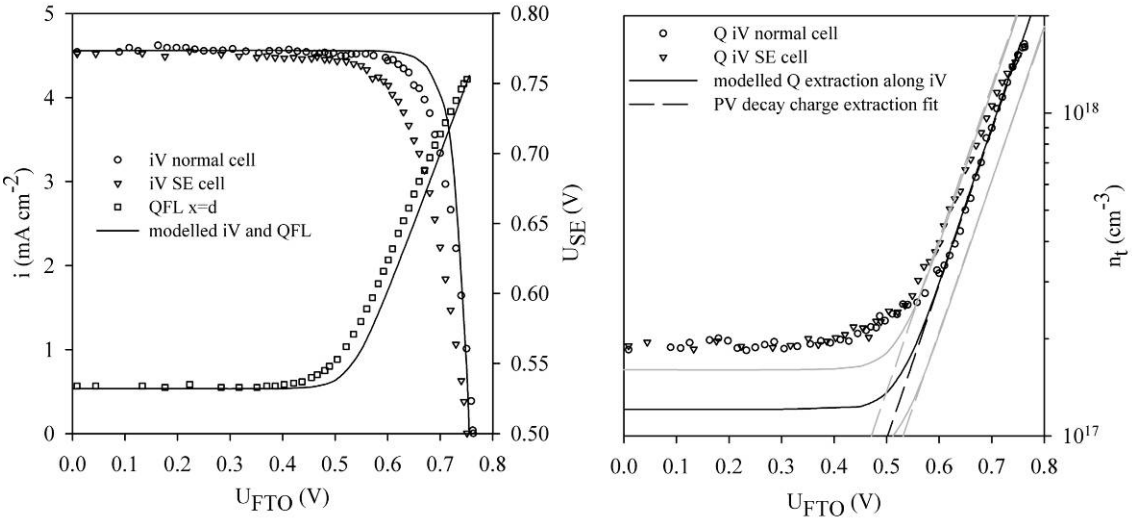

Figure 65 Left: Corresponding iV curve (normal cell and SE cell) and QFL (SE cell only) at x=d as a function of load voltage (U_{cell}). The improved fill-factor of the cell not containing the SE is a result of optimisation of the FTO outside the active zone by deposition of gold to reduce series resistance. The fitting was achieved in a similar manner as described in section 7.5, using the parameters in Table 7.7-1 and $N_C=10^{21}cm^{-3}$, d=5µm, $I_0=4.6x10^{16}cm^{-2}s^{-1}$ and $\alpha_{532nm}=2000cm^{-1}$.
Right: Measured charge extraction along the iV curve and the theoretical trapped charge according the QFL profile and trap distribution profile. Also shown is the resulting fit from measuring the trap density via the PV decay method where T_C=1050K. N_t varied according to E_C-$E_{F,redox}$. Shown in grey are the 95% confidence range for the PV decay charge extraction fit, and the subsequent effect on modelled iV charge extraction

Due to lack of full knowledge of the parameters defining electronic properties of the DSC, the uncertainty was translated to the parameters required to fit the experimental data demonstrated in Table 7.7-1). Nonetheless, the diffusion length remained invariant.

Table 7.7-1

D_0 (cm^2s^{-1})	E_C-$E_{F,redox}$ (eV)	N_t (cm^{-3})	τ_0 (ms)	L_n (µm)
0.4	0.99	$2.2x10^{19}$	1.7	85
0.1	0.96	$1.5x10^{19}$	5.5	
0.04	0.93	$1.1x10^{19}$	17	
0.01	0.90	$7.x10^{18}$	55	

The variation of N_t reflects the variation of E_C-$E_{F,redox}$. When a lower D_0 is used, E_C has to be shifted upwards to allow the predicted QFL and measured QFL to line up. This larger energy range between the $E_{F,redox}$ and E_C then results in an increased number of traps N_t between the two energies. However, the trap density profile $n_t(E_F)$ remains the same.

For high potentials above the inflection point of c.a. 500mV, the fit is in

excellent agreement with the data acquired from the normal cell. This is not surprising since for high potentials the QFL is homogeneous, and thus the measured charge is identical to that measured via PV charge extraction.

The quality of the agreement of the fitting of the SE cell provides some insight into the behaviour of the artefacts caused by the introduction of the SE. The measurement of the QFL for intermediate biases was always above that predicted by modelling. A possible internal IR drop has already been discussed as a possibility in section 7.2. The extra potential measured by the SE at intermediate applied biases above the inflection point has been attributed to the fact that part of the cell is always in a quasi open-circuit state, elevating the potential measured at x=d (see Figure 47). This is partly confirmed by the extra charge measured at these potentials, above the inflection point of 500mV and below the open-circuit voltage. In other words, when the data from the two charge extraction techniques are compared for the SE cell, the iV extracted charge for a defined bias will always be larger than that measured by the PV decay charge extraction method.

For simplicity, Figure 65 does not include the calculated total electron density (free and trapped). However, when the free electron density is taken into consideration for the total electron density, there is for lower D_0, are marked increase in total electron density at higher potentials, as illustrated in Figure 66.

The fact that the there is no deviation by the two methods of charge extraction at high potentials, suggests that the free electron density is insignificant in terms of total number of electrons ($n_t >> n_c$). The fitting of the QFL is possible for any combination of D_0 and τ_0 so that the diffusion length remains invariant. Some limits have already been imposed on the values of these, where D_0 should be no larger than the bulk anatase value, and τ_0 should be no larger than the apparent values measured via IMVS or PV decay. However, it now appears that it is possible to set a lower limit for the diffusion coefficient within a magnitude of bulk anatase value, $1 cm^2 s^{-1}$ to $0.1 cm^2 s^{-1}$.

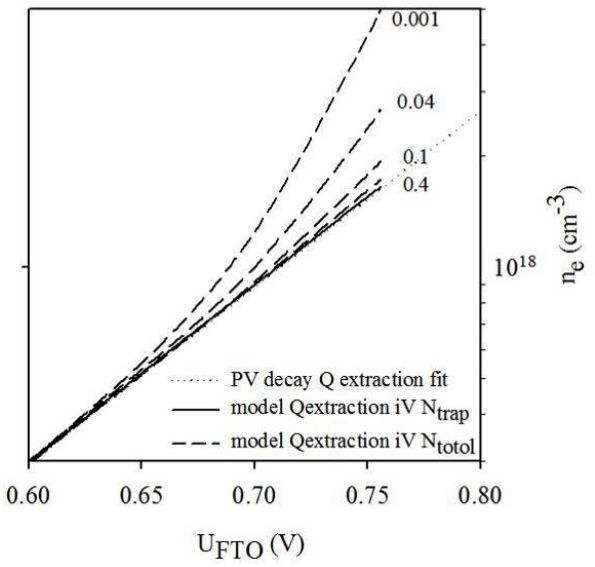

Figure 66 Comparison of how the total electron density varies according to D_0 with the subsequent parameters (see Table 7.7-1) and $N_C=10^{21}cm^{-3}$, d=5μm, $I_0=4.6x10^{16}cm^{-2}s^{-1}$, $\alpha_{532nm}=2000cm^{-1}$.

There is, however, still a disparity between the measured and modelled charge for applied biases below 500mV (modelling $1.2x10^{17}$ +/- $4x10^{16}cm^{-3}$ and experimental $1.9x10^{17}cm^{-3}$ +/- $2x10^{16}cm^{-3}$), in that the error due to the uncertainty of the trap distribution and the measurement technique are not enough to account for the disparity. However, the inferred energetic profile for the trap distribution may be incorrect. The uncertainty describing the trap distribution is only valid for the potential range through which the trap distribution is measured, where values below 300mV were difficult to determine. It could be possible that the trap distributions are not exponential at these lower potentials and any difference in their distribution would be more manifest at the lower potentials.

As for the uncertainty with the QFL measured at x=d, a difference in 30mV is enough to justify the extra trapped charge. For example, the measured voltage for the SE at short-circuit was 533mV and the charge measured for this short-circuit condition was $1.9x10^{17}cm^{-3}$. According to the PV charge extraction data, this charge density corresponds to an open-circuit voltage of 560mV, the difference being c.a. 27mV, i.e. the calculated trapped electron density will be lower than the measured one.

Although the modelled and experimental data relating the QFL and the trapped charge along the iV curve do not agree exactly, general trends were followed. These further confirm a large electron density and support a large electron density gradient within the TiO_2 film.

7.8 Direct Measurement of the Temperature Coefficient of the Electron Quasi-Fermi Level at Short and Open-Circuit

The temperature dependence of the quasi-Fermi level at x=d at short-circuit was measured using the secondary sensing electrode. The results show the quasi-Fermi level decreases with increasing temperature as predicted for diffusive electron transport. The temperature dependence of the open-circuit photovoltage was also measured and an expression derived. A shift in the conduction band edge in the TiO_2 and a decrease in the electron lifetime with increased temperature were postulated to account for deviations from calculated values.

7.8.1 Short-Circuit

Three effects of temperature on the QFL profiles are looked at, two of which are shown to be of minor consequence when compared with a third. The two minor effects are the temperature dependence of the density of states of the conduction band and the diffusion coefficient.

The QFL is defined as;

$$QFL(x) = E_F - E_{F,redox} = k_B T \ln\left(\frac{n_C(x)}{N_C}\right) + \left(E_C - E_{F,redox}\right) \qquad 74$$

All the parameters defining the QFL are temperature dependent. If the collection of injected charge is assumed to be unity (when L_n>3d) then under photostationary conditions the free electron density (n_C)is defined solely by the diffusion coefficient (D_0) (see section 4.6).

The impact of changing the value of N_C or D_0 has already been demonstrated in section 4.6. Variation of N_C only impacts on the value of the QFL and not n_C, while a larger D_0 affects the free electron density directly and, thus, the QFL.

These effects are secondary when compared to the required shift in the QFL to maintain a constant free electron density and, hence, current density. The free electron density profile will have to adjust to maintain the charge balance, where the number of injected electrons is equal to that collected at x=0.

The temperature dependence of N_C can be understood by the following expression [101];

$$N_C = 2\left(\frac{2\pi m_n k_B T}{h}\right)^{3/2} cm^{-3} \qquad 75$$

As for the diffusion coefficient Forro et. al. [134] have reported for T>160K, the mobility (μ_0) of electrons in single crystal anatase TiO_2 decreases with temperature in proportion to exp(T_0/T), with T_0=850K.

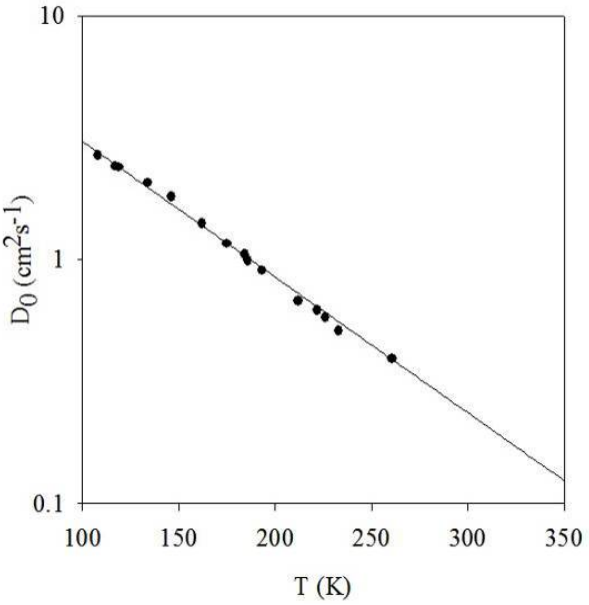

Figure 67 High temperature D_0 for singe crystal anatase TiO_2, inferred from Hall mobility (μ_H) values by Forro et. al. [134]

It follows from the Einstein relationship ($D_0=\mu_0(k_BT/q)$) that D_0 should vary with Texp(T_0/T). According to the Hall mobility measurements by Forro et. al., this corresponds to a room temperature value of $D_0\approx0.4cm^2s^{-1}$ for single crystal anatase TiO_2.

Figure 68 and Figure 69 are artificial examples of individual temperature effects of N_C and D_0 on the QFL profiles. These examples are artificial because only the respective values of N_C and D_0 were varied and not the temperature term in the solutions to the continuity equation (T=295K in these artificial examples). The QFL profiles are those required to sustain the unchangeable photocurrent, or electron flux.

As the density of states increases with temperature (where N_C increase is proportional to $T^{3/2}$) the QFL level decreases because there are more states for a given energy while the electron density remains constant. As the diffusion coefficient decreases with temperature, the QFL rises, this time because a greater electron density gradient is required to sustain the electron flux.

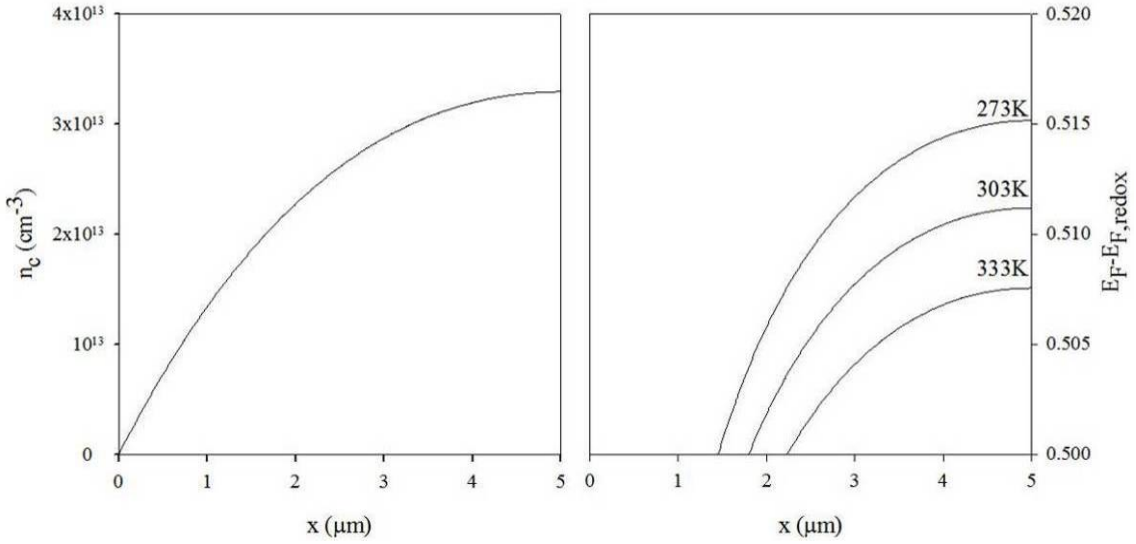

Figure 68 Example of how the temperature dependence of N_C affects the QFL profiles under short-circuit conditions. N_C values used were $8.8x10^{20}$, $1x10^{21}$ and $1.2x10^{21}cm^{-3}$ for 273, 303 and 333K respectively. This assumes $N_{C,295K}=10^{21}cm^{-3}$. Fixed parameters were, d=5μm, $I_0=10^{17}cm^{-2}s^{-1}$, $\alpha=2000cm^{-1}$, $E_C-E_{F,redox}=0.95eV$ and $\tau=10^{-4}s$.

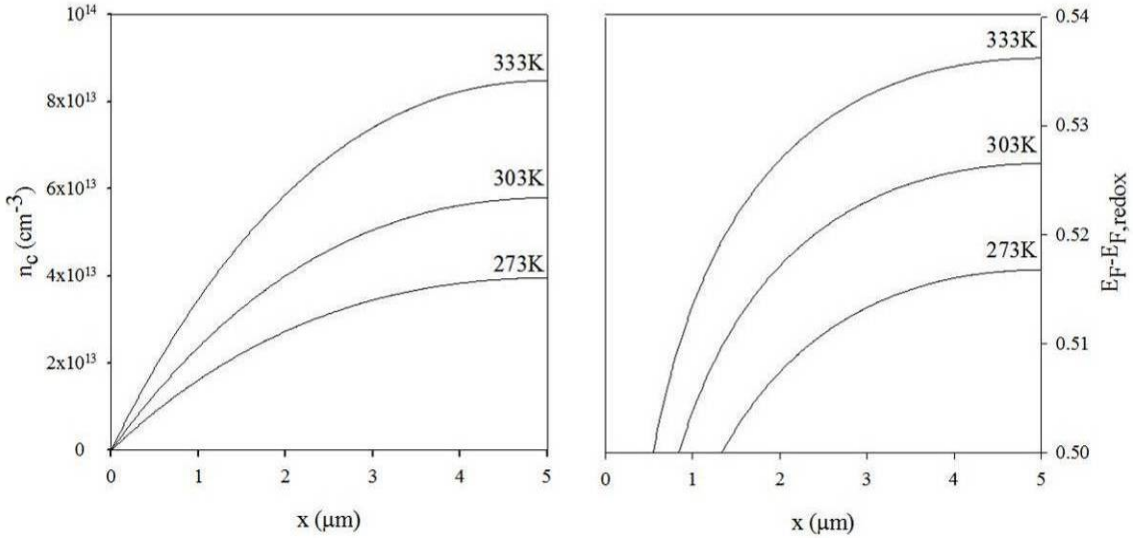

Figure 69 Example of how the temperature dependence of D_0 affects the QFL profiles. D_0 values used were inferred from Forro et. al. [134] with the extrapolation shown in Figure 67. D_0 values were 0.33, 0.23, $0.15cm^2s^{-1}$ for 273, 303 and 333K respectively. N_C was held at $10^{21}cm^{-3}$ and other parameters used were the same as in Figure 68.

The importance of these examples is that the resultant shift in the QFL level at x=d is relatively small, <5mV in the exemplified temperature range. Overall, both effects are opposite (though the change in D_0 has a greater impact) and secondary when compared to the thermal term relating the free electron density (k_BT) to the QFL.

Solutions to the continuity equation give the required electron density and gradient to sustain a photocurrent. The QFL is then related to the local

electron density by;

$$n_C(x) = N_C \exp\left(-\left(E_C - E_F(x)\right)/k_B T\right) \quad 76$$

The important point to keep in mind is that if the photocurrent remains unchanged for differing temperatures then the free electron density also remains unchanged, but with a varying temperature, the QFL has to also vary to compensate. If for simplicity, the temperature dependence of N_C is ignored, then for two different temperatures one can write;

$$N_C \exp\left(-\left(E_C - E_{F,1}\right)/k_B T_1\right) = N_C \exp\left(-\left(E_C - E_{F,2}\right)/k_B T_2\right) \quad 77$$

Thus the temperature dependence of the QFL can be approximated [137] to the following linear expression;

$$E_C - E_{F,T_2}(x) = \frac{T_2}{T_1}\left(E_C - E_{F,T_1}(x)\right) \quad 78$$

This expression suggests that if the QFL is measured, it should decrease linearly as the temperature is increased. It is only derived to show the linear relationship. The QFL profile and its shift is calculated according to the solutions to the continuity equation.

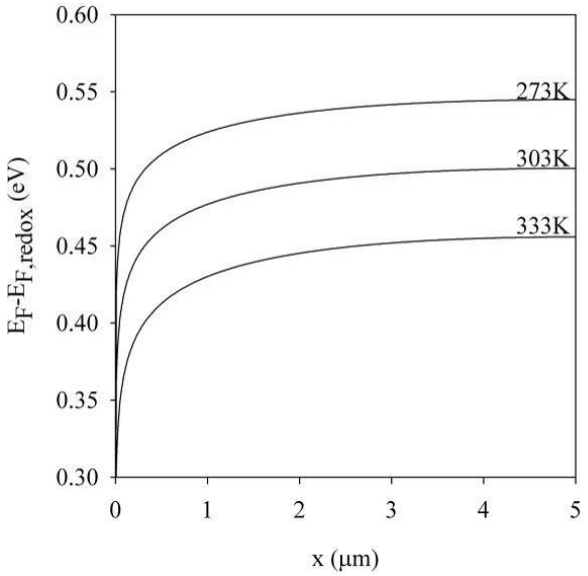

Figure 70 Profiles of the QFL calculated using the same values as in Figure 68 where Nc=10^{21}cm^{-3} and D_0=0.4cm^{2}s^{-1}. The modelling predicts the QFL should decrease with temperature. N.B. $n_C(x)$ remains unaltered.

Over the same temperature range the shifts in the QFL profile due to k_BT term is c.a. +/- 50meV, an order of magnitude greater than those due to N_C and D_0. This linear temperature dependence of the QFL was observed experimentally.

The slight offset of the data points can be attributed to the change of position

of the conduction band edge with respect to the redox potential. Analysing the charge extraction data for different temperatures (see Figure 72) can give insight into the magnitude of this shift. This is possible if one assumes that when the conduction band edge shifts with temperature, the trap energies also shift accordingly. Shifts in the conduction band energy are also observed in the presence of tertiary butyl pyridine. This is illustrated in Appendix C.

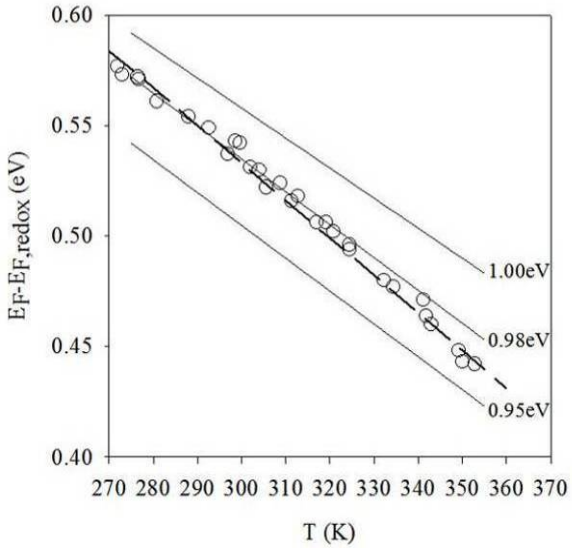

Figure 71 Experimental variation of the QFL relative to the redox Fermi level measured using the titanium secondary electrode (open circles). The lines were calculated using the same values as in Figure 68, and for completeness, also included the temperature dependence of N_C and D_0. E_C-$E_{F,redox}$ was varied as shown. The experimental data were fitted exactly when a shift of -0.2meV/K was imposed on the position of the conduction band edge (broken line). The data was derived by having an exact match between measurement and experiment at T=295K (i.e. room temperature).

The measured conduction band shift measured by the charge extraction technique (shown in Figure 72) suggests a larger shift but of the same order, than that inferred from the data in Figure 71. O'Regan and Durrant [138] estimated the temperature coefficient of the shift in the conduction band edge to be larger c.a. -1.7meV. However, the electrolyte used in the present experiments is different. One possibility for this shift of the conduction band edge could be due to the temperature dependence of the surface dipole potentials

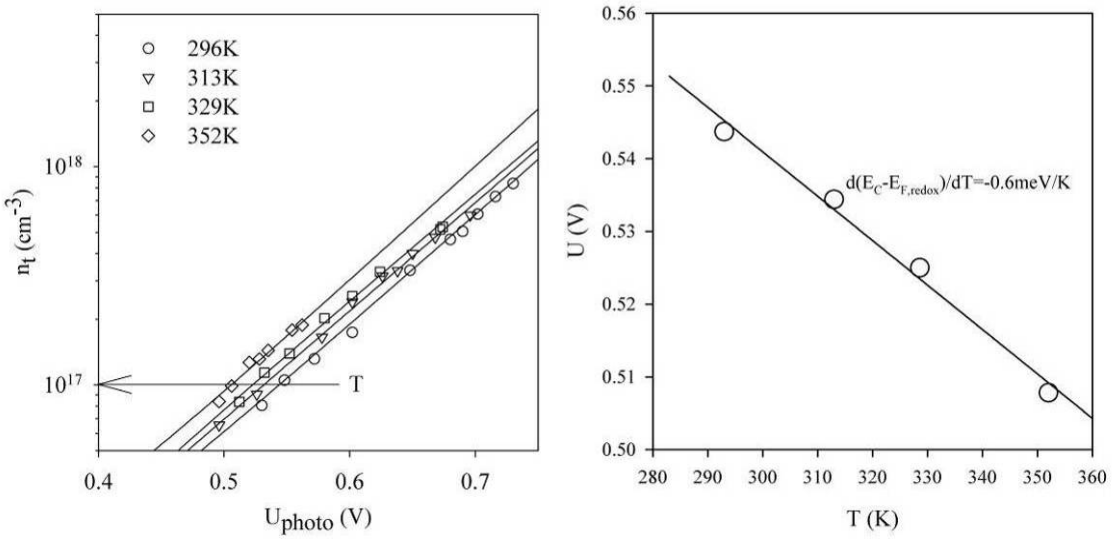

Figure 72 Left: Charge extraction data at various temperatures. Right: Shift of the trap distribution at $n_t=10^{17}cm^{-3}$. Temperature coefficient of the conduction band edge is estimated to be $d(E_C-E_{F,redox})/dT\approx-0.6meV/K$.

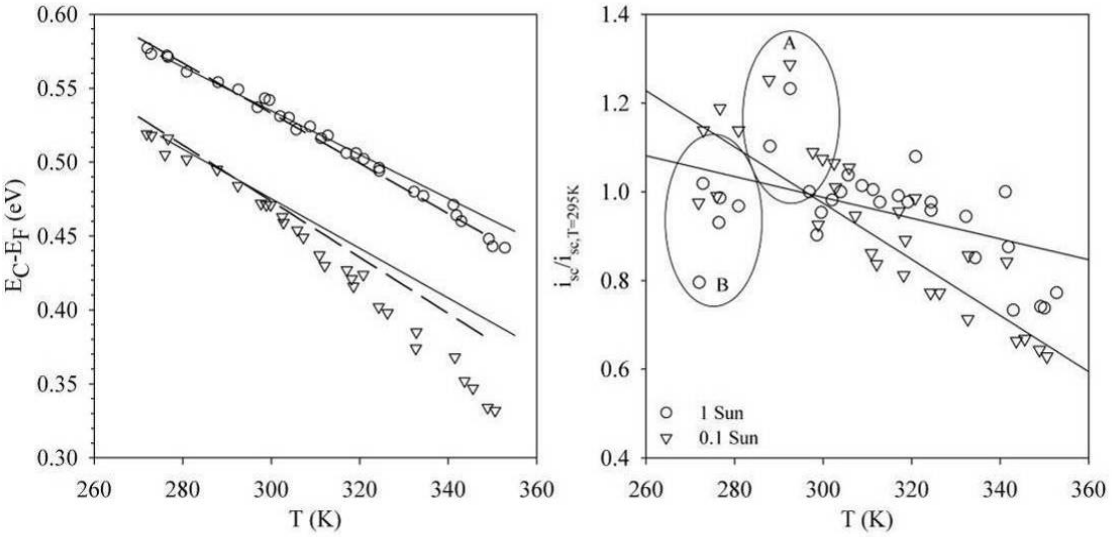

Figure 73 The left-hand-side plot compares the QFL measured at two intensities, at 1 sun and 0.1 sun. The 1 sun data is the same as presented in Figure 71. The calculated profile for 0.1 sun assumed the same parameters as that at 1 sun except for $I_0=10^{16}cm^{-2}s^{-1}$. Also included for the 0.1 sun data was the effect of the hypothetical conduction band shift (-0.2meV/K). Importantly, the right-hand-side plot shows how the short-circuit current varied with temperature, with a more pronounced decrease for the 0.1 sun data. As the temperature was decreased bellow room temperature, the short-circuit current values increased and then decreased due to condensation of water increasing the scattering (A) and then freezing reflecting light (B).

The temperature dependence of the QFL was also measured at 0.1 sun with a less ideal correlation between measured and predicted values. It must not be forgotten that the calculated lines are based on the QFL level at T=295K, and then extrapolated by varying the temperature in the solutions to the continuity equation. This is why there is better agreement for temperatures close to

T=295K. However, the movement of the conduction band edge to lower energies cannot account for the decline in the current densities. This decrease was more marked for the measurements at 0.1 sun. The decrease in the photocurrent suggests a decrease in the diffusion length of the electrons so that the assumption that L_n>3d is no longer valid.

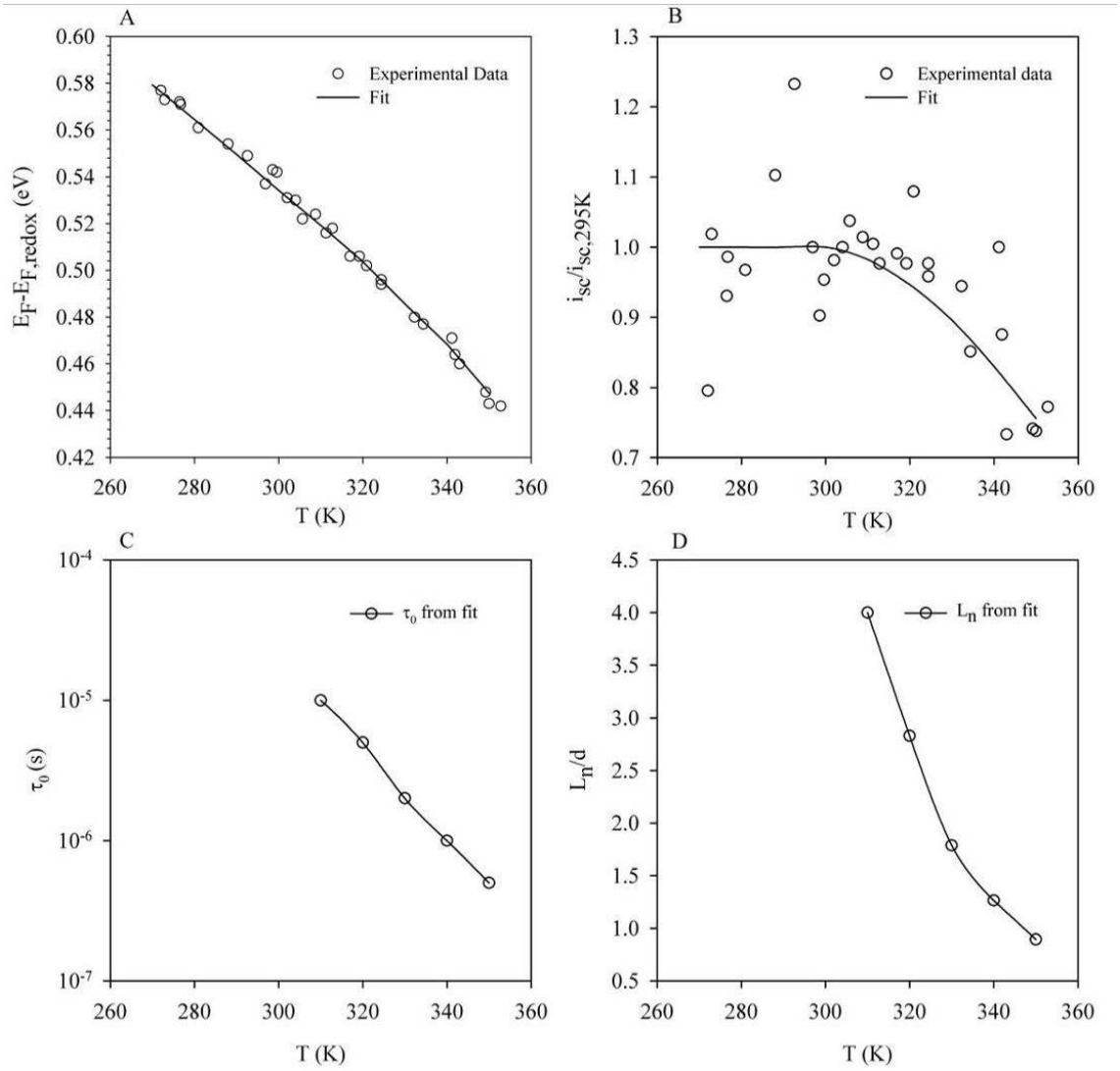

Figure 74 A: Fitting of the temperature dependent QFL (at x=d) data with consideration of the decrease in current density, by adjusting the electron lifetime and hence the electron diffusion length. B: Measured normalised short-circuit current density with the resultant modelled current density from the fit of the QFL temperature dependence. C: Adjusted electron lifetime to fit the QFL data exactly. D: Resultant variation in the electron diffusion length. No electron lifetime data is shown for T<300K because the diffusion length is sufficiently large to allow all electrons to be collected (L_n>3d). Other parameters were the same as those in Figure 73 but with a constant E_C-$E_{F,redox}$.

Figure 74 demonstrates that a decrease in the electron lifetime may be responsible for the decrease in the collected charge along with the deviation of the measured QFL data. However, this analysis did not hold for the 0.1 sun measurements. In this case, the required decrease in the electron lifetime to

match the calculated QFL to the measured QFL was too large, to the extent that the calculated short current density became much smaller than that measured. This could be the unexplained anomalous behaviour seen when the QFL is measured at low photon fluxes and high temperatures as shown in Figure 53.

For other cells (acetic acid route colloid) as in section 8, an electron lifetime decrease of two orders of magnitude was observed over a similar temperature range. If this is also the case with these SE cells, then the decrease in the photocurrent can be attributed to a decrease in the electron lifetime from c.a. 0.1ms to 1μs, the point where the calculated photocurrent begins to decrease (see Figure 74).

However, when the electron lifetime is adjusted to decrease the short-circuit QFL, the calculated open-circuit voltage does not correspond to the measured value. This is possibly due to the non-ideal behaviour of the open-circuit photovoltage, where electron lifetimes varying according to the position of the QFL.

Thus, deviations of the measured QFL from the calculated ones can be attributed to two factors. Firstly, according to the charge extraction data, the position of the conduction band appears to shift. Secondly, at higher temperatures the collection of charge is affected, suggesting a change in the diffusion length of the electrons, most probably due to a significant change in the electron lifetime.

A distinction has to be made here as to what affects the electron lifetime, i.e. ideal and non-ideal electron lifetime behaviour. Firstly the back reaction of electrons with I_3^- could have an Arrhenius relationship, where the reaction rate constant ($k_0=1/\tau_0$) is temperature dependent. This is explored in section 8.2. Secondly, the electron lifetime is most probably also dependent on the position of the QFL due to surface recombination sites. This QFL dependent electron lifetime is what would give rise to the non-ideal behaviour of the open-circuit photovoltage.

7.8.2 Open-Circuit

The position of the QFL under open-circuit conditions is also easily derived by noting that the conduction band density under open-circuit conditions is determined by the balance between photo-injection and back reaction.

$$n_C = \frac{I_{abs}}{k_0 d} = \frac{I_0\left(1 - e^{-\alpha d}\right)}{k_0 d} \qquad 79$$

If the only temperature dependent term in the above expression is k_0, the rate constant for back reaction of the conduction band electrons with I_3^-, then we shall see that the temperature dependence of the open-circuit photovoltage can be described by employing the Arrhenius expression;

$$k_0 = A\exp\left(E_A / k_B T\right) \qquad 80$$

where E_A is the activation energy and A is the preexponential factor. Substituting equations 79 and 80 into equation 77 gives the photovoltage as a function of temperature;

$$qU_{photo} = E_C - E_{F,redox} + k_B T\left[\ln\left(I_0/d\right) - \ln\left(N_C\right) - \ln\left(A\right)\right] + E_A \qquad 81$$

It therefore follows that the temperature coefficient of the photovoltage is given by;

$$\frac{dqU_{photo}}{dT} = k_B\left[\ln\left(I_0/d\right) - \ln\left(N_C\right) - \ln\left(A\right)\right] \qquad 82$$

Since the temperature dependence of N_C can be written in the form;

$$N_C(T) = N_{C,298}\left(\frac{T}{298}\right)^{3/2} \qquad 83$$

we can obtain;

$$\frac{dqU_{photo}}{dT} = k_B\left[\ln\left(\frac{I_{abs}}{d}\right) - \ln N_{C,298} - \frac{3}{2}\ln\left(\frac{T}{298}\right) - \frac{3}{2} - \ln\left(A\right)\right] \qquad 84$$

$$\frac{dqU_{photo}}{dT} \approx k_B\left[\ln\left(\frac{I_{abs}}{d}\right) - \ln N_{C,298} - \ln\left(A\right)\right]$$

The surprising result is that the temperature dependence of the open-circuit voltage is independent of the activation energy E_A but depends on the light intensity and on the preexponential factor A. Influence of the temperature dependence of N_C is, in fact, negligible.

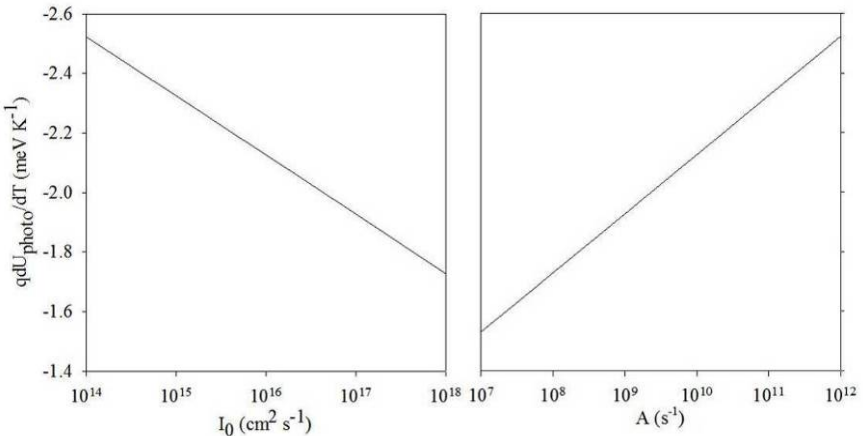

Figure 75 Predicted dependence of the temperature coefficient of the open-circuit voltage (U_{photo}) on the preexponential factor (A) for electron back reaction and on the light intensity (I_0). The left-hand-side plot is for $A=10^9 s^{-1}$ and variable I_0, while the right hand side plot is for $I_0=10^{17} cm^{-2} s^{-1}$ and variable A.

Figure 76 illustrates the experimental temperature dependence of the open-circuit voltage at two light intensities and the resulting fits. The slope was fitted by varying the pre-exponential factor A, and the absolute magnitude of the voltage was fitted varying the activation energy E_A.

The values obtained from the 1 sun linear fits correspond to room temperature $\tau_0=2x10^{-4}s$ and the 0.1 sun fits correspond to a $\tau_0=8x10^{-5}s$ However, the value of A is linearly dependent on the choice of N_C; e.g. decreasing N_C by an order of magnitude requires that A increases by an order magnitude to maintain the fit (see equation 82).

Again, it is observed that the calculated electron lifetime is smaller when the QFL position is lower. The broken line shown in Figure 76 for the temperature dependence of the photovoltage at a lower intensity was obtained by taking the values from the 1 sun measurement and lowering I_0. The lack of overlap highlights the non-ideal intensity dependence of the open-circuit voltage of these cells (82mV/decade). However, qualitatively it is interesting to note that at lower intensities the temperature coefficient of the open-circuit photovoltage becomes as expected more negative (see equation 84).

The L_n/d ratio, also shown in Figure 76, can be calculated by taking the fitting results of the temperature dependence of the open-circuit voltage to obtain a lifetime, and assuming a constant diffusion coefficient, calculate the diffusion length according to;

$$L_n = \sqrt{D_0 \tau_0} = \sqrt{\frac{D_0}{k_0}} \qquad 85$$

This calculation (shown in Figure 76) is to highlight the assumption where all injected charge is collected (i.e. L_n>3d) is possibly violated at higher temperatures and lower QFL levels. This, however is not enough to explain the difference in the measured QFL at the FTO and SE for the 0.1 sun measurements. Using the solutions to the continuity equation, it is impossible to calculate, using reasonable values, a QFL profile at open-circuit with a significant difference (c.a. 80mV for 0.1 sun and 350K) between the QFL at x=0 and x=d. As in the previous section, the data obtained at lower 0.1 sun intensities proved impossible to explain. This could be due to the physical disruption the intruding body that is titanium electrode, becoming more apparent at lower electron densities and higher temperatures.

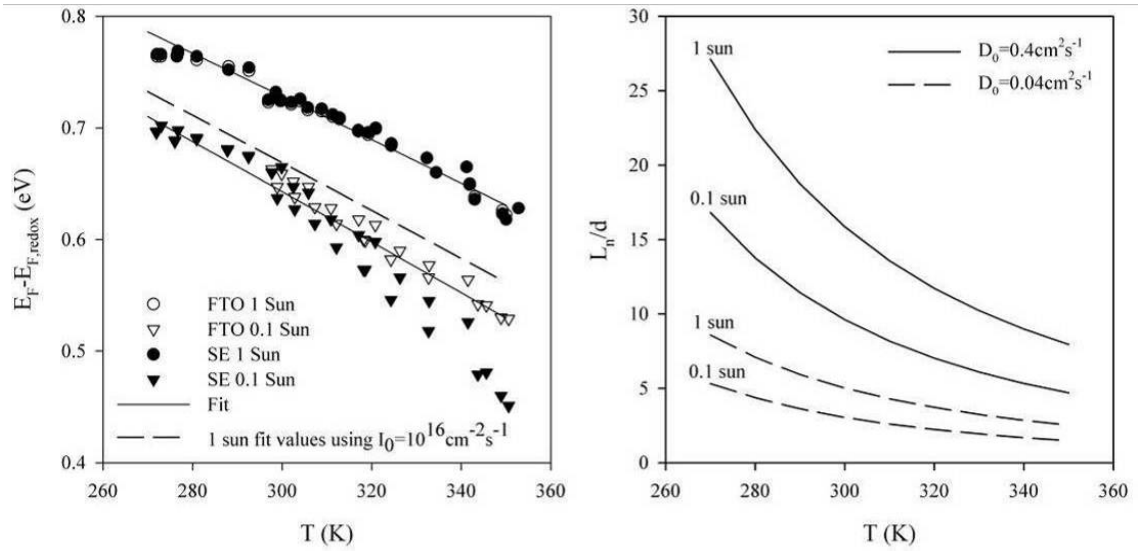

Figure 76 Left: Experimental temperature dependence of the open-circuit photovoltage (U_{photo}) at two intensities and the linear fits using equation 81. The following values were used: d=5μm; α=2000cm^{-1}; $N_{C,295K}$=10^{21}cm^{-3}; E_C-$E_{F,redox}$=0.98eV; resulting in A=10^8cm^{-1} and E_A=0.25eV for 1 sun (I_0=10^{17}cm^{-2}s^{-1}) data and A=4x10^8cm^{-1} and E_A=0.26eV for the 0.1 sun (I_0=10^{16}cm^{-2}s^{-1}) data. Also shown as a broken line, is how the 1 sun data fit shifts when only I_0 is modified from 10^{17}cm^{-2}s^{-1} to 10^{16}cm^{-2}s^{-1}.
Right: Resulting ratio of L_n/d when the reaction rate constant k_0 and hence the lifetime τ_0 are calculated using the Arrhenius expression in equation 80. Two different values of D_0 are used as an example.

A short analysis on the significance of the resultant values for the activation energies and pre-exponential factors was published [3]. These, however, are not now analysed because, as shown in the next section, these can vary significantly depending on the choice of unknown parameters.

8 Quasi-Static Analysis of Photovoltage Decay Transients and Measurement of the Activation Energy for Electron Back Reaction Via the Conduction Band

Numerical modelling is used to test the validity of the quasi-static approximation for the characterisation of DSC via PV decays. It has already been shown that a compact TiO_2 blocking layer slows down the rate of photovoltage decay, and that this QFL decay was confirmed to be spatially homogeneous with the use of an internal sensing electrode (see section 7.3).

Having shown that the quasi-static approximation can be used to fit experimental data, this analysis was used to infer the electron recombination rate constant as a function of temperature. According to the Arrhenius equation, the activation energy and pre-exponential factor for this reaction can be determined. The values of the activation energy and the pre-exponential factor were then used to predict, using the expression derived in section 7.8.2, how the measured open-circuit photovoltage should vary.

8.1 Quasi-Static Analysis of Photovoltage Decay Transients

The full numerical solution assumes a quasi-homogeneous medium where electric fields are screened out by the electrolyte and back reaction occurs solely via the conduction band. Illumination is via the substrate side. The continuity equation for the density of conduction band electrons is given by;

$$\frac{\partial n_C}{\partial t} = D_0 \frac{\partial^2 n_C}{dx^2} + \alpha I_0 e^{-\alpha x} - k_{CB}\left(n_C - n_{eq}\right) - \frac{dn_t}{dt} \qquad 86$$

and the continuity equation for the trapped electrons is given by;

$$\frac{dn_t}{dt} = N_t \left\langle \frac{df}{dt} \right\rangle = \left\langle k_t n_c (1-f) - k_d N_t f \right\rangle \qquad 87$$

The case of a simple exponential trap distribution between the redox potential and conduction band edge the density of states of this trap distribution is given by;

$$\begin{aligned} g(E_T) &= \frac{1}{1-\exp\left\{-\left(E_C - E_{f,redox}\right)/k_B T_C\right\}} \frac{N_T}{k_B T_C} \exp\left\{-\frac{E_C - E_T}{k_B T_C}\right\} \\ &\approx \frac{N_T}{k_B T_C} \exp\left\{-\frac{E_C - E_T}{k_B T_C}\right\} \end{aligned} \qquad 88$$

In the case of open-circuit voltage decay and no back reaction via the TCO

substrate, the gradient of conduction band electrons is zero at x=0 and x=d. The coupled equations 86 and 87 were solved numerically with a fully implicit approach employing a relaxation method using the differential equation solver *solvde* [139]. The photovoltage $U_{phot,num}$ was calculated from the conduction band density of electrons at x=0;

$$U_{photo,num} = \frac{k_B T}{q} \ln\left(\frac{n_c(x=0,t)}{n_{c,eq}}\right) \quad 89$$

Using the quasi-static approach, an analytical expression can be derived for the photovoltage decay. In essence, the quasi-static approximation envisages the system going through a series of steady-states. Thus, traps are dealt with by removing the dn_t/dt term in equation 86 and the diffusion coefficient D_0, and rate constant k_0, being substituted by their apparent values D_n and k_n (as described in section 4.8).

$$D_n = D_0\left(1+\frac{\partial n_t}{dn_c}\right)^{-1} \quad 90$$

$$k_n = k_0\left(1+\frac{\partial n_t}{dn_c}\right)^{-1} \quad 91$$

In the steady-state, the trap occupancy can be approximated to a step function where all traps below the quasi-Fermi level are occupied, and those above are empty;

$$f(E_T) = \theta(E_F - E_T) \text{ if } k_B T << |E_T - E_F| \quad 92$$

The thermal detrapping rate is assumed equal to its thermal equilibrium value;

$$k_d(E_T) = k_t \frac{1}{N_t} N_C e^{-(E_C - E_T)/k_B T} \quad 93$$

i.e. the detrapping rate is equal to the trapping rate when the trap lies at the conduction band edge, and is slower the further away (below) the trap lies from the conduction band. Using the approximate trap occupancy (equation 92) and integrating equation 88, one obtains an expression describing the total trapped electron density;

$$n_t = \int_{E_{f,redox}}^{E_F} g(E_t)dE_t = \frac{N_t}{k_B T_C}\exp(-E_C/k_B T_C)\int_{E_{f,redox}}^{E_F}\exp(E_t/k_B T_C)dE_t \qquad 94$$
$$= N_t\left\{\exp\left(-\left(E_C - E_f\right)/k_B T_C\right) - \exp\left(-\left(E_C - E_{F,redox}\right)/k_B T_C\right)\right\}$$

Simplifying because;

$$\exp\left(-\left(E_C - E_F\right)/k_B T_C\right) = \left(\frac{n_C}{N_C}\right)^{T/T_C} \qquad 95$$

and;

$$\exp\left(-\left(E_C - E_{F,redox}\right)/k_B T_C\right) = \left(\frac{n_{C,eq}}{N_C}\right)^{T/T_C} \qquad 96$$

then;

$$n_t \approx N_t\left\{\left(\frac{n_C}{N_C}\right)^{T/T_C} - \left(\frac{n_{C,eq}}{N_C}\right)^{T/T_C}\right\} \qquad 97$$

Differentiating yields another expression that relates the actual and apparent diffusion coefficient and rate constants;

$$\frac{dn_t}{dn_C} = \frac{N_t}{N_C}\frac{T}{T_C}\left(\frac{n_C}{N_C}\right)^{T/T_C - 1} \qquad 98$$

At all times under normal working conditions $n_c << N_C$, thus $dn_t/dn_C >> 1$ (with $T_C > T$).

The continuity equation for conduction band electrons (equation 86) can now be simplified. At open-circuit, the distribution of electrons in the conduction band is essentially homogeneous and thus the gradient negligible, $dn_C/dx = d^2n_C/dx^2 = 0$. It is important to note that this only holds true if the diffusion length is sufficiently large, or if the absorption of light is fairly homogeneous. In addition, by definition, the photovoltage decay occurs because of cessation of illumination, i.e. $I_{0,t>0} = 0$. For much of the decay time, the conduction band density of electrons is far greater than the thermal equilibrium value, thus $k_0(n_C - n_{C,eq}) \approx k_0 n_C$. Finally, because $dn_t/dn_C >> 1$, i.e. $dn_t/dt >> dn_C/dt$, then the left hand side of equation 86 can be set to zero, reducing the continuity equation for conduction band electrons to;

$$\frac{dn_t}{dt} = -k_0 n_c \qquad 99$$

Using the relationship in equation 98 and substituting into equation 99, and thus solving the differential equation, the quasi-static approximation for the photovoltage decay is;

$$U_{ph,qs}(t) = \frac{1}{1-T/T_C}\frac{k_B T}{q}\ln(c_1 - c_2 t) \qquad 100$$

where;

$$c_1 = \exp\left\{(T/T_C - 1)\frac{q}{k_B T}U_{ph}(t=0)\right\} \qquad 101$$

and;

$$c_2 = k_{CB}\left(1-\frac{T}{T_C}\right)\frac{N_C}{N_t}\frac{T_C}{T}\left(\frac{n_{c,eq}}{N_C}\right)^{1-T/T_C} \qquad 102$$

This treatment results in a linear plot on a logarithmic timescale for the photovoltage decay, which is observed in optimised cells. An important point to note is that the gradient of this decay profile is dependent on the trap characteristic temperature T_C and on the temperature T of the cell;

$$\frac{dU_{ph,qs}(t)}{d\ln(t)} \approx -\frac{k_B T}{q}\frac{1}{1-T/T_C} \qquad 103$$

The two figures below illustrate the calculated photovoltage decay transients using typical values of working cells. Figure 77 shows how the electron recombination rate constant affects the photovoltage decay transient, with the simple effect of shifting the whole decay profile to shorter timescales.

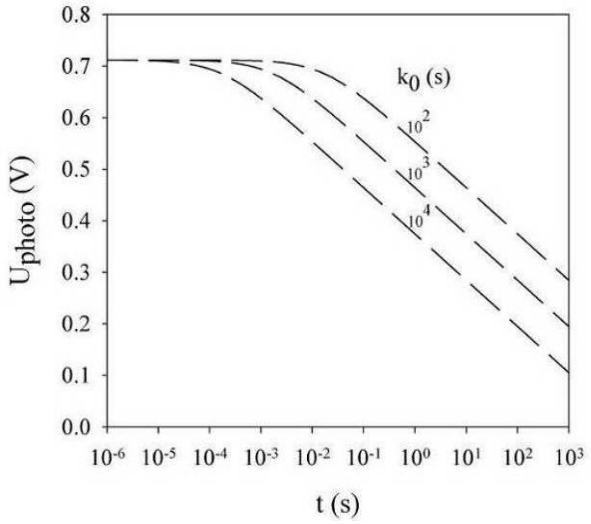

Figure 77 Photovoltage decay plots calculated from the quasistatic approach with variation in the electron recombination constant k_0. $N_C=10^{21}$ cm^{-3}, E_C-$E_{F,redox}$=1.0 eV, T=298K, T_C=800K, $U_{photo}(0)$=0.712V, $N_t=10^{18}$cm^{-3}.

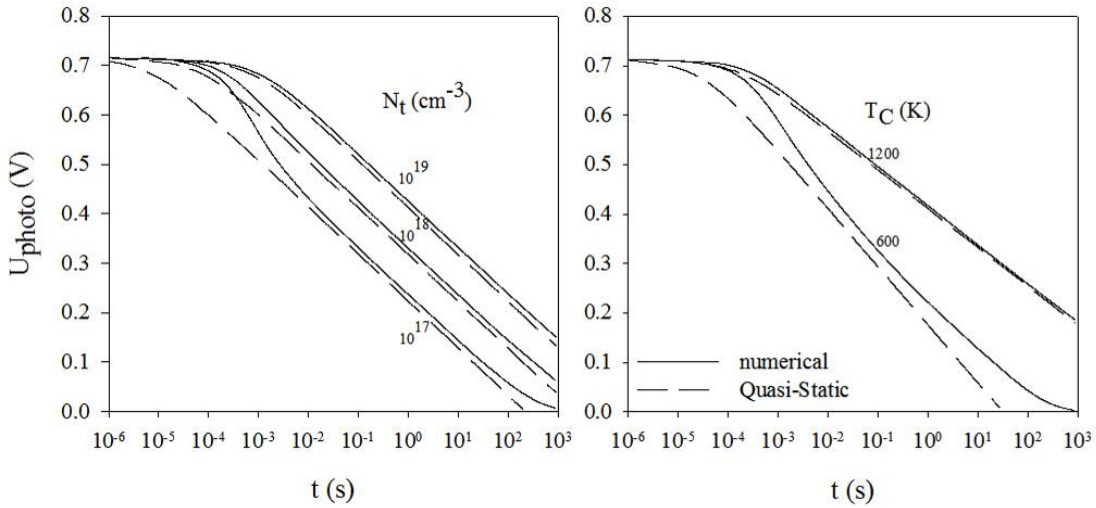

Figure 78 Photovoltage decay plots comparing full numerical calculations and quasi-static approximation. For the numerical calculations D_0=0.4 cm^2s^{-1}, k_t=10^9s^{-1} and k_0=10^4s^{-1}. The parameters in common with the two methods are the same as in Figure 77. Left: Trap density N_t varied. Right: Characteristic temperature T_C varied.

The plots in Figure 78 compare the results of the numerical calculation with the quasi-static model in order to establish the regimes in which the quasi-static approximation is suitable for analysing photovoltage decays.

Firstly, when the trap density is reduced to a density similar to the conduction band electron density at open-circuit ($10^{17}cm^{-3}$), the quasistatic assumption is violated. Secondly, reducing the value of T_C to such an extent has the effect of placing a greater fraction of traps near the conduction band edge, resulting in the number of traps that are filled being equivalent to the conduction band electron density, again violating the quasi-static assumption.

The full numerical solutions show that the initial plateau in the photovoltage decay is always restricted to the timescale of the electron lifetime. Thus, the timescale of this initial segment can be used to estimate the electron lifetime. At intermediate timescales, the two approaches tend to agree, showing that the quasi-static condition is held. At longer timescales, the two solutions diverge because the quasi-static approach assumes that the conduction band density of electrons is always far greater that the equilibrium value, $n_C << n_{C,eq}$. This is clearly not the case when $U_{photo}(t)$ approaches zero.

Provided that the cell parameters are in a suitable range, the quasi-static approach can be utilised to analyse the photovoltage decays to determine independently the characteristic trap distribution temperature (T_C) and the electron lifetime (τ_0). Again, values of N_C and E_C-$E_{F,redox}$ are required to obtain τ_0.

8.2 Determination of the Activation Energy of the Back Reaction Rate Employing a Quasi-Static Approach

The activation energy of the rate constant for back reaction of conduction band electrons to the electrolyte was, using the quasi-static formulation, determined by fitting the photovoltage decay transients of an optimised cells for various temperatures.

$$k_0 = A\exp\left(E_A / k_B T\right) \qquad 104$$

The Arrhenius equation above relates the constant activation energy, temperature and reaction rate constant. Figure 54 already illustrated how the photovoltage decay transients varied according to a range of temperatures. For this analysis a cell with an almost ideal open-circuit voltage characteristic (62mV per decade of illumination) was used (see Figure 59), making the quasi-static approach valid.

The trap distribution for the cell is required for fitting and was determined directly by PV decay charge extraction.

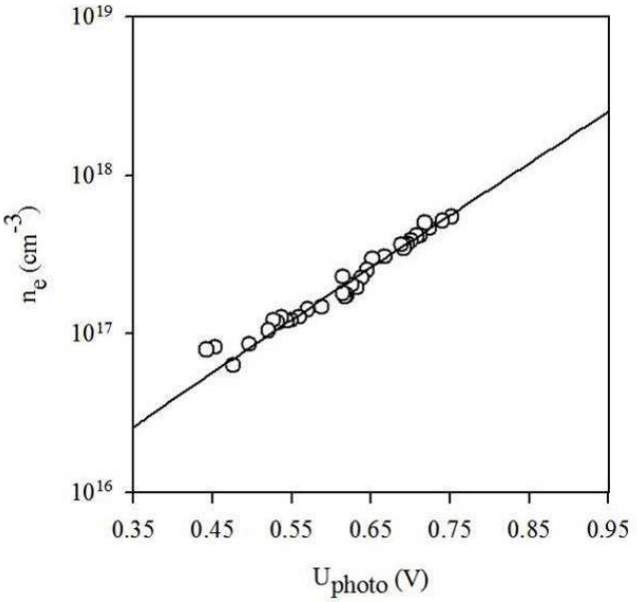

Figure 79 Charge extraction data for cell used in photovoltage decay analysis. Fitting using the characteristic temperature T_C=1500 and N_t=3x10^{18} cm^{-3} if E_C-$E_{F,redox}$=0.95eV is assumed.

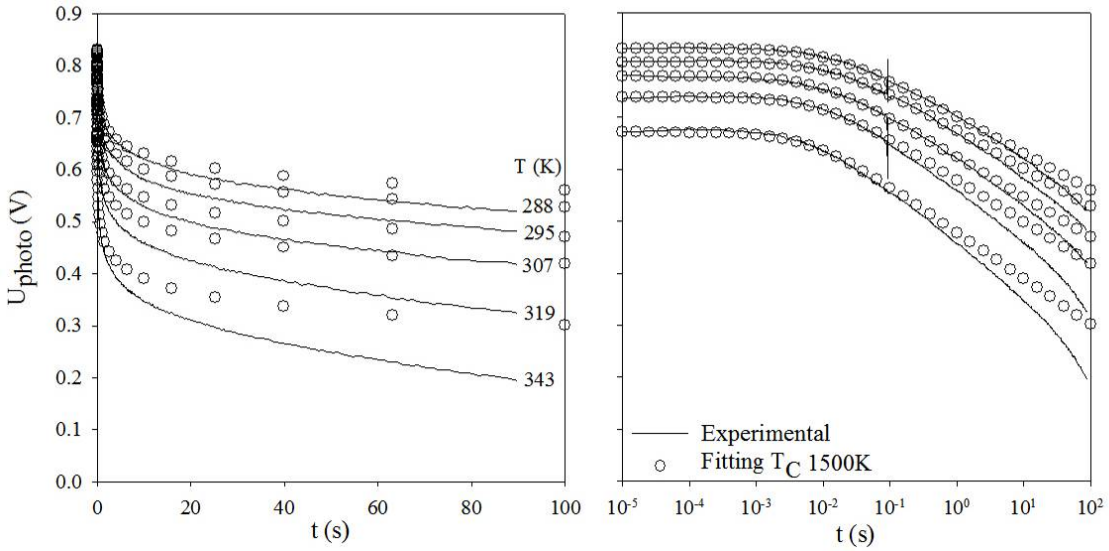

Figure 80 Photovoltage decays and fitting according to equations 100, 101 and 102. Parameters were; T_C=1500K, N_t=3x10^{18}, E_C-$E_{f,Fedox}$=0.95eV, $N_{C,295K}$=10^{19}cm^{-3}, N_C=$(N_{C,295K})^{3/2}$. Two scales, linear-linear and linear-log are used to better illustrate the different regions of the photovoltage decays.

The value of T_C measured from the charge extraction experiment did not yield convincing fits at long time scales t>0.1s. It is important to note that the value of T_C does not strongly affect the initial part of the photovoltage transients but more so the long timescale rate of decay. The values of k_0 were adjusted to best fit the inflection point of the transients.

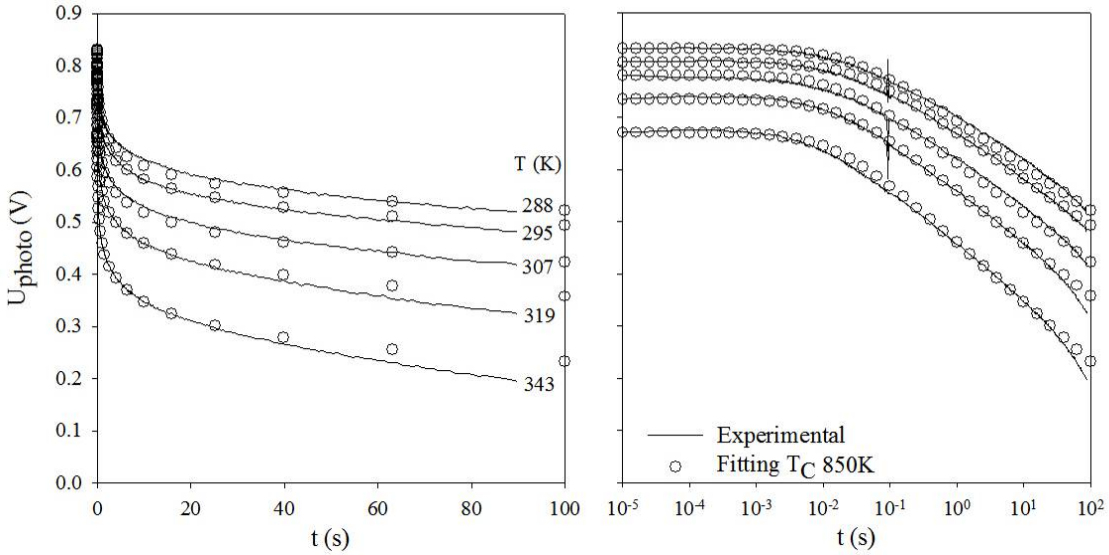

Figure 81 Photovoltage decay data fitted using the same parameters as in Figure 80 except T_C=850K.

A different value of T_C=850K was used to obtain a more optimal fit over the whole timescale even though contradicting the charge extraction data. This again highlights the contradictory values obtained from PV charge extraction and lifetime techniques (PV decay and IMVS). The initial and final photovoltage transients at room temperature (295K) were slightly different at

long timescales suggesting an irreversible change in the cell characteristics as its temperature was changed (see Figure 82).

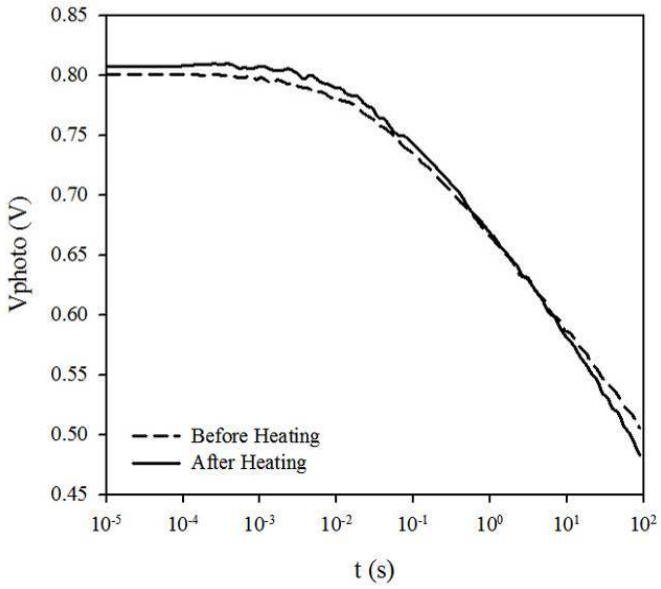

Figure 82 Photovoltage decay transients before and after heating to 70C/343K.

Firstly, stress due to thermal expansion may have introduced fissures in the blocking layer, resulting in an increase in the back reaction via the substrate. This effect appears to amplify as the temperature is increased. Secondly, heating could affect the balance of adsorbed species onto the surface of the TiO_2 particles, modifying the properties of the TiO_2 electrolyte interface. Unfortunately, the heating of the cell degraded the sealing, preventing further analysis.

Another method of displaying the relevant information extracted from the photovoltage decay transients is to transform it into lifetime data (see Figure 83). In essence, the analysis is identical and the values used for fitting were similar. Again from Figure 83, the fitting when using T_C=850K appears to be in better agreement over the whole scale. Plotting the data in terms of lifetimes does set an upper limit on the value of the electron lifetime, as the apparent electron lifetimes must always be longer than the conduction band lifetimes.

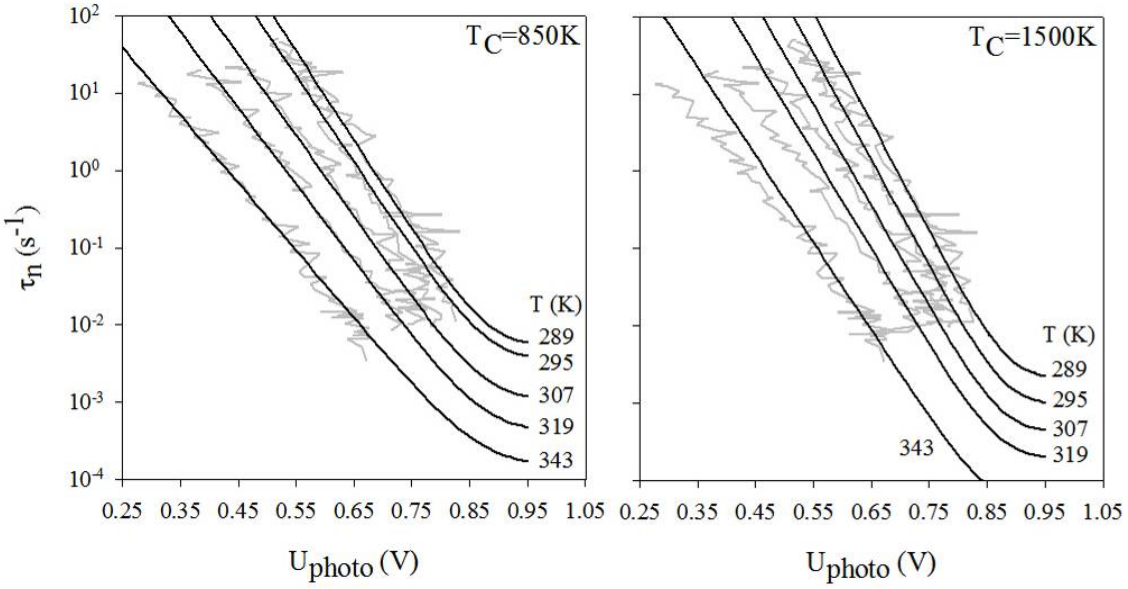

Figure 83 Photovoltage decay data transformed to lifetime data. Fitting in this case was carried out by using the relationship between electron lifetime and apparent electron lifetimes (equation 62) with $N_C=10^{19}x(T/295)^{3/2}$, $E_C-E_{F,redox}=0.95$eV, $T_C=850$K and $T_C=1500$K.

The fitting of the PV decays and the equivalent apparent lifetimes, using the two different characteristic temperatures, yielded information on how k_0 varied with temperature, i.e. an Arrhenius relationship. Figure 84 illustrates how the k_0 varied, and Table 8.2-1 summarizes the information when the Arrhenius equation is fitted accordingly.

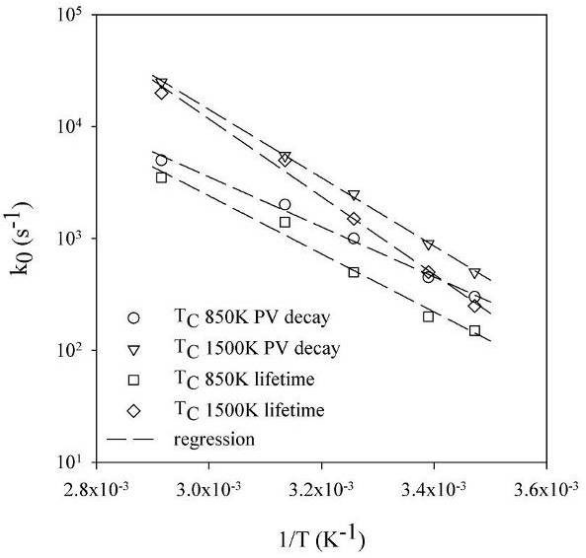

Figure 84 Rate constant (k_0) obtained from fitting the photovoltage decay and lifetime data. The resultant activation energies and pre-exponential factors are listed in the table below.

Table 8.2-1

Data analyses type	T_C	E_A (eV)	A (s^{-1})	A_{min} (s^{-1})	A_{max} (s^{-1})
PV decay	850K	0.44 +/- 4.5%	$9.7x10^9$	$4.7x10^9$	$2.0x10^{10}$
PV decay	1500K	0.60 +/- 1.6%	$1.9x10^{13}$	$1.4x10^{13}$	$2.7x10^{13}$
lifetime	850K	0.51 +/- 4.5%	$2.7x10^{11}$	$4.6x10^{10}$	$8.4x10^{11}$
lifetime	1500K	0.69 +/- 4.5%	$3.9x10^{14}$	$1.2x10^{14}$	$1.3x10^{15}$

There is considerable uncertainty in the values of A and E_A. However, it is still useful to use the values to calculate the photovoltage as a function of temperature to compare with the measured open-circuit photovoltages.

Thus far, the photovoltage decay transients and the lifetime plots have been fitted according to the quasi-static formulation. Flexibility of T_C was allowed, with two values used. One value corresponded to that obtained by PV decay charge extraction, and the other resulted in a better fitting to the PV decay transients and lifetime plots. From the fitting τ_0 was inferred and plotted as a function of temperature, allowing for the E_A and A to be calculated. Knowing these, the open-circuit voltage was calculated and compared to experiment. The most accurate calculations for the open-circuit photovoltage, were those obtained by fitting the PV decay transients whilst using the T_C value obtained by PV charge extraction.

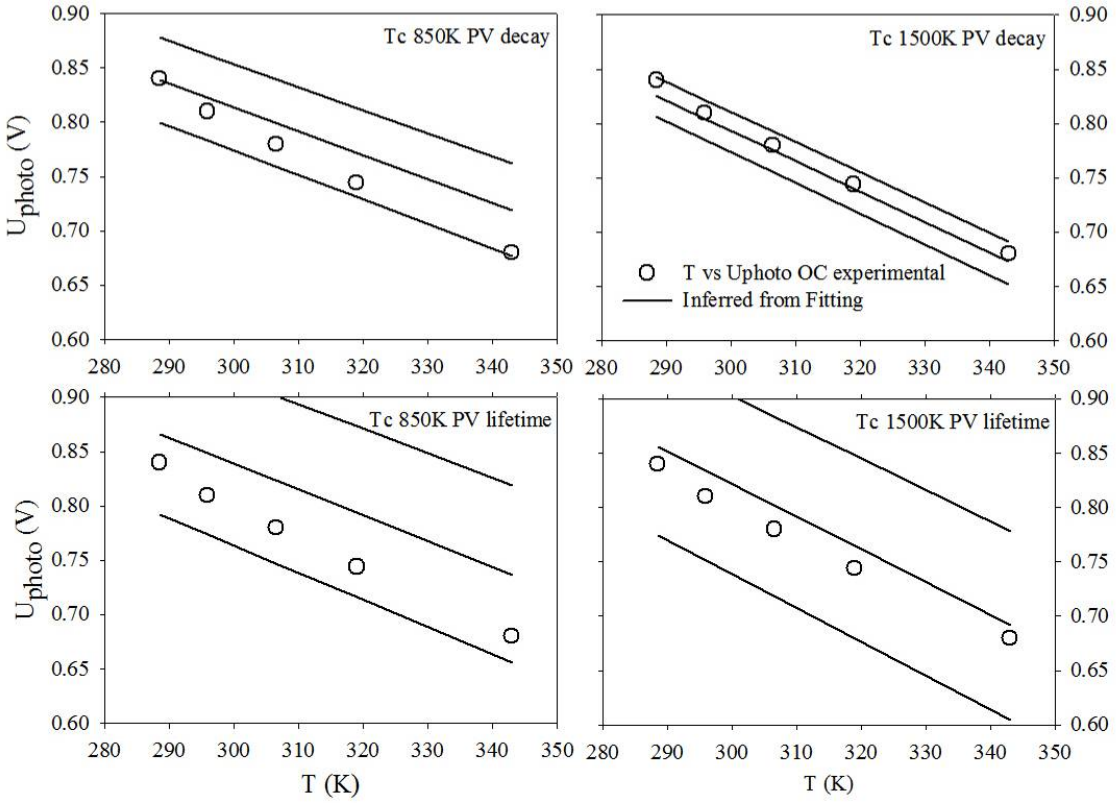

Figure 85 Open-circuit voltage calculated using equation 81 using E_A and A resultant from the fitting shown in Figure 84. Parameters remain equal with the absorbed photon number being $I_0=10^{16}cm^2s^{-1}$, d=5μm. The maximum and minimum calculated photovoltage values were calculated taking the uncertainties in the pre-exponential factor and activation energy in Table 8.2-1.

The value of conduction band density of states (N_C) used so far is low, $10^{19}cm^{-3}$. If N_C is increased by an order of magnitude, k_0 must be reduced by an order of magnitude resulting in conduction band electron lifetimes (τ_0) longer than the measured apparent values (τ_n) which is not possible. To obtain sensible

fits with a higher N_C requires larger values for E_C-$E_{F,redox}$. As always when the value of N_C is increased by an order of magnitude, the conduction band edge must increase by 59meV (at 298K) to maintain identical fits. Moving the conduction band edge requires the total number of traps between E_C and $E_{F,redox}$ to alter. For example, with T_C=850K the total number of total traps would increase 10 fold for every 168meV. The upward change in the conduction band edge is limited by the requirement that the LUMO level of the dye be above the conduction band edge to allow for efficient dye injection.

Figure 86 demonstrates the three variations one can permit when fitting the photovoltage decays to give rise to Arrhenius plots. These are the variation of the position of conduction band edge E_C-$E_{F,redox}$, the density of states N_C, and both at the same time.

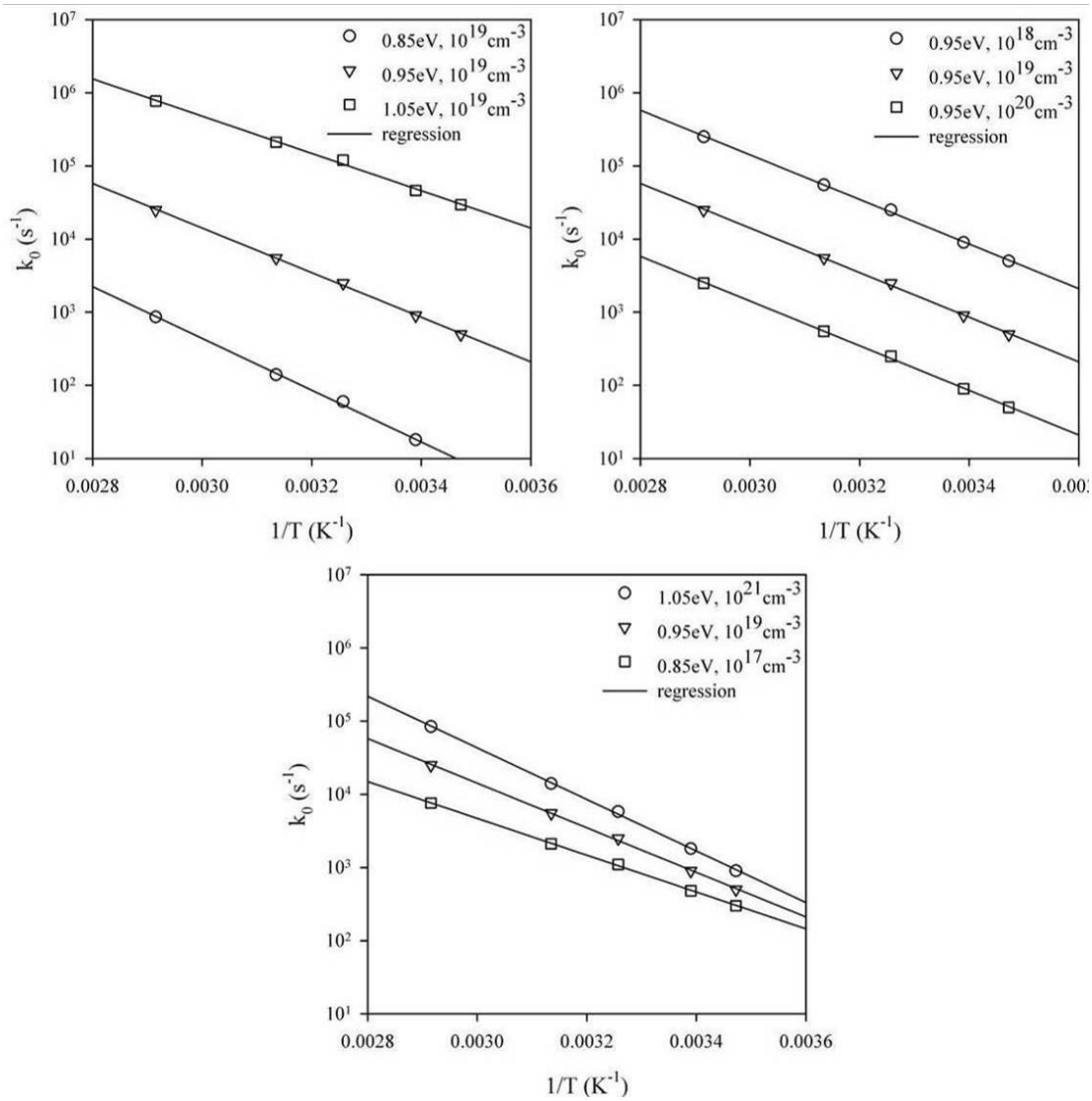

Figure 86 Resultant Arrhenius plots by fitting the PV decay transients varying E_C-$E_{F,redox}$ and N_C as shown. Total trap number N_t was adjusted according to the position of E_C. T_C=1500K, that measured by PV charge extraction. The resultant values for E_A and A are summarized in Table 8.2-2.

Table 8.2-2

Variation			Inferred Values from Fitting				
E_C-$E_{F,redox}$ (eV)	N_t (cm^{-3})	N_C (cm^{-3})	A_{min} (s^{-1})	A (s^{-1})	A_{max} (s^{-1})	E_A (eV)	E_A error %
E_C-$E_{F,redox}$ varied							
0.85	$1.4x10^{18}$	10^{19}	$1.0x10^{13}$	$1.8x10^{13}$	$3.0x10^{13}$	0.70	2.0
0.95	$3x10^{18}$	``	$1.4x10^{13}$	$2.0x10^{13}$	$2.9x10^{13}$	0.61	1.6
1.05	$6.8x10^{18}$	``	$1.1x10^{13}$	$2.1x10^{13}$	$3.9x10^{13}$	0.51	3.2
N_C varied							
0.95	$3x10^{18}$	10^{18}	$1.5\ x10^{14}$	$2.1\ x10^{14}$	$3.1\ x10^{14}$	0.61	1.6
``	``	10^{19}	$1.4\ x10^{13}$	$2.0\ x10^{13}$	$2.8\ x10^{13}$	0.61	1.6
``	``	10^{20}	$1.4\ x10^{12}$	$2.0\ x10^{12}$	$2.8\ x10^{12}$	0.61	1.6
E_C-$E_{F,redox}$ and N_C varied							
0.85	$1.4x10^{18}$	10^{17}	$1.0x10^{15}$	$1.6x10^{15}$	$2.4\ x10^{15}$	0.70	1.6
0.95	$3x10^{18}$	10^{19}	$1.3x10^{13}$	$1.9\ x10^{13}$	$2.8\ x10^{13}$	0.61	1.6
1.05	$6.8x10^{18}$	10^{21}	$1.3x10^{11}$	$1.7\ x10^{11}$	$2.1\ x10^{11}$	0.50	1.2

When only E_C-$E_{F,redox}$ is increased, the inferred values for k_0 increases. This results in a decrease in E_A increase whilst A remains essentially unchanged. There is, however, a limit as to how much E_C can shift, because electron injection from the dye to the conduction band has to remain favourable. When N_C is increased, E_A remains unchanged but A decreases by the same magnitude. If both E_C-$E_{F,redox}$ and N_C are increased at the same time, a more realistic value of N_C is possible with a larger E_C-$E_{F,redox}$, with $N_C=10^{21}cm^{-3}$ and E_C-$E_{F,redox}$=1.05eV. This still results in lifetimes which are compatible with the apparent ones measured. Although the values of E_A and A change, the calculated photovoltage as a function of temperature remains unchanged.

Further analysis requires either N_C or E_F-$E_{F,redox}$ to be defined and thus comparison of the values of E_A and A for the cells resulting of the two different colloids is difficult. However, it does appear that the kinetics governing the back reaction of electrons from the conduction band to the I_3^- species can be described by the Arrhenius equation. The back reaction rate varies by two orders of magnitude over the temperature range used, which is significant and comparable to that speculated in section 7.8 when measuring the temperature dependence of the shirt-circuit internal QFL and the open-circuit photovoltage.

9 Discussion and Conclusions

Two theoretical formulations to describe electron transport in a DSC were tested, the diffusion case for steady-state conditions, and the quasi-static condition to describe time resolved dynamic measurements.

Because of the relatively low diffusion coefficient of electrons in TiO_2, the solutions to the continuity equation suggest a large density of free electrons within the TiO_2, translating into a measurable internal QFL under illumination. Indirect evidence of the magnitude of the internal QFL was already present in the literature. However, the solutions to the continuity equation also allow the electron density profile to be described as a function of applied bias, (i.e. along the iV curve).

To be able to measure the QFL within the TiO_2, a secondary sensing electrode was devised. This was achieved by evaporating a thin film of Ti on top of the TiO_2, to then measure the QFL at the extremity of the TiO_2 film. Several steps were taken to optimise the electrode to ensure reliable results. However, some effects remained un-explained, such as the anomaly observed in the intensity dependence of the QFL measured under open-circuit conditions. More work is required to understand the behaviour of the Ti electrode as an intruding body, by varying such things as the nature of the nanoporous TiO_2 or how the Ti film is deposited.

Initial tests on the behaviour of the measured internal QFL showed that when a compact underlying TiO_2 blocking layer was not incorporated, the QFL decay profile under open-circuit conditions is spatially inhomogeneous. This further confirmed the importance of quenching electron recombination via the substrate when certain characteristics of DSC are to be investigated.

With the successful incorporation of a secondary sensing electrode within the TiO_2, the internal QFL could be measured under a variety of conditions. The first of these was how the internal QFL varied as a function of applied bias. This was shown to behave as expected when diffusive electron transport is assumed and the electron diffusion length is greater than the film thickness (L_n>3d). In other words, because of the relatively low electron diffusion coefficient in TiO_2, there is a large free electron density within the film and a large gradient close to the collecting substrate (FTO).

However, when the measured values were fitted according to theory, diffusion lengths over two orders in magnitude greater than the film thickness were

inferred. If this were true, much thicker films could be prepared to improve light harvesting and hence current densities. However, a flaw or incompleteness in the theory was highlighted, which is the non-ideal nature of the electron lifetime. This is most evident when the QFL is measured at open-circuit as a function of light intensity. A maximum value for the conduction band electron lifetime was determined by measuring the apparent electron lifetimes. According to the quasi-static formulation, the apparent electron lifetimes will always be greater than the conduction band electron lifetime. However, it was found that shorter apparent electron lifetimes were measured than the conduction band lifetimes inferred from fitting the QFLs. This being the case, the inferred conduction band electron lifetimes are erroneous and should in fact be shorter, suggesting that the electron diffusion length is actually shorter. The electron lifetimes could, in fact, vary significantly if dependent on the electron density. According to the calculations, the conduction band electron density varies over four orders of magnitude from short-circuit to open-circuit conditions. If electron recombination occurs additionally via a fixed number of surface states, these would be more predominant at low electron densities, where the ratio of surface recombination states to free electrons is greater. Thus, it is feasible that the electron lifetime varies according to the electron density, decreasing as the electron density decreases.

This problem or shortcoming of the theory was always kept in mind. The reason it was not dealt with theoretically is that firstly, it would add further unknowns, and secondly, it is possible to prepare DSCs having almost ideal open-circuit photovoltage intensity dependence, synonymous of an ideal electron lifetime characteristic. Unfortunately, these were not further explored by employing the secondary sensing electrode. Until the ideality of the intensity dependence of the open-circuit QFL can be controlled, there is little reason to formulate the behaviour of surface recombination states and, hence, the non-ideal behaviour of the electron lifetime. However, it could prove invaluable to the understanding of DSCs, to be able to control this behaviour experimentally and subsequently formulate it theoretically. This will probably follow from different colloid preparation techniques and surface modifications by additives to the electrolyte.

Having already made use of the quasi-static formulation and dynamic measurements to determine a maximum value for the conduction band electron lifetime, an attempt was made to test the diffusion model and the

trapping model together, by simultaneous measuring the QFL and the trapped electron density along the iV curve. The general trends found were as expected, where the trapped electron density varied according to the QFL. Importantly, this stringent test brought together two separate effects observed in a DSC, diffusion driven transport and the high trap density.

The open-circuit and short-circuit temperature dependence of the QFL was measured and compared to theory. For the open-circuit conditions, simple expressions were derived and general trends were shown that could be explained by an Arrhenius-type first order reaction for electron back reaction with the triiodide. That is, at higher temperatures, lower voltages were measured because of the increased back reaction rate, reducing the conduction band electron density. For short-circuit conditions, it was shown that the dominant factor determining the QFL is the k_BT term, as expected by the solutions of the continuity equation. The relationship was, however, not ideal, with lower than predicted QFL values measured at higher temperatures and low intensities. This was attributed to either a shift in the conduction band edge or decrease in the electron diffusion length, because of the possible strong temperature dependence of the electron lifetime. The current density temperature dependence suggested a decrease in electron collection efficiency, possibly due to a decrease in the electron lifetime. The strong temperature dependence for the electron recombination rate was then observed directly using an ideally behaving cell and employing the quasi-static formulation. It would certainly be interesting to observe this type of behaviour employing different concentration of species in the electrolyte to better elucidate the kinetics and energetics involved in the back reaction of electrons.

The quasi-static formulation was tested against a full numerical solution and shown to be valid for a parameter phase space typical of DSCs. The quasi-static formulation was then successfully shown to describe the open-circuit photovoltage decay profile of a DSC with almost ideally behaving cell. With this, it was then possible to measure open-circuit photovoltage decays at various temperatures, fit them accordingly, and infer how the back reaction rate (and hence lifetime) varied with temperature. Again, it was found that the back reaction rate followed an Arrhenius relationship. The calculated pre-exponential and activation values from the Arrhenius plots were then used to successfully predict the measured open-circuit photovoltage of the cells.

The choice of materials presented in this thesis were based on those that are commercially available. One hopes that this leads to more reproducibility and

thus comparability in the literature.

Great flexibility was always possible when fitting data because of the uncertainty of parameters. Independent means have to be developed to obtain more values to describe the electronic band structure of the oxides used in DSCs, namely the density of states and the electron mobility. Also, the interaction of the adsorption of the dyes and contacting with the electrolyte have to be further investigated to better pin down the position of different energy levels, e.g. the difference between the conduction band edge and the redox potential of the electrolyte.

One way to obtain a better handle of the unknown parameters is by further comparison of numerical modelling with experiment. One possibility is the modelling of photocurrent transients by full geometrical representations of the TiO_2 porous structure, using Monte Carlo simulation [140]. These explicitly allows for the different spatial and energetic trap distributions as well as for the TiO_2 structure. With the incorporation of the secondary sensing electrode, further dynamic measurements could be performed to also measure the temporal behaviour of the internal quasi-Fermi level and compared to full numerical solutions.

With all this in mind, it appears fundamental that to further understand the DSC, more ideally behaving cells have to be prepared and then characterised using the wide range of available techniques, some of which were recently developed and described here.

10 References

1. M. Bailes, P.J. Cameron, K. Lobato and L.M. Peter, *Determination of the density and energetic distribution of electron traps in dye-sensitized nanocrystalline solar cells.* Journal of Physical Chemistry B, 2005. 109(32): p. 15429.

2. K. Lobato, L.M. Peter and U. Würfel, *Direct measurement of the internal electron quasi-fermi level in dye sensitized solar cells using a titanium secondary electrode.* Journal of Physical Chemistry B, 2006. 110(33): p. 16201.

3. K. Lobato and L.M. Peter, *Direct measurement of the temperature coefficient of the electron quasi-Fermi level in dye-sensitized nanocrystalline solar cells using a titanium sensor electrode.* Journal of Physical Chemistry B, 2006. 110(43): p. 21920.

4. A.B. Walker, L.M. Peter, K. Lobato and P.J. Cameron, *Analysis of photovoltage decay transients in dye-sensitized solar cells.* Journal of Physical Chemistry B, 2006. 110(50): p. 25504.

5. D.M. Chapin, C.S. Fuller and G.L. Pearson, *A New Silicon p-n Junction Photocell for Converting Solar Radiation into Electrical Power.* Journal of Applied Physics, 1954. 25(5): p. 676.

6. W. Shockley and H.J. Queisser, *Detailed Balance Limit of Efficiency of P-N Junction Solar Cells.* Journal of Applied Physics, 1961. 32(3): p. 510.

7. E. Cartlidge, *Bright outlook for solar cells*, in *Physics World.* 2007: London.

8. M.A. Green, *Crystalline and thin-film silicon solar cells: state of the art and future potential.* Solar Energy, 2003. 74(3): p. 181.

9. W. Schmidt, B. Woesten and J.P. Kalejs, *Manufacturing technology for ribbon silicon (EFG) wafers and solar cells.* Progress in Photovoltaics, 2002. 10(2): p. 129.

10. R.W. Birkmire and E. Eser, *Polycrystalline thin film solar cells: Present status and future potential.* Annual Review of Materials Science, 1997. 27: p. 625.

11. L.L. Kazmerski, F.R. White and G.K. Morgan, *Thin-Film $CulnSe_2$-Cds Heterojunction Solar-Cells.* Applied Physics Letters, 1976. 29(4): p. 268.

12. D.A. Cusano, *CdTe solar cells and photovoltaic heterojunctions in II-VI compounds.* Solid-State Electronics, 1963. 6(3): p. 217.

13. R.R. King, D.C. Law, K.M. Edmondson, C.M. Fetzer, G.S. Kinsey, H. Yoon, R.A. Sherif and N.H. Karam, *40% efficient metamorphic GaInP/GaInAs/Ge multijunction solar cells.* Applied Physics Letters, 2007. 90(18).

14. V.M. Lantratov, N.A. Kalyuzhnyi, S.A. Mintairov, N.K. Timoshina, M.Z. Shvarts and V.M. Andreev, *High-efficiency dual-junction GaInP/GaAs tandem solar cells obtained by the method of MOCVD.* Semiconductors, 2007. 41(6): p. 727.

15. A. Luque, A. Marti and A.J. Nozik, *Solar cells based on quantum dots: Multiple exciton generation and intermediate bands.* Mrs Bulletin, 2007. 32(3): p. 236.

16. T.L. Benanti and D. Venkataraman, *Organic solar cells: An overview focusing on active layer morphology.* Photosynthesis Research, 2006. 87(1): p. 73.

17. B. O'Regan and M. Grätzel, *Low-cost, high-efficiency solar cell based on dye-sensitized colloidal TiO_2 films.* Nature, 1991. 353(6346): p. 737.

18. Y. Chiba, A. Islam, Y. Watanabe, R. Komiya, N. Koide and L.Y. Han, *Dye-sensitized solar cells with conversion efficiency of 11.1%.* Japanese Journal of Applied Physics Part 2-Letters & Express Letters, 2006. 45(24-28): p. L638.

19. P. Würfel, *Physics of Solar Cells*. 1st ed. 2005, Weinheim: Wiley-VCH.

20. M. Grätzel, *Conversion of sunlight to electric power by nanocrystalline dye-sensitized solar cells.* Journal of Photochemistry and Photobiology a-Chemistry, 2004. 164(1-3): p. 3.

21. M.K. Nazeeruddin, A. Kay, I. Rodicio, R. Humphrybaker, E. Muller, P. Liska, N. Vlachopoulos and M. Gratzel, *Conversion of Light to Electricity by Cis-X2bis(2,2'-Bipyridyl-4,4'-Dicarboxylate)Ruthenium(II) Charge-Transfer Sensitizers (X = Cl-, Br-, I-, Cn-, and Scn-) on Nanocrystalline TiO_2 Electrodes.* Journal of the American Chemical Society, 1993. 115(14): p. 6382.

22. M.K. Nazeeruddin, P. Pechy, T. Renouard, S.M. Zakeeruddin, R. Humphry-Baker, P. Comte, P. Liska, L. Cevey, E. Costa, V. Shklover, L. Spiccia, G.B. Deacon, C.A. Bignozzi and M. Gratzel, *Engineering of efficient panchromatic sensitizers for nanocrystalline TiO_2-based solar cells.* Journal of the American Chemical Society, 2001. 123(8): p. 1613.

23. P. Wang, S.M. Zakeeruddin, J.E. Moser, R. Humphry-Baker, P. Comte, V. Aranyos, A. Hagfeldt, M.K. Nazeeruddin and M. Gratzel, *Stable new sensitizer with improved light harvesting for nanocrystalline dye-sensitized solar cells.* Advanced Materials, 2004. 16(20): p. 1806.

24. L. Schmidt-Mende, U. Bach, R. Humphry-Baker, T. Horiuchi, H. Miura, S. Ito, S. Uchida and M. Gratzel, *Organic dye for highly efficient solid-state dye-sensitized solar cells.* Advanced Materials, 2005. 17(7): p. 813.

25. T. Horiuchi, H. Miura, K. Sumioka and S. Uchida, *High efficiency of dye-sensitized solar cells based on metal-free indoline dyes.* Journal of the American Chemical Society, 2004. 126(39): p. 12218.

26. J. Kallioinen, G. Benko, V. Sundstrom, J.E.I. Korppi-Tommola and A.P. Yartsev, *Electron transfer from the singlet and triplet excited states of $Ru(dcbpy)_2(NCS)_2$ into nanocrystalline TiO_2 thin films.* Journal of Physical Chemistry B, 2002. 106(17): p. 4396.

27. Y. Tachibana, J.E. Moser, M. Gratzel, D.R. Klug and J.R. Durrant, *Subpicosecond interfacial charge separation in dye-sensitized nanocrystalline titanium dioxide films.* Journal of Physical Chemistry, 1996. 100(51): p. 20056.

28. Y. Tachibana, S.A. Haque, I.P. Mercer, J.E. Moser, D.R. Klug and J.R. Durrant, *Modulation of the rate of electron injection in dye-sensitized nanocrystalline TiO_2 films by externally applied bias.* Journal of Physical Chemistry B, 2001. 105(31): p. 7424.

29. T. Hannappel, B. Burfeindt, W. Storck and F. Willig, *Measurement of ultrafast photoinduced electron transfer from chemically anchored Ru-dye molecules into empty electronic states in a colloidal anatase TiO_2 film.* Journal of Physical Chemistry B, 1997. 101(35): p. 6799.

30. P. Wang, S.M. Zakeeruddin, R. Humphry-Baker and M. Gratzel, *A binary ionic liquid electrolyte to achieve >= 7% power conversion efficiencies in dye-sensitized solar cells.* Chemistry of Materials, 2004. 16(14): p. 2694.

31. P. Wang, S.M. Zakeeruddin, J.E. Moser, M.K. Nazeeruddin, T. Sekiguchi and M. Gratzel, *A stable quasi-solid-state dye-sensitized solar cell with an amphiphilic ruthenium sensitizer and polymer gel electrolyte.* Nature Materials, 2003. 2(6): p. 402.

32. P. Wang, C. Klein, R. Humphry-Baker, S.M. Zakeeruddin and M. Gratzel, *A high molar extinction coefficient sensitizer for stable dye-sensitized solar cells.* Journal of the American Chemical Society, 2005. 127(3): p. 808.

33. S.A. Haque, E. Palomares, B.M. Cho, A.N.M. Green, N. Hirata, D.R. Klug and J.R. Durrant, *Charge separation versus recombination in dye-sensitized nanocrystalline solar cells: the minimization of kinetic redundancy.* Journal of the American Chemical Society, 2005. 127(10): p. 3456.

34. A. Hagfeldt and M. Gratzel, *Molecular photovoltaics.* Accounts of Chemical Research, 2000. 33(5): p. 269.

35. A.C. Fisher, L.M. Peter, E.A. Ponomarev, A.B. Walker and K.G.U. Wijayantha, *Intensity dependence of the back reaction and transport of electrons in dye-sensitized nanacrystalline TiO_2 solar cells.* Journal of Physical Chemistry B, 2000. 104(5): p. 949.

36. G. Schlichthorl, S.Y. Huang, J. Sprague and A.J. Frank, *Band edge movement and recombination kinetics in dye-sensitized nanocrystalline TiO_2 solar cells: A study by intensity modulated photovoltage spectroscopy.* Journal of Physical Chemistry B, 1997. 101(41): p. 8141.

37. S.Y. Huang, G. Schlichthorl, A.J. Nozik, M. Gratzel and A.J. Frank, *Charge recombination in dye-sensitized nanocrystalline TiO_2 solar cells.* Journal of Physical Chemistry B, 1997. 101(14): p. 2576.

38. P.J. Cameron and L.M. Peter, *Characterization of titanium dioxide blocking layers in dye-sensitized nanocrystalline solar cells.* Journal of Physical Chemistry B, 2003. 107(51): p. 14394.

39. K. Schwarzburg and F. Willig, *Origin of photovoltage and photocurrent in the nanoporous dye-sensitized electrochemical solar cell.* Journal of Physical Chemistry B, 1999. 103(28): p. 5743.

40. G. Oskam, B.V. Bergeron, G.J. Meyer and P.C. Searson, *Pseudohalogens for dye-sensitized TiO_2 photoelectrochemical cells.* Journal of Physical Chemistry B, 2001. 105(29): p. 6867.

41. B.V. Bergeron, A. Marton, G. Oskam and G.J. Meyer, *Dye-sensitized SnO_2 electrodes with iodide and pseudohalide redox mediators.* Journal of Physical Chemistry B, 2005. 109(2): p. 937.

42. P.J. Cameron, L.M. Peter, S.M. Zakeeruddin and M. Gratzel, *Electrochemical studies of the Co(III)/ Co(II)(dbbip)$_2$ redox couple as a mediator for dye-sensitized nanocrystalline solar cells.* Coordination Chemistry Reviews, 2004. 248(13-14): p. 1447.

43. U. Bach, D. Lupo, P. Comte, J.E. Moser, F. Weissortel, J. Salbeck, H. Spreitzer and M. Gratzel, *Solid-state dye-sensitized mesoporous TiO_2 solar cells with high photon-to-electron conversion efficiencies.* Nature, 1998. 395(6702): p. 583.

44. B.A. Gregg, F. Pichot, S. Ferrere and C.L. Fields, *Interfacial recombination processes in dye-sensitized solar cells and methods to passivate the interfaces.* Journal of Physical Chemistry B, 2001. 105(7): p. 1422.

45. R.M. Penner, M.J. Heben, T.L. Longin and N.S. Lewis, *Fabrication and Use of Nanometer-Sized Electrodes in Electrochemistry.* Science, 1990. 250(4984): p. 1118.

46. J.F. Sun and D.M. Stanbury, *Kinetics and mechanism of the one-electron reduction of iodine by $[Ru^{II}(NH_3)_5isn]^{2+}$ in aqueous solution.* Inorganic Chemistry, 1998. 37(6): p. 1257.

47. B. O'Regan, F. Lenzmann, R. Muis and J. Wienke, *A solid-state dye-sensitized solar cell fabricated with pressure-treated P25-TiO_2 and CuSCN: Analysis of pore filling and IV characteristics.* Chemistry of Materials, 2002. 14(12): p. 5023.

48. K. Tennakone, G. Kumara, I.R.M. Kottegoda, K.G.U. Wijayantha and V.P.S. Perera, *A solid-state photovoltaic cell sensitized with a ruthenium bipyridyl complex.* Journal of Physics D-Applied Physics, 1998. 31(12): p. 1492.

49. A.F. Nogueira, J.R. Durrant and M.A. De Paoli, *Dye-sensitized nanocrystalline solar cells employing a polymer electrolyte.* Advanced Materials, 2001. 13(11): p. 826.

50. F. Cao, G. Oskam and P.C. Searson, *A Solid-State, Dye-Sensitized Photoelectrochemical Cell.* Journal of Physical Chemistry, 1995. 99(47): p. 17071.

51. W. Kubo, T. Kitamura, K. Hanabusa, Y. Wada and S. Yanagida, *Quasi-solid-state dye-sensitized solar cells using room temperature molten salts and a low molecular weight gelator.* Chemical Communications, 2002(4): p. 374.

52. P. Wang, S.M. Zakeeruddin, I. Exnar and M. Gratzel, *High efficiency dye-sensitized nanocrystalline solar cells based on ionic liquid polymer gel electrolyte.* Chemical Communications, 2002(24): p. 2972.

53. J.M. Tarascon and M. Armand, *Issues and challenges facing rechargeable lithium batteries.* Nature, 2001. 414(6861): p. 359.

54. Y. Saito, T. Kitamura, Y. Wada and S. Yanagida, *Application of poly(3,4-ethylenedioxythiophene) to counter electrode in dye-sensitized solar cells.* Chemistry Letters, 2002(10): p. 1060.

55. L.M. Peter, *Transport, trapping and interfacial transfer of electrons in dye-sensitized nanocrystalline solar cells.* Journal of Electroanalytical Chemistry, 2007. 599(2): p. 233.

56. A. Hauch and A. Georg, *Diffusion in the electrolyte and charge-transfer reaction at the platinum electrode in dye-sensitized solar cells.* Electrochimica Acta, 2001. 46(22): p. 3457.

57. A. Kay and M. Gratzel, *Low cost photovoltaic modules based on dye sensitized nanocrystalline titanium dioxide and carbon powder.* Solar Energy Materials and Solar Cells, 1996. 44(1): p. 99.

58. P.J. Cameron and L.M. Peter, *How does back-reaction at the conducting glass substrate influence the dynamic photovoltage response of nanocrystalline dye-sensitized solar cells?* Journal of Physical Chemistry B, 2005. 109(15): p. 7392.

59. P.J. Cameron, L.M. Peter and S. Hore, *How important is the back reaction of electrons via the substrate in dye-sensitized nanocrystalline solar cells?* Journal of Physical Chemistry B, 2005. 109(2): p. 930.

60. L.Y. Han, N. Koide, Y. Chiba, A. Islam, R. Komiya, N. Fuke, A. Fukui and R. Yamanaka, *Improvement of efficiency of dye-sensitized solar cells by reduction of internal resistance.* Applied Physics Letters, 2005. 86(21).

61. K. Hara, T. Horiguchi, T. Kinoshita, K. Sayama, H. Sugihara and H. Arakawa, *Highly efficient photon-to-electron conversion with mercurochrome-sensitized nanoporous oxide semiconductor solar cells.* Solar Energy Materials and Solar Cells, 2000. 64(2): p. 115.

62. S. Ito, T. Takeuchi, T. Katayama, M. Sugiyama, M. Matsuda, T. Kitamura, Y. Wada and S. Yanagida, *Conductive and transparent multilayer films for low-temperature-sintered mesoporous TiO_2 electrodes of dye-sensitized solar cells.* Chemistry of Materials, 2003. 15(14): p. 2824.

63. S. Nakade, M. Matsuda, S. Kambe, Y. Saito, T. Kitamura, T. Sakata, Y. Wada, H. Mori and S. Yanagida, *Dependence of TiO_2 nanoparticle preparation methods and annealing temperature on the efficiency of dye-sensitized solar cells.* Journal of Physical Chemistry B, 2002. 106(39): p. 10004.

64. M.A. De Paoli, A.F. Nogueira, D.A. Machado and C. Longo, *All-polymeric electrochromic and photoelectrochemical devices: new advances.* Electrochimica Acta, 2001. 46(26-27): p. 4243.

65. F. Pichot, J.R. Pitts and B.A. Gregg, *Low-temperature sintering of TiO_2 colloids: Application to flexible dye-sensitized solar cells.* Langmuir, 2000. 16(13): p. 5626.

66. C. Longo, J. Freitas and M.A. De Paoli, *Performance and stability of TiO_2/dye solar cells assembled with flexible electrodes and a polymer electrolyte.* Journal of Photochemistry and Photobiology a-Chemistry, 2003. 159(1): p. 33.

67. D.S. Zhang, T. Yoshida and H. Minoura, *Low temperature synthesis of porous nanocrystalline TiO_2 thick film for dye-sensitized solar cells by hydrothermal crystallization.* Chemistry Letters, 2002(9): p. 874.

68. D.S. Zhang, T. Yoshida and H. Minoura, *Low-temperature fabrication of efficient porous titania photoelectrodes by hydrothermal crystallization at the solid/gas interface.* Advanced Materials, 2003. 15(10): p. 814.

69. D.S. Zhang, T. Yoshida, K. Furuta and H. Minoura, *Hydrothermal preparation of porous nano-crystalline TiO_2 electrodes for flexible solar cells.* Journal of Photochemistry and Photobiology a-Chemistry, 2004. 164(1-3): p. 159.

70. T. Miyasaka, Y. Kijitori, T.N. Murakami, M. Kimura and S. Uegusa, *Efficient nonsintering type dye-sensitized photocells based on electrophoretically deposited TiO_2 layers.* Chemistry Letters, 2002(12): p. 1250.

71. T.N. Murakami, Y. Kijitori, N. Kawashima and T. Miyasaka, *UV light-assisted chemical vapour deposition of TiO_2 for efficiency development at dye-sensitized mesoporous layers on plastic film electrodes.* Chemistry Letters, 2003. 32(11): p. 1076.

72. T.N. Murakami, Y. Kijitori, N. Kawashima and T. Miyasaka, *Low temperature preparation of mesoporous TiO_2 films for efficient dye-sensitized photoelectrode by chemical vapour deposition combined with UV light irradiation.* Journal of Photochemistry and Photobiology a-Chemistry, 2004. 164(1-3): p. 187.

73. T. Kado, M. Yamaguchi, Y. Yamada and S. Hayase, *Low temperature preparation of nano-porous TiO_2 layers for plastic dye sensitized solar cells.* Chemistry Letters, 2003. 32(11): p. 1056.

74. H. Lindstrom, G. Boschloo, S.E. Lindquist and A. Hagfeldt, *A new method for manufacturing dye-sensitized solar cells on plastic substrates*, in *Molecules as Components of Electronic Devices*. 2003, American Chemical Society: Washington. p. 123.

75. H. Lindstrom, A. Holmberg, E. Magnusson, S.E. Lindquist, L. Malmqvist and A. Hagfeldt, *A new method for manufacturing nanostructured electrodes on plastic substrates.* Nano Letters, 2001. 1(2): p. 97.

76. H. Lindstrom, A. Holmberg, E. Magnusson, L. Malmqvist and A. Hagfeldt, *A new method to make dye-sensitized nanocrystalline solar cells at room temperature.* Journal of Photochemistry and Photobiology a-Chemistry, 2001. 145(1-2): p. 107.

77. H. Lindstrom, E. Magnusson, A. Holmberg, S. Sodergren, S.E. Lindquist and A. Hagfeldt, *A new method for manufacturing nanostructured electrodes on glass substrates.* Solar Energy Materials and Solar Cells, 2002. 73(1): p. 91.

78. S.A. Haque, E. Palomares, H.M. Upadhyaya, L. Otley, R.J. Potter, A.B. Holmes and J.R. Durrant, *Flexible dye sensitised nanocrystalline semiconductor solar cells.* Chemical Communications, 2003(24): p. 3008.

79. G.K. Mor, K. Shankar, M. Paulose, O.K. Varghese and C.A. Grimes, *Use of highly-ordered TiO_2 nanotube arrays in dye-sensitized solar cells.* Nano Letters, 2006. 6(2): p. 215.

80. G.K. Mor, O.K. Varghese, M. Paulose, K. Shankar and C.A. Grimes, *A review on highly ordered, vertically oriented TiO_2 nanotube arrays: Fabrication, material properties, and solar energy applications.* Solar Energy Materials and Solar Cells, 2006. 90(14): p. 2011.

81. M. Paulose, K. Shankar, O.K. Varghese, G.K. Mor and C.A. Grimes, *Application of highly-ordered TiO_2 nanotube-arrays in heterojunction dye-sensitized solar cells.* Journal of Physics D-Applied Physics, 2006. 39(12): p. 2498.

82. M. Paulose, K. Shankar, O.K. Varghese, G.K. Mor, B. Hardin and C.A. Grimes, *Backside illuminated dye-sensitized solar cells based on titania nanotube array electrodes.* Nanotechnology, 2006. 17(5): p. 1446.

83. K. Shankar, G.K. Mor, H.E. Prakasam, S. Yoriya, M. Paulose, O.K. Varghese and C.A. Grimes, *Highly-ordered TiO_2 nanotube arrays up to 220 μm in length: use in water photoelectrolysis and dye-sensitized solar cells.* Nanotechnology, 2007. 18(6).

84. K. Zhu, N.R. Neale, A. Miedaner and A.J. Frank, *Enhanced charge-collection efficiencies and light scattering in dye-sensitized solar cells using oriented TiO_2 nanotubes arrays.* Nano Letters, 2007. 7(1): p. 69.

85. G. Redmond, D. Fitzmaurice and M. Graetzel, *Visible-Light Sensitization by Cis-Bis(Thiocyanato)Bis(2,2'-Bipyridyl-4,4'-Dicarboxylato)Ruthenium(II) of a Transparent Nanocrystalline ZnO Film Prepared by Sol-Gel Techniques.* Chemistry of Materials, 1994. 6(5): p. 686.

86. H. Rensmo, K. Keis, H. Lindstrom, S. Sodergren, A. Solbrand, A. Hagfeldt, S.E. Lindquist, L.N. Wang and M. Muhammed, *High light-to-energy conversion efficiencies for solar cells based on nanostructured ZnO electrodes.* Journal of Physical Chemistry B, 1997. 101(14): p. 2598.

87. K. Sayama, H. Sugihara and H. Arakawa, *Photoelectrochemical properties of a porous Nb_2O_5 electrode sensitized by a ruthenium dye.* Chemistry of Materials, 1998. 10(12): p. 3825.

88. S. Ferrere, A. Zaban and B.A. Gregg, *Dye sensitization of nanocrystalline tin oxide by perylene derivatives.* Journal of Physical Chemistry B, 1997. 101(23): p. 4490.

89. M. Quintana, T. Edvinsson, A. Hagfeldt and G. Boschloo, *Comparison of dye-sensitized ZnO and TiO_2 solar cells: Studies of charge transport and carrier lifetime.* Journal of Physical Chemistry C, 2007. 111(2): p. 1035.

90. P. Hoyer, R. Eichberger and H. Weller, *Spectroelectrochemical Investigations of Nanocrystalline ZnO Films.* Berichte Der Bunsen-Gesellschaft-Physical Chemistry Chemical Physics, 1993. 97(4): p. 630.

91. P. OBrien, T. Saeed and J. Knowles, *Speciation and the nature of ZnO thin films from chemical bath deposition.* Journal of Materials Chemistry, 1996. 6(7): p. 1135.

92. L. Vayssieres, K. Keis, A. Hagfeldt and S.E. Lindquist, *Three-dimensional array of highly oriented crystalline ZnO microtubes.* Chemistry of Materials, 2001. 13(12): p. 4395.

93. R.B. Peterson, C.L. Fields and B.A. Gregg, *Epitaxial chemical deposition of ZnO nanocolumns from NaOH.* Langmuir, 2004. 20(12): p. 5114.

94. T. Yoshida, M. Tochimoto, D. Schlettwein, D. Wohrle, T. Sugiura and H. Minoura, *Self-assembly of zinc oxide thin films modified with tetrasulfonated metallophthalocyanines by one-step electrodeposition.* Chemistry of Materials, 1999. 11(10): p. 2657.

95. T. Yoshida and H. Minoura, *Electrochemical self-assembly of dye-modified zinc oxide thin films.* Advanced Materials, 2000. 12(16): p. 1219.

96. M.H. Huang, Y.Y. Wu, H. Feick, N. Tran, E. Weber and P.D. Yang, *Catalytic growth of zinc oxide nanowires by vapor transport.* Advanced Materials, 2001. 13(2): p. 113.

97. C. Bauer, G. Boschloo, E. Mukhtar and A. Hagfeldt, *Electron injection and recombination in Ru(dcbpy)$_2$(NCS)$_2$ sensitized nanostructured ZnO.* Journal of Physical Chemistry B, 2001. 105(24): p. 5585.

98. K. Keis, J. Lindgren, S.E. Lindquist and A. Hagfeldt, *Studies of the adsorption process of Ru complexes in nanoporous ZnO electrodes.* Langmuir, 2000. 16(10): p. 4688.

99. J. Bisquert and V.S. Vikhrenko, *Interpretation of the time constants measured by kinetic techniques in nanostructured semiconductor electrodes and dye-sensitized solar cells.* Journal of Physical Chemistry B, 2004. 108(7): p. 2313.

100. S. Sodergren, A. Hagfeldt, J. Olsson and S.E. Lindquist, *Theoretical-Models for the Action Spectrum and the Current-Voltage Characteristics of Microporous Semiconductor-Films in Photoelectrochemical Cells.* Journal of Physical Chemistry, 1994. 98(21): p. 5552.

101. S.M. Sze, *Physics of Semiconductor Devices, Physics and Technology*. 1st ed. 2006, Chichester: John Wiley & Sons.

102. M. Yanagida, K. Sayama, K. Kasuga, M. Kurashige and H. Sugihara, *Reverse electron transfer at the interface of semiconductor film in dye-sensitized solar cells.* Journal of Photochemistry and Photobiology a-Chemistry, 2006. 182(3): p. 288.

103. M. Gratzel and A.J. Frank, *Interfacial Electron-Transfer Reactions in Colloidal Semiconductor Dispersions, Kinetic Analysis.* Journal of Physical Chemistry, 1982. 86: p. 2964.

104. R.G. Breckenridge and W.R. Hosler, *Electrical Properties of Titanium Dioxide Semiconductors.* Physical Review, 1953. 91(4): p. 793.

105. S.E. Lindquist, B. Finnstrom and L. Tegner, *Photo-Electrochemical Properties of Polycrystalline TiO$_2$ Thin-Film Electrodes on Quartz Substrates.* Journal of the Electrochemical Society, 1983. 130(2): p. 351.

106. A. Hagfeldt, U. Bjorksten and S.E. Lindquist, *Photoelectrochemical Studies of Colloidal TiO$_2$-Films - the Charge Separation Process Studied by Means of Action Spectra in the UV Region.* Solar Energy Materials and Solar Cells, 1992. 27(4): p. 293.

107. L.M. Peter, *Dye-sensitized nanocrystalline solar cells.* Physical Chemistry Chemical Physics, 2007. 9(21): p. 2630.

108. B.C. O'Regan and F. Lenzmann, *Charge transport and recombination in a nanoscale interpenetrating network of n-type and p-type semiconductors: Transient photocurrent and photovoltage studies of TiO2/Dye/CuSCN photovoltaic cells.* Journal of Physical Chemistry B, 2004. 108(14): p. 4342.

109. G. Boschloo and A. Hagfeldt, *Activation energy of electron transport in dye-sensitized TiO$_2$ solar cells.* Journal of Physical Chemistry B, 2005. 109(24): p. 12093.

110. K. Schwarzburg and F. Willig, *Influence of Trap Filling on Photocurrent Transients in Polycrystalline TiO_2.* Applied Physics Letters, 1991. 58(22): p. 2520.

111. B. O'Regan, M. Gratzel and D. Fitzmaurice, *Optical Electrochemistry .1. Steady-State Spectroscopy of Conduction-Band Electrons in a Metal-Oxide Semiconductor Electrode.* Chemical Physics Letters, 1991. 183(1-2): p. 89.

112. U. Kolle, J. Moser and M. Gratzel, *Dynamics of Interfacial Charge-Transfer Reactions in Semiconductor Dispersions - Reduction of Cobaltoceniumdicarboxylate in Colloidal TiO_2.* Inorganic Chemistry, 1985. 24(14): p. 2253.

113. J. Moser, S. Punchihewa, P.P. Infelta and M. Gratzel, *Surface Complexation of Colloidal Semiconductors Strongly Enhances Interfacial Electron-Transfer Rates.* Langmuir, 1991. 7(12): p. 3012.

114. L.M. Peter and K.G.U. Wijayantha, *Intensity dependence of the electron diffusion length in dye-sensitised nanocrystalline TiO_2 photovoltaic cells.* Electrochemistry Communications, 1999. 1(12): p. 576.

115. A. Solbrand, A. Henningsson, S. Sodergren, H. Lindstrom, A. Hagfeldt and S.E. Lindquist, *Charge transport properties in dye-sensitized nanostructured TiO_2 thin film electrodes studied by photoinduced current transients.* Journal of Physical Chemistry B, 1999. 103(7): p. 1078.

116. A. Solbrand, H. Lindstrom, H. Rensmo, A. Hagfeldt, S.E. Lindquist and S. Sodergren, *Electron transport in the nanostructured TiO_2-electrolyte system studied with time-resolved photocurrents.* Journal of Physical Chemistry B, 1997. 101(14): p. 2514.

117. L. Dloczik, O. Ileperuma, I. Lauermann, L.M. Peter, E.A. Ponomarev, G. Redmond, N.J. Shaw and I. Uhlendorf, *Dynamic response of dye-sensitized nanocrystalline solar cells: Characterization by intensity-modulated photocurrent spectroscopy.* Journal of Physical Chemistry B, 1997. 101(49): p. 10281.

118. P.E. de Jongh and D. Vanmaekelbergh, *Investigation of the electronic transport properties of nanocrystalline particulate TiO_2 electrodes by intensity-modulated photocurrent spectroscopy.* Journal of Physical Chemistry B, 1997. 101(14): p. 2716.

119. P.E. de Jongh and D. Vanmaekelbergh, *Trap-limited electronic transport in assemblies of nanometer-size TiO_2 particles.* Physical Review Letters, 1996. 77(16): p. 3427.

120. F. Cao, G. Oskam, G.J. Meyer and P.C. Searson, *Electron transport in porous nanocrystalline TiO_2 photoelectrochemical cells.* Journal of Physical Chemistry, 1996. 100(42): p. 17021.

121. A. Zaban, M. Greenshtein and J. Bisquert, *Determination of the electron lifetime in nanocrystalline dye solar cells by open-circuit voltage decay measurements.* Chemphyschem, 2003. 4(8): p. 859.

122. S. Yanagida, *Recent research progress of dye-sensitized solar cells in Japan.* Comptes Rendus Chimie, 2006. 9(5-6): p. 597.

123. K.S. Ahn, M.S. Kang, J.K. Lee, B.C. Shin and J.W. Lee, *Enhanced electron diffusion length of mesoporous TiO_2 film by using Nb_2O_5 energy barrier for dye-sensitized solar cells.* Applied Physics Letters, 2006. 89(1): p. 3.

124. N.W. Duffy, L.M. Peter and K.G.U. Wijayantha, *Characterisation of electron transport and back reaction in dye-sensitised nanocrystalline solar cells by small amplitude laser pulse excitation.* Electrochemistry Communications, 2000. 2(4): p. 262.

125. U. Würfel, J. Wagner and A. Hinsch, *Spatial electron distribution and its origin in the nanoporous TiO_2 network of a dye solar cell.* Journal of Physical Chemistry B, 2005. 109(43): p. 20444.

126. N.W. Duffy, L.M. Peter, R.M.G. Rajapakse and K.G.U. Wijayantha, *A novel charge extraction method for the study of electron transport and interfacial transfer in dye sensitised nanocrystalline solar cells.* Electrochemistry Communications, 2000. 2(9): p. 658.

127. G. Schlichthorl, N.G. Park and A.J. Frank, *Evaluation of the charge-collection efficiency of dye-sensitized nanocrystalline TiO_2 solar cells.* Journal of Physical Chemistry B, 1999. 103(5): p. 782.

128. G. Franco, J. Gehring, L.M. Peter, E.A. Ponomarev and I. Uhlendorf, *Frequency-resolved optical detection of photoinjected electrons in dye-sensitized nanocrystalline photovoltaic cells.* Journal of Physical Chemistry B, 1999. 103(4): p. 692.

129. L. Kavan and M. Grätzel, *Highly Efficient Semiconducting TiO_2 Photoelectrodes Prepared by Aerosol Pyrolysis.* Electrochimica Acta, 1995. 40(5): p. 643.

130. U. Würfel, M. Peters, A. Hinsch and R. Kern, *Incorporating a secondary electrode in the dye solar cell: Measuring the internal voltage.* Proceedings of the 20th European Photovoltaic Solar Energy Conference, 2005.

131. U. Würfel, J. Wagner and A. Hinsch, *The spatial electron distribution and its dynamics in the nanoporous TiO2 network of a Dye Solar Cell.* Quantsol Proceedings, 2005.

132. K. Lobato and L.M. Peter, *Direct Measurement of the Temperature Coefficient of the Electron Quasi-Fermi Level in Dye-Sensitized Nanocrystalline Solar Cells Using a Titanium Sensor Electrode.* Journal of Physical Chemistry B, 2006.

133. E. Hristova, L. Arsov, B.N. Popov and R.E. White, *Ellipsometric and Raman spectroscopic study of thermally formed films on titanium.* Journal of the Electrochemical Society, 1997. 144(7): p. 2318.

134. L. Forro, O. Chauvet, D. Emin, L. Zuppiroli, H. Berger and F. Levy, *High mobility n-type charge carriers in large single crystals of anatase TiO_2.* Journal of Applied Physics, 1994. 75(1): p. 633.

135. M.J. Cass, A.B. Walker, D. Martinez and L.M. Peter, *Grain morphology and trapping effects on electron transport in dye-sensitized nanocrystalline solar cells.* Journal of Physical Chemistry B, 2005. 109(11): p. 5100.

136. M.J. Cass, F.L. Qiu, A.B. Walker, A.C. Fisher and L.M. Peter, *Influence of grain morphology on electron transport in dye sensitized nanocrystalline solar cells.* Journal of Physical Chemistry B, 2003. 107(1): p. 113.

137. L.M. Peter, A.B. Walker, G. Boschloo and A. Hagfeldt, *Interpretation of apparent activation energies for electron transport in dye-sensitized nanocrystalline solar cells.* Journal of Physical Chemistry B, 2006. 110(28): p. 13694.

138. B.C. O'Regan and J.R. Durrant, *Calculation of Activation Energies for Transport and Recombination in Mesoporous TiO_2/Dye/Electrolyte Films-Taking into Account Surface Charge Shifts with Temperature.* Journal of Physical Chemistry B, 2006. 110(17): p. 8544.

139. W.H. Press, S.A. Teukolsky, W.T. Vettering and B.P. Flannery, *Numerical Recipes in Fortran, 2nd ed.* Cambridge University Press, U.K., 1992.

140. A.B. Walker, L.M. Peter, D. Martinez and K. Lobato, *Transient Photocurrents in Dye-Sensitized Nanocrystalline Solar Cells.* Chimia, In press.

11 Appendix A: Full Derivation of the Solution to the Continuity Equation Under Photostationary Conditions

The continuity equation to solve is;

$$\frac{\partial n_C(x)}{\partial t} = I_0 \alpha e^{-\alpha x} + D_0 \frac{\partial^2 n_C(x)}{\partial x^2} - k_0 \left[n_C(x) - n_{eq} \right] = 0 \tag{105}$$

Rearrange to;

$$D_0 \frac{\partial^2 n_C(x)}{\partial x^2} - k_0 \left[n_C(x) - n_{eq} \right] = -I_0 \alpha e^{-\alpha x} \tag{106}$$

Start by solving the reduced equation;

$$D_0 \frac{\partial^2 n_C(x)}{\partial x^2} - k_0 \left[n_C(x) - n_{eq} \right] = 0 \tag{107}$$

A substitution of variables is done;

$$N(x) = n(x) - n_{eq} \tag{108}$$

Therefore the derivatives with the substitution of variables are:

$$\begin{aligned} \frac{dN}{dx} &= \frac{dn}{dx} \\ \frac{d^2N}{dx^2} &= \frac{d^2n}{dx^2} \end{aligned} \tag{109}$$

The reduced equation then becomes;

$$D_0 \frac{\partial^2 N}{\partial x^2} - k_n N = 0 \tag{110}$$

A known solution to this type of differential equation is;

$$N = e^{mx} \tag{111}$$

I.e. we can show that it is a solution to the reduced equation, by first taking its second derivative;

$$\frac{d^2N}{dx^2} = m^2 e^{mx} = m^2 N \tag{112}$$

To then substitute into the reduced equation;

$$\begin{aligned} D_0 m^2 N - k_n N &= 0 \\ D_0 m^2 - k_n &= 0 \end{aligned} \tag{113}$$

We can now solve for m;

$$m = \pm\sqrt{\frac{k_0}{D_0}} \tag{114}$$

The solution for m being a quadratic form has two solutions;

$$\begin{aligned} N_1 &= \exp\left(+\sqrt{\frac{k_0}{D_0}}x\right) \\ N_2 &= \exp\left(-\sqrt{\frac{k_0}{D_0}}x\right) \end{aligned} \tag{115}$$

These solutions satisfy the reduced equation separately, but the sum of them will also satisfy the reduced equation but applying pre-exponential factors;

$$N = A\exp\left(\sqrt{k_0/D_0}x\right) + B\exp\left(-\sqrt{k_0/D_0}x\right) \tag{116}$$

We can again show that this will also satisfy the reduced equation;

$$\begin{aligned} &D_n\frac{d^2}{dx^2}\left\{A\exp\left(\sqrt{k_0/D_0}x\right) + B\exp\left(-\sqrt{k_0/D_0}x\right)\right\} - k_n\left\{A\exp\left(\sqrt{k_0/D_0}x\right) + B\exp\left(-\sqrt{k_0/D_0}x\right)\right\} = 0 \\ &D_0\left\{\frac{k_0}{D_0}A\exp\left(\sqrt{k_0/D_0}x\right) + \frac{k_0}{D_0}B\exp\left(-\sqrt{k_0/D_0}x\right)\right\} - k_n\left\{A\exp\left(\sqrt{k_0/D_0}x\right) + B\exp\left(-\sqrt{k_0/D_0}x\right)\right\} = 0 \\ &k_0\left\{A\exp\left(\sqrt{k_0/D_0}x\right) + B\exp\left(-\sqrt{k_0/D_0}x\right)\right\} - k_n\left\{A\exp\left(\sqrt{k_0/D_0}x\right) + B\exp\left(-\sqrt{k_0/D_0}x\right)\right\} = 0 \\ &0 = 0 \end{aligned} \tag{117}$$

I.e. it also works.

The complimentary function to the reduced equation (integral) is;

$$N(x) = A\exp\left(\sqrt{\frac{k_0}{D_0}}x\right) + B\exp\left(-\sqrt{\frac{k_0}{D_0}}x\right) \tag{118}$$

Replacing the substituted variable;

$$n(x) = A\exp\left(\sqrt{\frac{k_0}{D_0}}x\right) + B\exp\left(-\sqrt{\frac{k_0}{D_0}}x\right) + n_{eq} \tag{119}$$

We now return to the initial differential equation to solve;

$$\frac{\partial n_C(x)}{\partial t} = I_0\alpha e^{-\alpha x} + D_0\frac{\partial^2 n_C(x)}{\partial x^2} - k_0\left[n_C(x) - n_{eq}\right] = 0 \tag{120}$$

And try another trial solution;

$$\begin{aligned} n(x) &= Ce^{-\alpha x} \\ N(x) &= n(x) - n_{eq} \\ N(x) &= Ce^{-\alpha x} - n_{eq} \end{aligned} \qquad 121$$

Differentiating this trial solution;

$$\begin{aligned} \frac{dN}{dx} &= C\alpha \frac{dn}{dx} \\ \frac{d^2N}{dx^2} &= C\alpha^2 \frac{d^2n}{dx^2} \end{aligned} \qquad 122$$

Then substituting into the original differential equation to solve;

$$\begin{aligned} D_0 \frac{\partial^2 N}{\partial x^2} - k_n N &= -\alpha I_0 e^{-\alpha x} \\ D_0 C\alpha^2 e^{-\alpha x} - k_n C e^{-\alpha x} &= -\alpha I_0 e^{-\alpha x} \end{aligned} \qquad 123$$

Rearranging accordingly to solve for the pre-exponential factor C;

$$\begin{aligned} D_0 \frac{\partial^2 N}{\partial x^2} - k_n N &= -\alpha I_0 e^{-\alpha x} \\ D_0 C\alpha^2 - k_n C &= -\alpha I_0 \\ C &= -\frac{\alpha I_0}{D_0\alpha^2 - k_0} \end{aligned} \qquad 124$$

A value of C is set to allow this form of N to be a solution. Thus a general solution is;

$$N = A\exp\left(\sqrt{k_0/D_0}\,x\right) + B\exp\left(-\sqrt{k_0/D_0}\,x\right) + C\exp(-\alpha x) \qquad 125$$

A and B are the pre-exponential factors from the reduced equation (and thus form the complimentary function) while the pre-exponential factor C forms the particular integral solution.

Next we can test to see if this form of N is solution to the continuity equation;

$$\begin{aligned} & D_0 \frac{\partial^2 N}{\partial x^2} - k_0 N = -I_0 \alpha e^{-\alpha x} \\ & D_0 \frac{\partial^2}{\partial x^2}\left\{ A\exp\left(\sqrt{k_0/D_0}\right) + B\exp\left(-\sqrt{k_0/D_0}\right) - \frac{\alpha I_0}{D_0\alpha^2 - k_0}\exp(-\alpha x)\right\} \\ & - k_0\left\{ A\exp\left(\sqrt{k_0/D_0}\right) + B\exp\left(-\sqrt{k_0/D_0}\right) - \frac{\alpha I_0}{D_0\alpha^2 - k_0}\exp(-\alpha x)\right\} \\ & = -I_0\alpha\exp(-\alpha x) \end{aligned} \qquad 126$$

Differentiating;

$$
\begin{aligned}
&D_0\left\{A\frac{k_0}{D_0}\exp\left(\sqrt{k_0/D_0}\right)+B\frac{k_0}{D_0}\exp\left(-\sqrt{k_0/D_0}\right)-\alpha^2\frac{\alpha I_0}{D_0\alpha^2-k_0}\exp(-\alpha x)\right\}\\
&-k_0\left\{A\exp\left(\sqrt{k_0/D_0}\right)+B\exp\left(-\sqrt{k_0/D_0}\right)-\frac{\alpha I_0}{D_0\alpha^2-k_0}e\right\}\\
&=-I_0\alpha\exp(-\alpha x)
\end{aligned}
\qquad 127
$$

Rearranging;

$$
\begin{aligned}
&k_0\left\{A\exp\left(\sqrt{k_0/D_0}x\right)+B\exp\left(-\sqrt{k_0/D_0}x\right)\right\}-D_0\alpha^2\frac{\alpha I_0}{D_0\alpha^2-k_0}\exp(-\alpha x)\\
&-k_0\left\{A\exp\left(\sqrt{k_0/D_0}x\right)+B\exp\left(-\sqrt{k_0/D_0}x\right)\right\}+k_0\frac{\alpha I_0}{D_0\alpha^2-k_0}\exp(-\alpha x)\\
&=-I_0\alpha\exp(-\alpha x)
\end{aligned}
\qquad 128
$$

and eliminating:

$$
-D_0\alpha^2\frac{\alpha I_0}{D_0\alpha^2-k_0}\exp(-\alpha x)+k_0\frac{\alpha I_0}{D_0\alpha^2-k_0}\exp(-\alpha x)=-I_0\alpha\exp(-\alpha x) \qquad 129
$$

Then rearranging to two show that the RHS is equivalent to the LHS;

$$
\begin{aligned}
&\left(\frac{k_0}{D_0\alpha^2-k_0}-\frac{D_0\alpha^2}{D_0\alpha^2-k_0}\right)I_0\exp(-\alpha x)\equiv-I_0\alpha\exp(-\alpha x)\\
&\left(\frac{k_0-D_0\alpha^2}{D_0\alpha^2-k_0}\right)I_0\exp(-\alpha x)\equiv-I_0\alpha\exp(-\alpha x)\\
&\left(\frac{-D_0\alpha^2+k_0}{D_0\alpha^2-k_0}\right)I_0\exp(-\alpha x)\equiv-I_0\alpha\exp(-\alpha x)\\
&(-1)I_0\exp(-\alpha x)\equiv-I_0\alpha\exp(-\alpha x)
\end{aligned}
\qquad 130
$$

I.e. the form on N is a general solution to the continuity equation, and for completeness we can substitute the variables to have n(x) with the pre-exponential factor C already solved for;

$$
n(x)=A\exp\left(\sqrt{k_0/D_0}x\right)+B\exp\left(-\sqrt{k_0/D_0}x\right)-\frac{\alpha I_0}{D_0\alpha^2-k_0}\exp(-\alpha x)+n_{eq} \qquad 131
$$

To solve for the pre-exponential factors A and B, the boundary conditions need to be applied.

The extraction rate at x=0 must equal the rate at which electrons arrive at x=0, i.e.;

$$
k_{ext}n_{x=0}=-D_0\left.\frac{dn}{dx}\right|_{x=0} \qquad 132
$$

The second boundary condition is that at x=d, there can be no net electron flux, thus;

$$\left.\frac{dn}{dx}\right|_{x=d} = 0 \qquad 133$$

Applying the first boundary condition;

$$\begin{aligned}
&\frac{dn}{dx} = \sqrt{\frac{k_0}{D_0}}\left\{A\exp\left(\sqrt{k_0/D_0}\,x\right) + B\exp\left(-\sqrt{k_0/D_0}\,x\right)\right\} + \frac{\alpha^2 I_0}{D_0\alpha^2 - k_0}\exp(-\alpha x) \\
&-D_0\left.\frac{dn}{dx}\right|_{x=0} = -D_0\left(\sqrt{\frac{k_0}{D_0}}\{A-B\} + \frac{\alpha^2 I_0}{D_0\alpha^2 - k_0}\right) = k_{ext}n_{x=0}
\end{aligned} \qquad 134$$

It so happens that we can define $n_{x=0}$;

$$n(x=0) = A + B - \frac{\alpha I_0}{D_0\alpha^2 - k_0} + n_{eq} \qquad 135$$

Thus substituting back into to the expression arising from the first boundary condition;

$$\begin{aligned}
&-D_0\left(\sqrt{\frac{k_0}{D_0}}\{A-B\} + \frac{\alpha^2 I_0}{D_0\alpha^2 - k_0}\right) = k_{ext}\left(A + B - \frac{\alpha I_0}{D_0\alpha^2 - k_0} + n_{eq}\right) \\
&-\sqrt{k_0 D_0}\,A + \sqrt{k_0 D_0}\,B - D_0\frac{\alpha^2 I_0}{D_0\alpha^2 - k_0} = k_{ext}A + k_{ext}B - k_{ext}\frac{\alpha I_0}{D_0\alpha^2 - k_0} + k_{ext}n_{eq} \\
&-A\left(\sqrt{k_0 D_0} + k_{ext}\right) + B\left(\sqrt{k_0 D_0} + k_{ext}\right) = k_{ext}\frac{\alpha I_0}{D_0\alpha^2 - k_0} + k_{ext}n_{eq} + D_0\frac{\alpha^2 I_0}{D_0\alpha^2 - k_0}
\end{aligned} \qquad 136$$

This equation will be one of two required to solve for A and B simultaneously.

Applying the second boundary condition obtains the second of the two equations required to solve for A and B;

$$\begin{aligned}
&\frac{dn}{dx} = \sqrt{\frac{k_0}{D_0}}\left\{A\exp\left(\sqrt{k_0/D_0}\,x\right) - B\exp\left(-\sqrt{k_0/D_0}\,x\right)\right\} + \frac{\alpha^2 I_0}{D_0\alpha^2 - k_0}\exp(-\alpha x) \\
&\left.\frac{dn}{dx}\right|_{x=d} = 0 = \sqrt{\frac{k_0}{D_0}}\left\{A\exp\left(\sqrt{k_0/D_0}\,d\right) + B\exp\left(-\sqrt{k_0/D_0}\,d\right)\right\} + \frac{\alpha^2 I_0}{D_0\alpha^2 - k_0}\exp(-\alpha d) \\
&A\sqrt{\frac{k_0}{D_0}}\exp\left(\sqrt{k_0/D_0}\,d\right) - B\sqrt{\frac{k_0}{D_0}}\exp\left(-\sqrt{k_0/D_0}\,d\right) = -\frac{\alpha^2 I_0}{D_0\alpha^2 - k_0}\exp(-\alpha d) \\
&A\sqrt{k_0 D_0}\exp\left(\sqrt{k_0/D_0}\,d\right) - B\sqrt{k_0 D_0}\exp\left(-\sqrt{k_0/D_0}\,d\right) = -D_0\frac{\alpha^2 I_0}{D_0\alpha^2 - k_0}\exp(-\alpha d)
\end{aligned} \qquad 137$$

Thus the two simultaneous equations to solve for A and B are;

$$-A\left(\sqrt{k_0 D_0}+k_{ext}\right)+B\left(\sqrt{k_0 D_0}+k_{ext}\right)=k_{ext}\frac{\alpha I_0}{D_0\alpha^2-k_0}+k_{ext}n_{eq}+D_0\frac{\alpha^2 I_0}{D_0\alpha^2-k_0} \quad 138$$

$$A\sqrt{k_0 D_0}\exp\left(\sqrt{k_0/D_0}d\right)-B\sqrt{k_0 D_0}\exp\left(-\sqrt{k_0/D_0}d\right)=-D_0\frac{\alpha^2 I_0}{D_0\alpha^2-k_0}\exp(-\alpha d)$$

For the sake of clarity some repeated terms are substituted, letting;

$$\begin{aligned}\gamma &= \sqrt{k_0 D_0}\\ \phi &= \sqrt{k_0/D_0}\\ \varphi &= \frac{\alpha I_0}{D_0\alpha^2-k_0}\end{aligned} \quad 139$$

Thus the two simultaneous equations become;

$$-A\left(\sqrt{k_0 D_0}+k_{ext}\right)+B\left(\sqrt{k_0 D_0}+k_{ext}\right)=k_{ext}\frac{\alpha I_0}{D_0\alpha^2-k_0}+k_{ext}n_{eq}+D_0\frac{\alpha^2 I_0}{D_0\alpha^2-k_0} \quad 140$$

$$A(-\gamma-k_{ext})+B(\gamma+k_{ext})=\varphi(k_{ext}+\alpha D_0)+k_{ext}n_{eq}$$

and;

$$A\sqrt{k_0 D_0}\exp\left(\sqrt{k_0/D_0}d\right)-B\sqrt{k_0 D_0}\exp\left(\sqrt{k_0/D_0}d\right)=-D_0\frac{\alpha^2 I_0}{D_0\alpha^2-k_0}\exp(-\alpha d) \quad 141$$

$$A\gamma\exp(\phi d)-B\gamma\exp(\phi d)=-\alpha D_0\varphi\exp(-\alpha d)$$

We now have a set of simultaneous equations of the appropriate form to be solved applying matrix methods;

$$\begin{aligned}Au+Bv&=y\\ Aw+Bx&=z\end{aligned} \quad 142$$

Where again for clarity;

$$\begin{aligned}u &= -\gamma-k_{ext}\\ v &= \gamma+k_{ext}\\ y &= \varphi(k_{ext}+\alpha D_0)+k_{ext}n_{eq}\end{aligned} \quad 143$$

and;

$$\begin{aligned}w &= \gamma\exp(\phi d)\\ x &= -\gamma\exp(\phi d)\\ z &= -\alpha D_0\varphi\exp(-\alpha d)\end{aligned} \quad 144$$

The couple of simultaneous equations can be expressed as a matrix product;

$$\begin{bmatrix} u & v \\ w & x \end{bmatrix}\begin{bmatrix} A \\ B \end{bmatrix}=\begin{bmatrix} y \\ z \end{bmatrix} \tag{145}$$

Thus one can solve for A and B by;

$$\begin{bmatrix} A \\ B \end{bmatrix}=\begin{bmatrix} u & v \\ w & x \end{bmatrix}^{-1}\begin{bmatrix} y \\ z \end{bmatrix} \tag{146}$$

Where the inverse of a 2x2 matrix is;

$$\begin{bmatrix} u & v \\ w & x \end{bmatrix}^{-1}=\frac{1}{ux-vw}\begin{bmatrix} x & -v \\ -w & u \end{bmatrix} \tag{147}$$

Thus rearranging the matrices to solve for the unknowns A and B and expanding the resulting matrix multiplication;

$$\begin{bmatrix} A \\ B \end{bmatrix}=\frac{1}{ux-vw}\begin{bmatrix} x & -v \\ -w & u \end{bmatrix}\begin{bmatrix} y \\ z \end{bmatrix}$$

$$A=\frac{xy-vz}{ux-vw} \tag{148}$$

$$B=\frac{-wy+vz}{ux-vw}$$

We can now replace all the substitutions to obtain the full solutions to the factors A and B;

$$\begin{aligned} A &= \frac{\left(-\sqrt{k_0 D_0}\exp\left(\sqrt{k_0/D_0}\,d\right)\right)\left(\frac{\alpha I_0}{D_0\alpha^2-k_0}\left(k_{ext}+\alpha D_0\right)+k_{ext}n_{eq}\right)-\left(\sqrt{k_0 D_0}+k_{ext}\right)\left(-D_0\alpha\frac{\alpha I_0}{D_0\alpha^2-k_0}\exp(-\alpha d)\right)}{\left(-\sqrt{k_0 D_0}-k_{ext}\right)\left(-\sqrt{k_0 D_0}\exp\left(\sqrt{k_0/D_0}\,d\right)\right)-\left(\sqrt{k_0 D_0}+k_{ext}\right)\left(\sqrt{k_0 D_0}\exp\left(\sqrt{k_0/D_0}\,d\right)\right)} \\ &= \frac{-\left(\sqrt{k_0 D_0}\exp\left(\sqrt{k_0/D_0}\,d\right)\right)\left(\frac{\alpha I_0}{D_0\alpha^2-k_0}\left(k_{ext}+\alpha D_0\right)+k_{ext}n_{eq}\right)+\left(\sqrt{k_0 D_0}+k_{ext}\right)\left(D_0\alpha\frac{\alpha I_0}{D_0\alpha^2-k_0}\exp(-\alpha d)\right)}{\left(-\sqrt{k_0 D_0}-k_{ext}\right)\left(-\sqrt{k_0 D_0}\exp\left(\sqrt{k_0/D_0}\,d\right)\right)-\left(\sqrt{k_0 D_0}+k_{ext}\right)\left(\sqrt{k_0 D_0}\exp\left(\sqrt{k_0/D_0}\,d\right)\right)} \end{aligned} \tag{149}$$

$$\begin{aligned} B &= \frac{-\left(\sqrt{k_0 D_0}\exp\left(\sqrt{k_0/D_0}\,d\right)\right)\left(\frac{\alpha I_0}{D_0\alpha^2-k_0}\left(k_{ext}+\alpha D_0\right)+k_{ext}n_{eq}\right)+\left(\sqrt{k_0 D_0}+k_{ext}\right)\left(-D_0\alpha\frac{\alpha I_0}{D_0\alpha^2-k_0}\exp(-\alpha d)\right)}{\left(-\sqrt{k_0 D_0}-k_{ext}\right)\left(-\sqrt{k_0 D_0}\exp\left(\sqrt{k_0/D_0}\,d\right)\right)-\left(\sqrt{k_0 D_0}+k_{ext}\right)\left(\sqrt{k_0 D_0}\exp\left(\sqrt{k_0/D_0}\,d\right)\right)} \\ &= -\frac{\left(\sqrt{k_0 D_0}\exp\left(\sqrt{k_0/D_0}\,d\right)\right)\left(\frac{\alpha I_0}{D_0\alpha^2-k_0}\left(k_{ext}+\alpha D_0\right)+k_{ext}n_{eq}\right)+\left(\sqrt{k_0 D_0}+k_{ext}\right)\left(D_0\alpha\frac{\alpha I_0}{D_0\alpha^2-k_0}\exp(-\alpha d)\right)}{\left(\sqrt{k_0 D_0}+k_{ext}\right)\left(\sqrt{k_0 D_0}\exp\left(\sqrt{k_0/D_0}\,d\right)\right)-\left(\sqrt{k_0 D_0}+k_{ext}\right)\left(\sqrt{k_0 D_0}\exp\left(\sqrt{k_0/D_0}\,d\right)\right)} \end{aligned}$$

We now have required pre-exponential factors to satisfy the time independent continuity equation, and calculate n(x).

12 Appendix B: Photocurrent Transients

Photocurrent transients were measured over several order of magnitude of time and illumination intensity. Two current amplifiers were used, Femto Variable-Gain Low-Noise Current Amplifier DLPCA-200 (500kHz bandwidth), and Femto Variable-Gain High-Speed Current Amplifier DHPCA-100 (200mHz bandwidth). These two amplifiers used in conjunction allowed for the wide dynamic range of measurements.

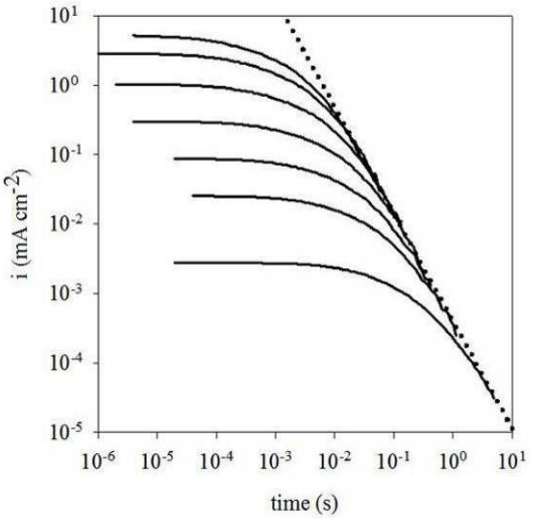

Figure 87 Light off photocurrent transient of a typical DSC employing the Solaronix colloid. The light intensities of the 532nm LED varied between 10^{17} photons $cm^{-2}s^{-1}$ and 10^{13} photons $cm^{-2}s^{-1}$. The dotted line is a guide to demonstrate the tendency to a power law current decay profile. Illumination was through FTO.

Because the current amplifiers has an input impedance of 50Hz, some modifications were made to reduce output impedance sensed by the DSC and hence improve the time resolution, by reducing the RC time-constant. These were achieved by using a shorting resistor in parallel with measuring resistor of the current amplifier. Also the cells used for these measurements employed the optimisation of the contacts by evaporation of gold. The sensed output impedance of the DSC is therefore;

$$R_{OUT} = \left(\frac{1}{R_P} + \frac{1}{R_{AMP}} \right)^{-1} \qquad 150$$

These modifications are important when performing photocurrent transients arising from a pulsed source of illumination.

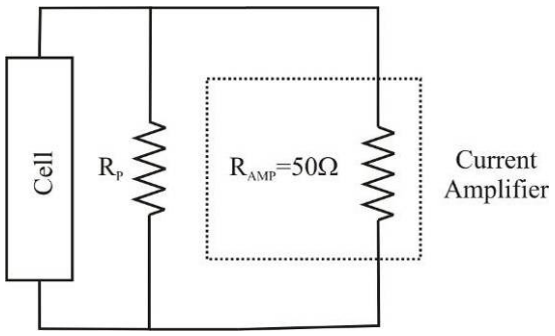

Figure 88 Schematic representation of how the output impedance of the cell was adjusted to minimise the RC time-constant of the system.

The current measured through R_{AMP} is then multiplied by R_{AMP}/R_P to give the total current. Typical values of R_P were 1 to 10Ω.

The pulsed illumination source was a 532nm Nd-Yag Continuum laser with typical FWHM pulse width of 4ns. The current transients resultant from pulsed illumination were obtained by recording at different timescales and then superimposing.

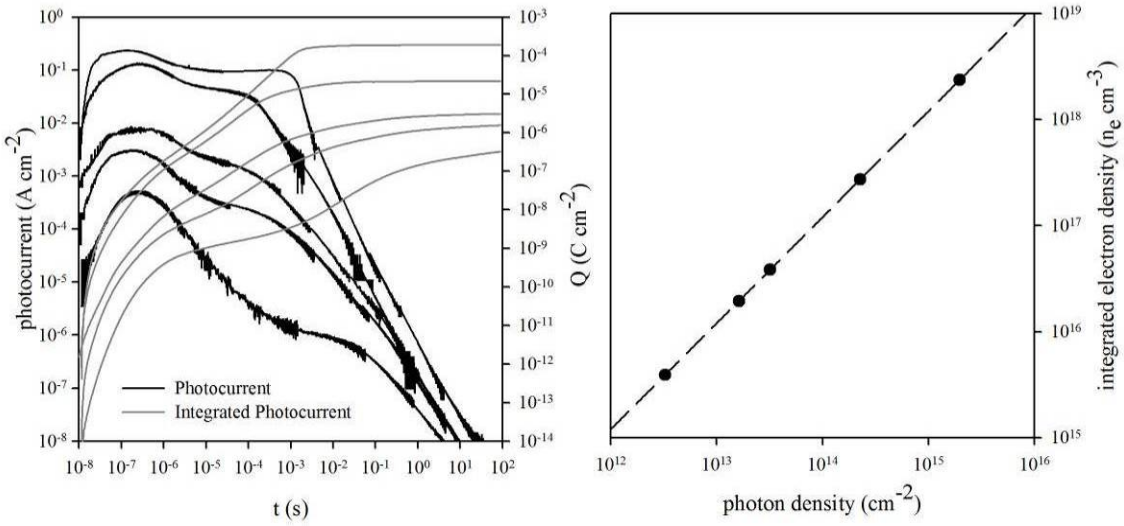

Figure 89 Left: Pulsed photocurrent and corresponding numerically integrated charge transients for a cell employing optimised gold contacts. Photon densities were 2x10^{15}cm^{-2} at 100% with a subsequent decreases to 10, 1, 0.54, and 0.1%. Right: Integral of photocurrent transients demonstrating linear response to photon density.. Illumination was through the FTO.

The pulsed photocurrent transients are fairly complicated but also show the tendency to a power law current decay profile.

13 Appendix C: Effect of tertiary butyl pyridine

Tertiary butyl pyridine is a frequent additive in DSCs, and is found to improve the open-circuit voltage. The reasons for this could be either by passivation of surface recombination sites and/or by shifting the position of the conduction band edge, because of changes to surface dipole moments.

It was found that photocurrent transients of DSCs remained similar even when differing by the addition of TBP in the electrolyte. This is illustrated in Figure 91. A possible reason for this could be the trap distribution as viewed from the conduction band remains un-altered, i.e. the trap distribution shifts with the conduction band. Evidence supporting this idea is illustrated in Figure 91 and Figure 92. The temporal profile of the photocurrent transients *i(t)* remains un-altered. This signifies that the injected (light on) and extracted (light off) charge is also equal $Q = \int i(t)dt$. If the current transients are due to the filling and emptying of traps, then the trap distribution with respect to the conduction band edge has to remain equal.

The charge extraction data shown in Figure 92 illustrates the clear shift in the trap distribution by the addition of TBP, with the trap distribution shifting upwards in energy. This is schematically illustrated in Figure 90. The effect on the iV is also illustrated with the larger open-circuit voltages.

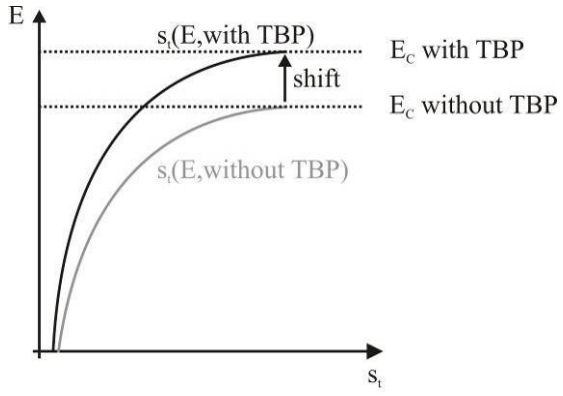

Figure 90 Schematic representation of how the conduction band and trap density of states could shift with the addition of TBP.

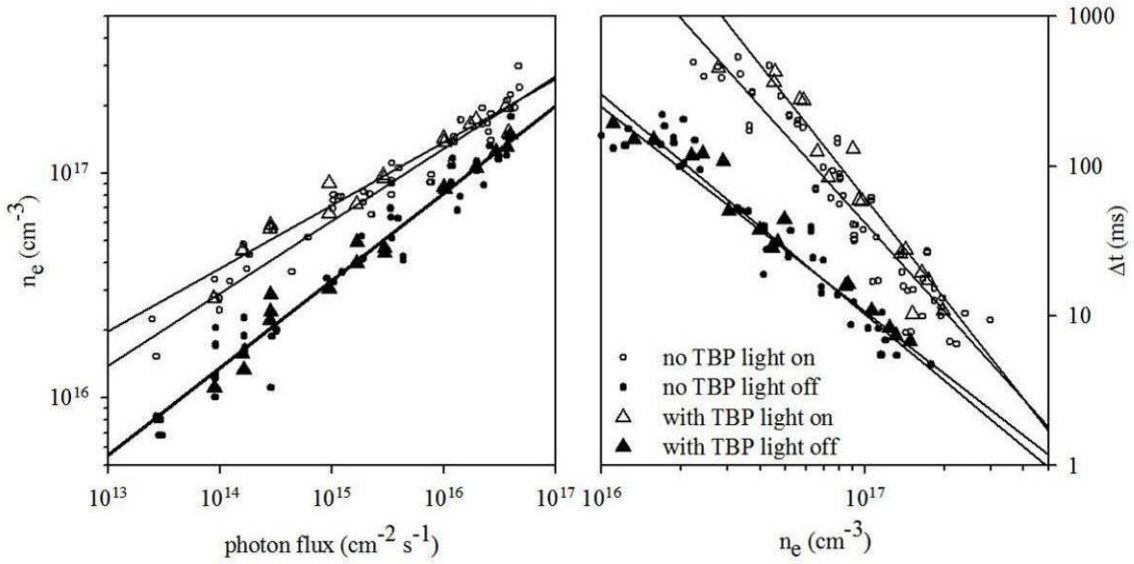

Figure 91 Left: Short-circuit extracted and injected charge for light on and off photocurrent transients. Right: Time taken (Δt) for the current density to vary between 10% and 90% of the photostationary state.

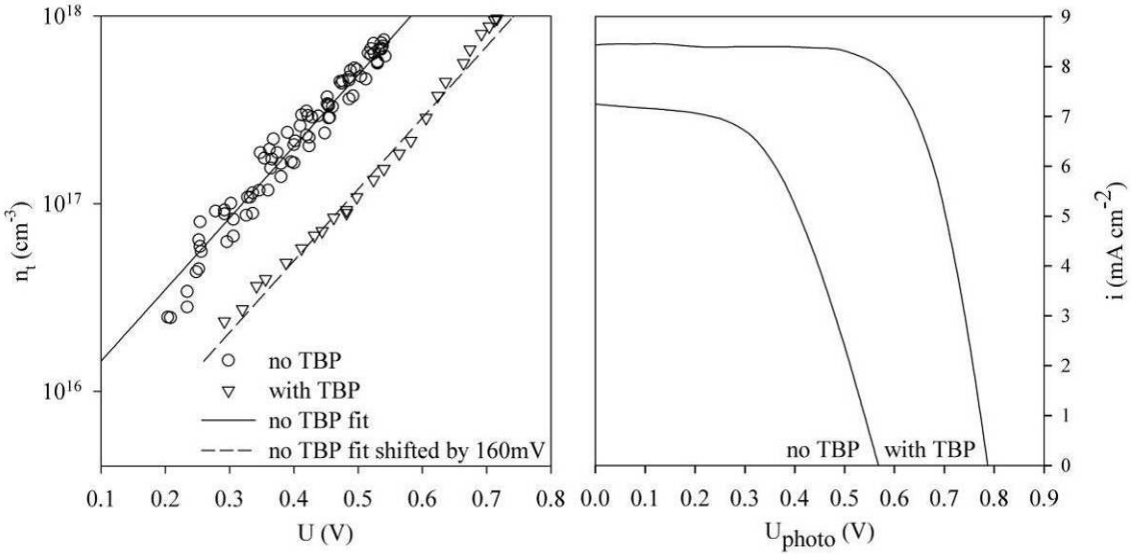

Figure 92 Left: Charge extraction data for cells with and without TBP. Right: AM1.5 iV curves of the cells with and without TBP.